HEAVY FERMIONS: FROM NODAL METALS TO SUPER-SPINS

By

ALINE RAMIRES NEVES DE OLIVEIRA

A dissertation submitted to the

Graduate School—New Brunswick

Rutgers, The State University of New Jersey

in partial fulfillment of the requirements

for the degree of

Doctor of Philosophy

Graduate Program in Physics and Astronomy

written under the direction of

Piers Coleman

and approved by

_____

_____

_____

_____

_____

New Brunswick, New Jersey

October, 2015

ABSTRACT OF THE DISSERTATION

Heavy Fermions: From Nodal Metals to Super-Spins

By ALINE RAMIRES NEVES DE OLIVEIRA

Dissertation Director:

Piers Coleman

Condensed matter physics is an area of research which lies at a sweet spot between two complementary perspectives: the atomistic point of view which takes into account all the details of the system of interest; and the framework of universality and emergent phenomena, which allows us to make drastic simplifications to the microscopic description of materials while still being able to explain much of the experimentally observed phenomena. This thesis addresses problems from both perspectives, focusing on heavy fermion systems.

Heavy fermion systems are prototype materials for the study of strongly correlations and quantum criticality. Theoretical understanding of these systems is important for the design of new materials and for the fundamental understanding of quantum critical phenomena. This thesis is strongly motivated by recent experiments in an *intrinsically quantum critical* material, β-$YbAlB_4$. This system shows anomalous critical exponents in transport and thermodynamics. In Chapter 2 we construct a phenomenological theory for the heavy fermion metal β-$YbAlB_4$ based on the Anderson model, taking into account the peculiarities of this specific material. We analyze the consequences of a non-trivial, momentum-dependent, hybridization matrix between f-electrons and conduction electrons, which gives rise to a nodal metal with unusual dispersion and singular thermodynamic properties, in accordance

with experiments. In Chapter 3 we analyze the Electron Spin Resonance experiments in this same material and propose a theory including spin-orbit coupling, crystal electric fields and hyperfine coupling which can account for many of the features of the experimentally observed signal.

Within a broader perspective on heavy fermion systems, the absence of a single unified theoretical description which can account for the plethora of phenomena observed in this class of materials also motivates us to consider new theoretical approaches. In Chapter 4 we generalize the construction of supersymmetric spin representations in the large-N limit, now with *symplectic symmetry*, and explore its properties. We apply the supersymmetric symplectic-N spin representation to two toy models in Chapter 5, and find promising results for a future unified picture of heavy fermion systems.

Acknowledgments

I would like to start acknowledging my advisor, Piers Coleman, for guiding me and constantly feeding me with interesting questions and ideas since the very beginning of my stay at Rutgers. His enthusiasm made this doctoral endeavor an enjoyable experience. His support and encouragement towards my participation in many meetings and schools was key for my formation as a scientist, allowing me to look at the forefront of research and to connect with other students and scientists in the area, what will be of extreme importance for the next steps in my career;

I would like to thank the Department of Physics and Astronomy at Rutgers for the support; for all the staff who helped me with the necessary paperwork (a special thanks to Shirley Hinds who needed to struggle with my very long last name for a while!); for all the faculty who dedicated some of their time to teaching graduate courses that complemented my formation, specially in condensed matter: Lev Ioffe, Emil Yuzbashyan and Gabriel Kotliar, whose courses gave me a great breadth of understanding;

I would also like to thank other PhD students and post-docs who shared some of their experience with me during journal clubs, group meetings or informal discussions. In particular: Tzen Ong, Onur Erten and Victor Alexandrov for being great group mates; Maryam Taherinejad, Sebastian E. Reyes-Lillo, Chuck-Hou Yee, Tahir Yusufaly, Lucian Pascut, Turan Birol, Deepak Iyer, Anindya Roy, Sinisa Coh, Senia Coh, Simon Knappen and Michael Manhart for interesting discussions about Physics and beyond;

I would like to thank the Rutgers Graduate School-New Brunswick for providing a wealth of opportunities for professional development of graduate students with programs as GradFund, the TA Project, and the PreDoctoral Leadership Development Institute, from which I benefited a lot;

I would also like to thank the funding agencies for the support: the National Science

Foundation (DMR 0907179, DMR 1309929) and the Department of Energy (DE-AC02-98 CH 10886); the American Physical Society for the Brazil-US Visitation Program Grants which allowed me to keep connections with my mother land; and several other institutions which provided support for my participation in events as the High Magnetic Field Laboratory in Tallahassee, the New York Academy of Sciences, the International Centre for Theoretical Physics in Trieste, the International Institute of Physics in Brazil, and the Institute for Complex Adaptive Matter. I would like to thank Ellen Langreth for establishing the David Langreth Graduate Development Award, which was a great motivation early in my PhD and allowed me to participate in conferences which I would not be able to attend otherwise. A special thanks for the Kavli Institute for Theoretical Physics at the University of California Santa Barbara for hosting me during the Fall 2014.

Dedication

A todos que entendem porque alguém empreenderia no desafio de uma pós-graduação...

To all those who understand why one would endeavour the challenges of a doctoral degree...

Table of Contents

List of Tables

List of Figures

Chapter 1

Introduction

In this introductory chapter we motivate the study of condensed matter as a fundamental area of investigation for the search and understanding of new phases of matter. We introduce the main concepts that help us to progress in this field, focusing on strongly correlated systems and narrowing the discussion to heavy fermion systems, the main topic of this thesis. We highlight the main features and recent experiments on heavy fermions and discuss the current theoretical understanding and challenges in this subject area.

1.1 The Concept of Emergence

A crucial concept for the understanding of phenomena in solids today is the idea of *emergence*, which tells us that a reductionist point of view is not always enough: knowledge on the microscopic laws of nature does not directly provide us with the ability to understand the properties of the universe at large [1]. When many particles are placed together, the interactions and correlations between them can give rise to unexpected phenomena, called *emergent phenomena*. Examples of emergent phenomena can be seen in nature with the formation of crystals, sand dunes and even with the emergence of life itself.

In his insightful 1972 paper [1], P. W. Anderson points out that a *constructionist* hypothesis, built solely on the knowledge acquired from a reductionist approach, does not always hold. He writes: "The constructionist hypothesis breaks down when confronted with the twin difficulties of scale and complexity ... at each level of complexity new properties appear, and the understanding of the new behaviors requires research which I think is as fundamental in its nature as any other."

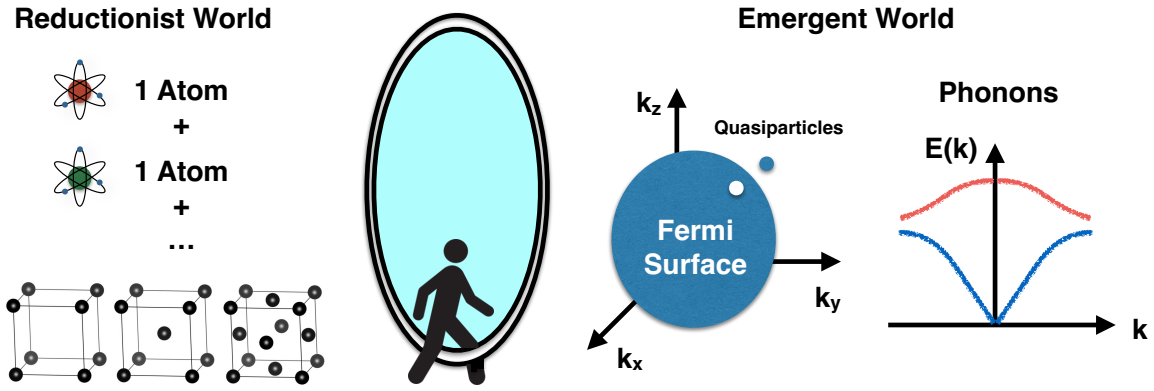

Figure 1.1: Reductionist versus Emergent world: in the *Reductionist World* the details of the atoms and lattice structures are the important information. In the *Emergent World* general concepts as the idea of quasiparticles and collective modes as phonons are the stating point for discussion.

1.1.1 Emergence in Condensed Matter Physics

In condensed matter physics, two philosophies are intertwined: the reductionist atomistic approach and the complimentary concept of emergent phenomena. We will see along this thesis how different constituents in materials can lead to different physical phenomena. Moreover, the way these constituents are assembled may play an important role in the determination of the ground state of the system. Despite this reductionist point of view, which suggests us that every single material should be considered independently, the emergent phenomena in condensed matter are usually very robust to perturbations and repeat themselves in materials with different constituents and geometry. Condensed matter physics is an area of research which explores both the reductionist and the emergent phenomena perspectives, see Fig. 1.1. Usually we cannot completely wash out all of the details of the problem we are interested in, but once we determine what is important for their description, the theories are able to account for the physics of entire families of materials.

At the scale of Angstroms, the basic bulging blocks of matter are atoms, entities that we understand reasonably well, but the knowledge of the properties of isolated atoms does not always give us the ability to infer the behavior of the systems they form when assembled together. As an illustration of this point, extending on the discussion in [2], here I mention a few examples of different phenomena that can emerge when atoms form a crystal. As a first

example, when atoms of gold assemble to form a face-centered cubic structure, they give rise to a ductile metal with resistivity of the order of $10^{-8} Ohm \cdot cm$, which we understand as a good example of a Fermi liquid. On the other hand, when carbon atoms assemble to form a diamond cubic structure, they give rise to an insulator with remarkable hardness and resistivity which can go up to $10^{+18} Ohm \cdot cm$. This difference of 26 orders of magnitude in transport properties is striking. Interestingly enough, carbon has many other allotropes, the most common being graphite, with very distinct properties. This is an example of how the constituent elements but also their assembly are decisive in determining the properties of materials. As a third example I mention niobium, a material that becomes a superconductor below the critical temperature of 9K. The understanding of how a material can transport current without dissipation required another level of understanding beyond the single particle description, with the idea of formation and condensation of Cooper pairs [3].

Let me go beyond the elemental materials, and look at systems of increasing complexity, involving binary, tertiary, and higher order compounds (see Fig. 1.2). For example, we can go from the elemental material Fe, a ferromagnet at room temperature (Curie temperature of 1043K [4]); to binary compounds such as MgB_2, a conventional type-II SC with a critical temperature (T_c) of 39K [5], amongst the highest in the family of conventional superconductors. As an example of a tertiary element, consider $CeRhIn_5$, a heavy fermion system which displays coexistence of magnetism and superconductivity [6, 7]. As a material with 4 different elements in its composition we have Bi_2NiMnO_6, which is has both ferromagnetic and ferroelectric properties at low temperatures [8]. Going further in this scale, we can find $HgBa_2Ca_2Cu_3O_8$, a high temperature superconductor in the family of the cuprates with the highest well established T_c of 133K [9]. Complexity, as it develops, reveals diverse and potentially useful emergent phenomena, taking us closer, for example, to the holy grail of room temperature superconductivity.

In this spirit this thesis will give examples on how the complimentary points of view of reductionism and emergence are both valid, providing different insights into our understanding of materials today.

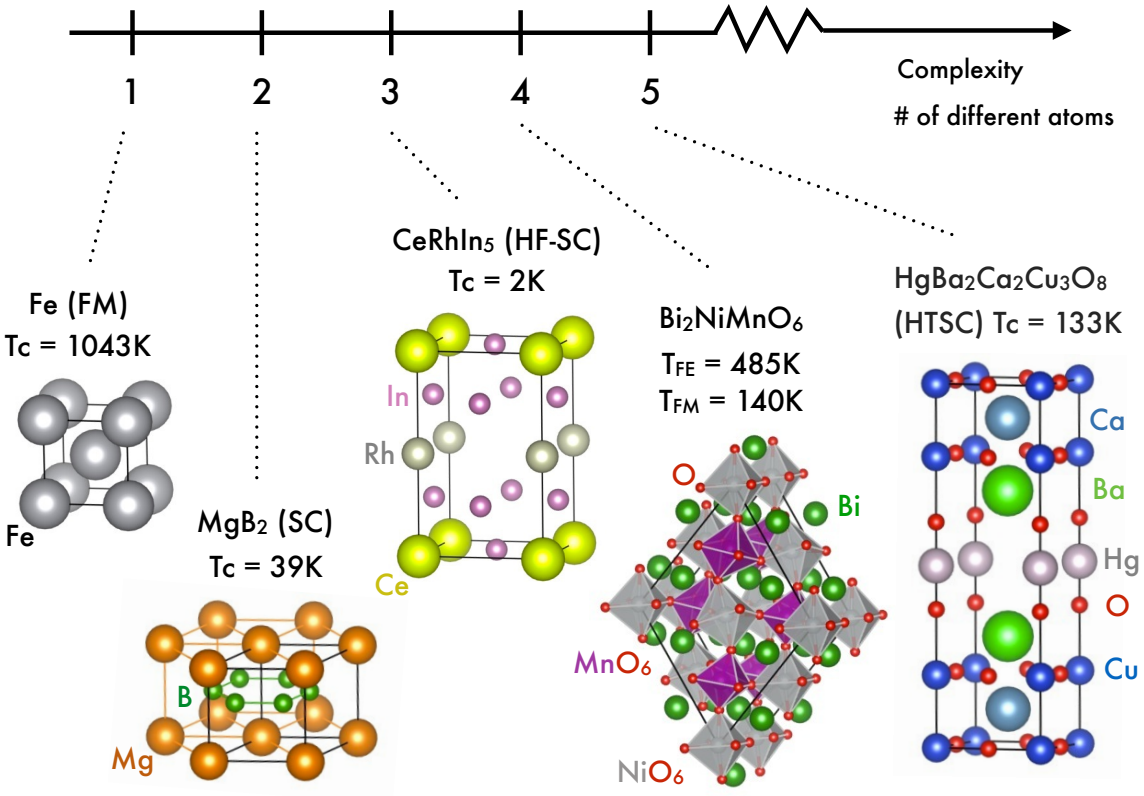

Figure 1.2: Examples of materials of increasing complexity (or number of different constituent atoms). Note the different kinds of phenomena that emerge with increasing complexity. See text for discussion and references. Figures generated by VESTA software [10].

1.2 Important Concepts in Condensed Matter Theory

In order to theoretically address condensed matter systems, if we start with a purely reductionist perspective we have a very tough problem: in principle we need to solve a many-body Schrödinger equation including all nuclei and electrons of the atoms in the material. The Hamiltonian should include kinetic terms and interactions, explicitly considering the Coulomb interaction amongst all the charges in the system. This problem becomes very hard analytically and computationally very expensive as the number of particles increase.

Within some approximations we can understand parts of this problem. Considering the electrons in a solid to be non-interacting and subject to a perfect and infinite periodic potential we can construct a band theory using a nearly free electron model in case of

extended orbitals as s and p or a tight-binding approximation for more localized orbitals, as d or f, based on the overlap of atomic wave-functions [11]. These approaches give good results for simple metals, but once interactions and correlations become important more powerful techniques need to be introduced.

In order to develop a more natural understanding of condensed matter phenomena, we would like to develop analytical approaches to the problems we are interested in. Towards this end, we need to establish a portfolio of key theoretical concepts that are helpful for the understanding of many-body systems. In the following subsections we briefly introduce some of these concepts.

1.2.1 The Landau Fermi Liquid Theory

The Landau Fermi liquid theory [12] gives us a framework to understand why the properties of a strongly interacting set of electrons are very similar to the properties of a Fermi gas, or a set of non-interacting electrons.

Given a Fermi surface, an abstract boundary in momentum space that separates the occupied from the unoccupied electronic states, Landau argued that an extra fermion near the Fermi surface has a very constrained space of states to scatter to, since it cannot scatter to the already occupied states inside the Fermi surface due to the Pauli exclusion principle [12]. Due to this constraint, he argued, that if one starts with the non-interacting problem and then adiabatically turns on the interactions, the states above the Fermi energy will evolve while maintaining a one-to-one correspondence with the original fermionic state, now called a *quasiparticle state* (see the right side of Fig. 1.1). Turning on the interactions effectively has the effect of renormalizing the original electronic parameters and consequently we have the same qualitative behavior as in a non-interacting Fermi gas.

The main properties of a Fermi liquid are: a specific heat which is linear in temperature, a temperature independent magnetic susceptibility and a resistivity that depends

quadratically on temperature:

$$C_v = \frac{\pi^2 k_B^2}{3} N^*(0) T, \tag{1.1}$$

$$\chi = \mu_B^2 \frac{N^*(0)}{1 + F_0^a}, \tag{1.2}$$

$$\rho \sim \rho_0 + AT^2, \tag{1.3}$$

where k_B is the Boltzmann constant, μ_B the Bohr magneton, ρ_0 a residual resistivity and A a coefficient which is proportional to square of the renormalized density of states at the Fermi level, which can be written as:

$$N^*(0) = \frac{m p_F}{\pi^2 \hbar^3}(1 + F_1^s), \tag{1.4}$$

m is the bare electron mass and p_F the momentum at the Fermi surface. F_0^a and F_1^s are Landau parameters, determined from a multipolar expansion of the interactions in terms of Legendre polynomials [13].

1.2.2 The Renormalization Concept

The renormalization group technique introduces a series of transformations to a given physical system so one can investigate its behavior at different length or energy scales [14]. It turns out that the low energy behavior of a system is usually only weakly dependent on the high energy physics and details of the Hamiltonian. This technique provides a systematic way to determine what are the relevant interactions at low temperatures. It can be implemented by a reduction of the cutoff energy scale in the problem, integrating out the states at higher energies and defining new effective models at lower energies. In this process the coupling constants of the given model are renormalized. Those coupling constants that tend to vanish under this procedure are said to be *irrelevant*; and those that become stronger under the renormalization group transformations are said to be *relevant*.

There are in fact many high energy Hamiltonians that will flow towards the same low energy Hamiltonian, or stable *fixed point*, meaning that they will have the same low energy physics (for example H_1, H_2, H_3 in Fig. 1.3). A fixed point is reached when the effective

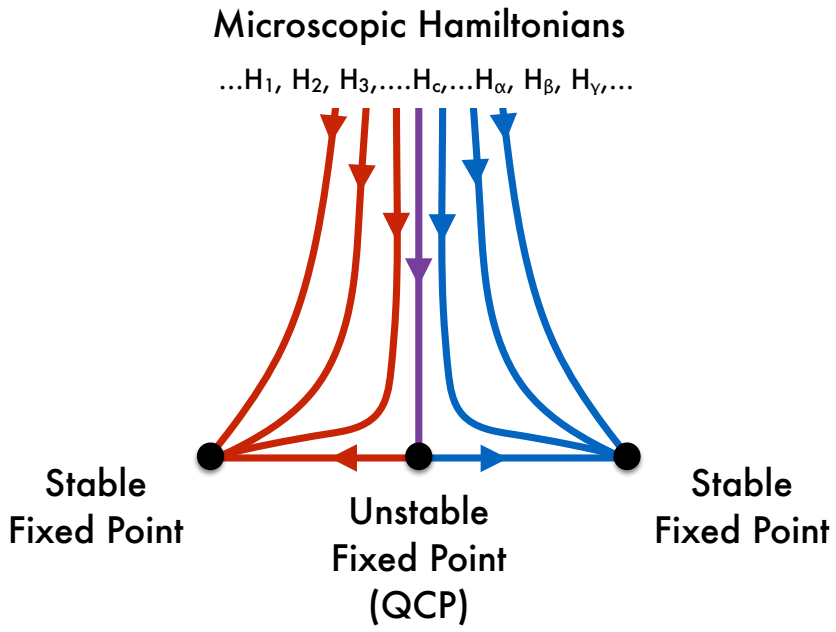

Figure 1.3: Schematic diagram for a renormalization group flow.

interactions transform into themselves under the renormalization group. On the other hand, for certain Hamiltonians or sets of coupling constants the problem may evolve to a different stable fixed point, describing a different phase of matter at low temperatures (as in $H_\alpha, H_\beta, H_\gamma$ in Fig. 1.3). In case one can continuously tune from one Hamiltonian in the first group to Hamiltonians in the second group, there will be one Hamiltonian, H_c, which flows between the two fixed points towards an *unstable fixed point*. As the name says, this kind of fixed point is unstable towards the flow to either of the stable fixed points under small perturbations (see Fig. 1.3), and it characterizes a *quantum critical point*.

The renormalization concept brings the idea of *universality*, the notion that many Hamiltonians have the same low energy physics and can be simplified if we are interested in studying the low energy phenomena. If the idea of universality did not hold, we would be lost looking into the details and complexity of each system and our simplified models would not be expected to capture the phenomena seen experimentally. In fact, universal exponents are usually experimentally observed in transport and thermodynamical properties.

Interestingly enough, the Kondo problem was the first problem in which the full renormalization group technique was applied [14]. The apparently simple problem of a single impurity embedded in a conduction sea is actually highly non-trivial due to the many-body nature of the conduction sea.

1.2.3 Landau Theory, Symmetry Breaking, Phases of Matter and Beyond

One way to characterize distinct phases of matter is to consider their symmetries. This idea can be made quantitative by the concept of an *order parameter*, a quantity which is zero in the phase that preserves the symmetries of the Hamiltonian and non-zero otherwise. One of the most iconic examples of an order parameter is the magnetization in a ferromagnet, associated with the breaking of spin rotational symmetry.

Landau theory was formulated in order to study continuous phase transitions between phases with different symmetries [15]. At high temperatures we usually find disordered phases which are symmetric, and below a critical temperature we find ordered phases in which some symmetry is broken. Landau theory is based on the construction of an energy functional in terms of the order parameter respecting the symmetries of the Hamiltonian. If the free energy functional has a minima when the order parameter is zero the system is in a disordered state, while if the minima occurs for a finite value of the order parameter we have an ordered state. Close to second order phase transitions, given the analyticity of the functional, the free energy can be expanded in powers of the order parameter and many of the properties of the phase transition can be inferred from it.

Experimentally it is possible to tune systems by pressure, magnetic field or doping, so that the critical temperature is driven to zero. In case this process is continuous and the transition second order, it gives rise to a *quantum phase transition* in which quantum fluctuations drive the change of state. At this point the coherence length diverges and fluctuations of the system in all length and time scales are important. The regions around quantum phase transitions are known to be interesting regions due to the possibility of the mergence of new phases of matter (see Fig. 1.4 for a cartoon of this concept). Experimentally one finds unusual phase coexistence and unconventional superconductivity around quantum

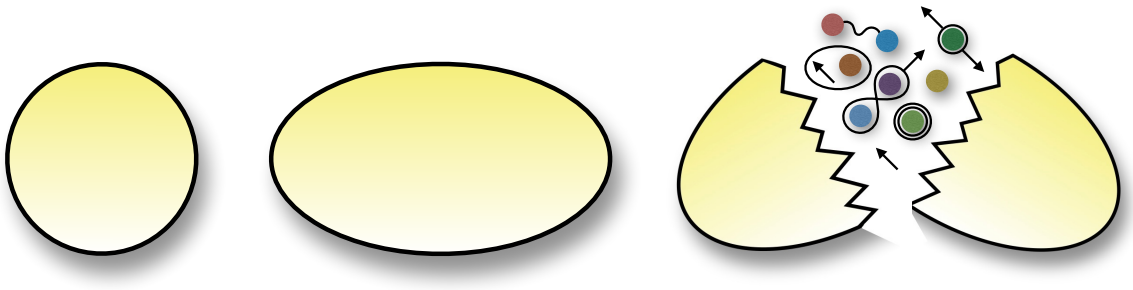

Figure 1.4: Symmetry breaking and the emergence of new phases of matter.

critical points and the ubiquitous non-Fermi liquid behavior above quantum critical points in strongly correlated materials, usually characterized by a logarithmic temperature dependence of the specific heat coefficient and unusual temperature dependence of the resistivity:

$$C_v \sim \log T, \tag{1.5}$$

$$\rho \sim T^{\alpha}, \quad \text{with } \alpha < 2. \tag{1.6}$$

It is important to point out that our current understanding on the classification of phases of matter actually goes beyond the traditional Landau symmetry breaking construction, now including a classification based on *topology*. Systems with topological order include quantum Hall [16] and spin liquid states [17]. In order to characterize such states one needs to look at new quantities such as ground state degeneracy or entanglement entropy [18].

1.3 Strongly Correlated Systems

Within condensed matter, strongly correlated systems are usually sets of electrons in which the strength of the interactions are comparable or larger then their kinetic energy. Electrons are charged particles and interact via the Coulomb interaction, which strength is inversely proportional to the distance between the charges. If we take atoms in empty space, their electrons are bound to the respective nuclei and in a state described by an atomic wave function with a given principal quantum number n and angular momentum l. The smaller the orbital (or the region in which the wave function has an appreciable weight), the more energetically expensive to fill orbitals with two electrons (one spin up and one spin down)

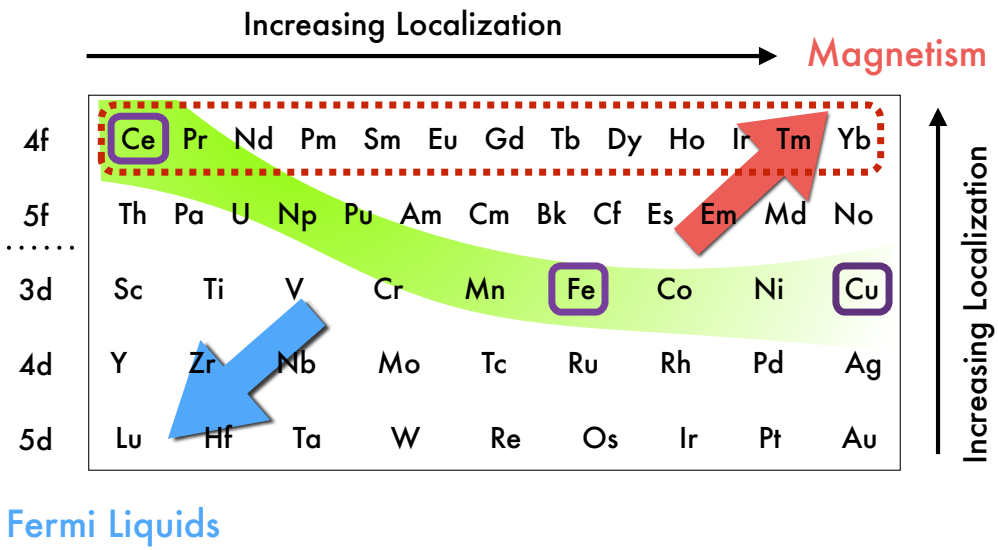

Figure 1.5: The Smith-Kmetko Diagram, adapted from [19]. This diagram organizes the elements in the periodic table in increasing order of localization, as indicated by the black arrows. Here we highlight with the red dotted line the elements usually present in heavy fermion systems which have very localized 4f-electrons. In the purple full line squares we point out the elements present in families of strongly correlated systems that are extensively studies today: Fe in the the iron pnictides and Cu in the cuprate superconductors and Ce in heavy fermions. See text for further discussion.

due to the Coulomb interaction, since these electrons need to "share" the same tight space.

Atoms with very localized orbitals are the drivers of new physics in strongly correlated systems. The trends on the degree of localization for intermetallic atoms is systematized in the Smith-Kmetko diagram [19], see Fig. 1.5, that essentially rearranges the rows of the periodic table of elements in increasing order of localization. The vertical trend can be understood as follows: for a given value of angular momentum l, as the quantum number n increases, the radial part of the wave-function gets more spread. This can be seen in the exponential dependence of the radial part of the hydrogenic wave function which follows $e^{-r/(na_0)}$, where $a_0 = \hbar^2/me^2$ is the Bohr radius. Within a particular row in the diagram, the increase in the nuclear charge leads to further reduction on the size of the orbitals. This can be understood by the definition of an effective Bohr radius $a_{Eff} = \hbar^2/mZe^2$, which takes into account the larger charge Ze in the nucleus, drastically reducing the region in which the wave-function has an appreciable weight.

The analysis of the Smith-Kmetko diagram can be extended to intermetallic compounds, as discussed in [19]. In the bottom left corner of the diagram (highlighted by the blue arrow) there are atoms with the most delocalized orbitals, which usually overlap when in a crystal, leading to itinerant compounds. These usually form good metals and are well described by the Fermi liquid theory, possibly with instabilities towards superconductivity at low temperatures. In the opposite corner of this diagram (highlighted by the red arrow) we have the most localized orbitals, which tend to not overlap when in a periodic array leading to the formation of local moments and the development of magnetism.

The materials that lie in the intermediate region (highlighted green) of the Smith-Kmetko diagram are particularly interesting; they are said to be "in the brink of localization" [20], and are the elements that drive the interesting behavior in many strongly correlated systems (for example, Ce, Fe and Cu, highlighted by purple squares). The electrons in atoms in this region are in between localized (magnetic) and delocalized (itinerant) behavior, and can usually be tuned from one regime to the other by small amounts of doping or pressure.

There are several classes of strongly correlated materials, with very rich phase diagrams, as shown artistically in Fig. 1.6. Here I will point out three families of materials in which the presence of d- or f-orbitals brings in interesting phenomena: the cuprate superconductors [21], which are currently the materials with the highest superconducting critical temperatures; the recently discovered Fe-based superconductors [22], with critical temperatures that can go up to 100K; and the heavy fermion systems, the family we will be focusing on in this thesis. The superconducting critical temperatures in heavy fermions are much lower if compared to the other families. This fact makes these systems not very appealing for technological applications, but at the same time the small energy scales make these systems more easily tunable, so we can have access to more detailed sets of experiments to build a more complete theoretical understanding. One interesting point to notice about these families of materials is that they show a recurrent theme: these systems usually display antiferromagnetic order, which can be suppressed by tuning the material by pressure,

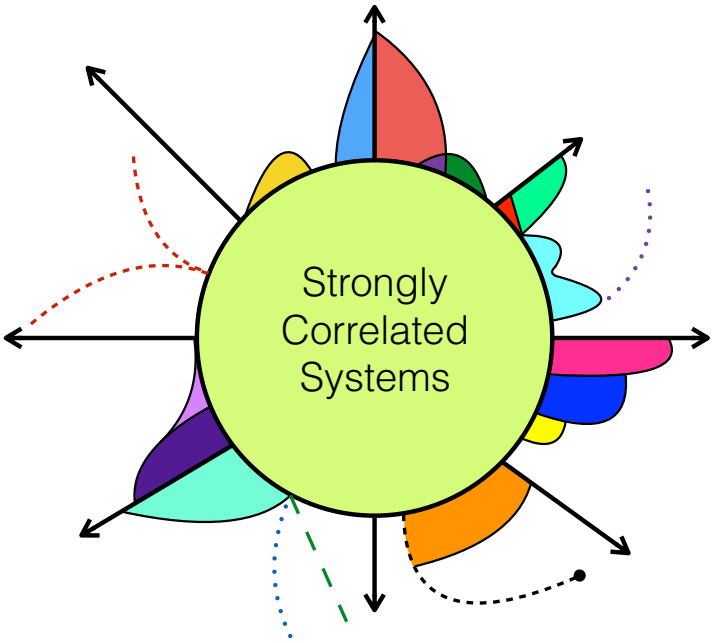

Figure 1.6: Strongly Correlated Systems. This figure artistically shows the richness of the phase diagrams of strongly correlated systems. It includes schematically phase diagrams of cuprate, Fe-based and organic superconductors and heavy fermion systems.

doping or magnetic field, with superconductivity often emerging in the vicinity of the antiferromagnetic quantum critical point and non Fermi liquid behavior is usually observed at finite temperatures above it. This is a direct consequence of the presence of elements with electrons in the brink of the localization.

1.4 Heavy Fermion Systems

Since their discovery [23], heavy fermion materials have provided a wealth of insights into correlated electron physics. These materials contain a matrix of localized magnetic moments formed from f-electrons immersed in a host metal; at low temperatures the spin-quenching entanglement of the f-moments with the conduction electrons gives rise to a diversity of ground-states, including anisotropic superconductors, Kondo insulators and Fermi liquids with quasiparticles with effective masses 100s to 1000s times larger than the bare electron mass [20, 24]. An important class of heavy fermion metals exhibit the phenomenon of quantum criticality, whereby upon tuning via pressure, doping or magnetic field through

a zero temperature second order quantum phase transition, they develop non-Fermi liquid behavior and predisposition to superconductivity [25, 26, 27].

1.4.1 Local moments and the Kondo effect

In order to introduce the idea of heavy fermions it is natural to first understand the concept of *local moments*. The simplest example of a local moment is an unpaired electron in a localized atomic orbital. At temperatures smaller than the ionization energy, the only degree of freedom that is left is the magnetic moment. The hallmark of the presence of local moments is a Curie-like behavior of the magnetic susceptibility at high temperatures with $\chi \sim 1/T$.

In solids, local moments usually come from impurities of $3d$ transition metal or $4f$ rare-earth elements. These impurities contribute to a Curie-like behavior of the magnetic susceptibility at high temperatures, but at low temperatures the magnetic susceptibility saturates to a constant value, indicating the formation of a Pauli paramagnet, as schematically depicted in Fig. 1.7. The screening of the local moments by the conduction electrons in the metal is the cause of the development of the paramagnetic state and this phenomenon is called the *Kondo effect*. The crossover temperature between the local moment behavior, in which the local spin is free, and the low temperature behavior, in which the local moment is entangled with the conduction sea, is known as the *Kondo temperature*.

1.4.2 The Anderson model: local moment formation and renormalization

The Anderson model was proposed in 1961, motivated by the study of local moments in metals, with the aim of understanding the necessary conditions for local moment formation [28]. The proposed model can be written as:

$$H = \sum_{\mathbf{k}\sigma} \epsilon_{\mathbf{k}} c^{\dagger}_{\mathbf{k}\sigma} c_{\mathbf{k}\sigma} + \epsilon_f \sum_{\sigma} f^{\dagger}_{\sigma} f_{\sigma} + U n_{f\uparrow} n_{f\downarrow} + V \sum_{\mathbf{k}\sigma} (c^{\dagger}_{\mathbf{k}\sigma} f_{\sigma} + f^{\dagger}_{\sigma} c_{\mathbf{k}\sigma}), \tag{1.7}$$

where the first term represents the host metal, a conduction electron system with dispersion $\epsilon_{\mathbf{k}}$; and the second term introduces the energy ϵ_f of a localized f-state in the impurity site. The third term represents the onsite Coulomb interaction between localized electrons in the

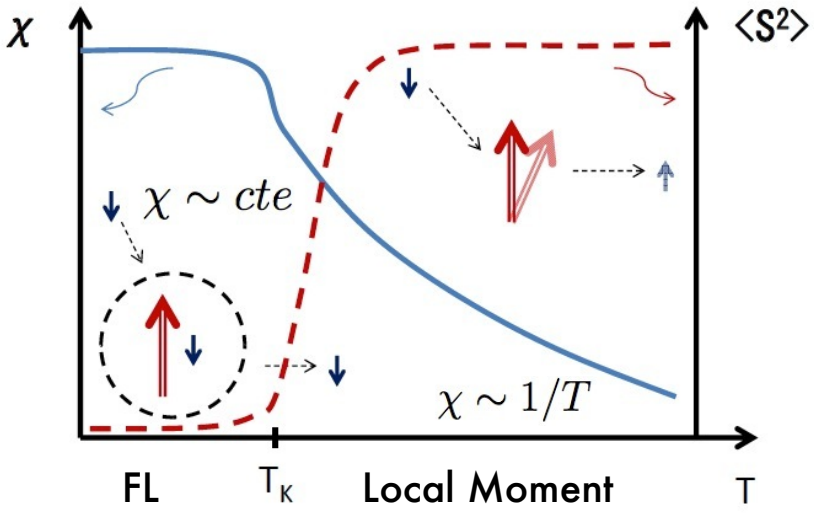

Figure 1.7: The behavior of local moments when immersed in a conduction sea. At high temperatures they behave as free local moments, with a Curie magnetic susceptibility, and at low temperatures they are screened by conduction electrons and the susceptibility goes to a constant. The temperature at which this crossover happens is the Kondo temperature.

impurity site with strength U, where $n_{f\sigma} = f^\dagger_\sigma f_\sigma$ is the number operator for a given spin state. The last term represents the hybridization between the localized and the conduction electrons, where V is proportional to the overlap of the wave functions of localized and conduction electrons.

Within this model there are three options for the occupation of the localized f-level: it can be empty, singly occupied (with spin up or down) or doubly occupied. In order for the system to develop local moments, the singly occupied states must be the lowest in energy. At high enough temperatures, the Anderson model admits valence fluctuations to empty or doubly occupied states, with the following energies:

$$\begin{aligned} f^1 \to f^2, \qquad & \Delta E_{II} = U + \epsilon_f > 0, \\ f^1 \to f^0, \qquad & \Delta E_I = -\epsilon_f > 0, \end{aligned} \tag{1.8}$$

what requires $\epsilon_f < 0$ for local moment formation. Under these conditions the reduction of the temperature or cutoff energy scale leads to two crossovers. The Coulomb interaction is usually one of the largest energy scales, what makes $\Delta E_{II} > \Delta E_I$, so the first crossover

happens when the temperature crosses ΔE_{II} and the fluctuations to double occupied states are suppressed. Materials in this regime are called *mixed valent* systems. The Hilbert space now is constrained to empty and singly occupied states and the effective Hamiltonian which describes the system at $T < \Delta E_{II}$ is known as the Infinite U Anderson Model:

$$H = \sum_{\mathbf{k}\sigma} \epsilon_{\mathbf{k}} c^{\dagger}_{\mathbf{k}\sigma} c_{\mathbf{k}\sigma} + \epsilon_f \sum_{\sigma} X_{\sigma\sigma} + V \sum_{\mathbf{k}\sigma} (c^{\dagger}_{\mathbf{k}\sigma} X_{0\sigma} + X_{\sigma 0} c_{\mathbf{k}\sigma}), \tag{1.9}$$

where $X_{\sigma 0}$, $X_{0\sigma}$ and $X_{\sigma\sigma}$ are Hubbard operators [29], which by construction eliminate double occupancy of the f-level from the description. A generic Hubbard operator is defined as $X_{pq} = |p\rangle\langle q|$, and in the Hamiltonian above we have:

$$X_{\sigma\sigma'} = |\sigma\rangle\langle\sigma'|, \tag{1.10}$$

$$X_{0\sigma} = |0\rangle\langle\sigma|, \tag{1.11}$$

$$X_{\sigma 0} = |\sigma\rangle\langle 0|. \tag{1.12}$$

Reducing the temperature further, below ΔE_I, fluctuations to empty states are also supressed and the Hilbert space is restricted to the singly occupied states. Note, though, that there can still be virtual fluctuations due to the hybridization with the conduction sea:

$$\begin{aligned} c_{\uparrow} + f^1_{\downarrow} &\rightleftharpoons f^2 \rightleftharpoons c_{\downarrow} + f^1_{\uparrow}, \\ c_{\uparrow} + f^1_{\downarrow} &\rightleftharpoons c_{\uparrow} + c_{\downarrow} \rightleftharpoons c_{\downarrow} + f^1_{\uparrow}, \end{aligned} \tag{1.13}$$

which can flip the spins of the conduction and localized electrons. Within second order perturbation theory these virtual fluctuations will selectively lower the energy of the singlet configuration, what leads to an effective antiferrromagnetic interaction between the conduction and localized electron spins. The effective Hamiltonian is now:

$$H = \sum_{\mathbf{k}\sigma} \epsilon_{\mathbf{k}} c^{\dagger}_{\mathbf{k}\sigma} c_{\mathbf{k}\sigma} + J_K \mathbf{S} \cdot \mathbf{s}(0), \tag{1.14}$$

where $\mathbf{S}$ is the spin operator for the f-electron and $\mathbf{s}(0)$ is the conduction electron spin

density at the impurity site; $J_K \sim V^2/U$ is known as the Kondo coupling. This Hamiltonian was originally called the s-d Model [30], but it started being called the Kondo model, after its use by J. Kondo to solve the resistivity minima problem [31, 32].

1.4.3 Renormalization in the Kondo model

Under further reduction of the temperature one can analyze what is the behavior of the couplings in the Kondo model. From a renormalization group analysis the beta function, which dictates how the coupling constants of the theory flow under renormalization, has the following form:

$$\frac{\partial g}{\partial \log \Lambda} = \beta(g) = -2g^2 + O(g)^3, \tag{1.15}$$

where $g = N(0)J_K$, with $N(0)$ the density of states of the conduction electrons at the Fermi level, J_K the Kondo coupling, and Λ the cutoff energy scale, which can be understood as the temperature at which we are analyzing the system. Given that the beta function is negative, the coupling constant $N(0)J_K$ increases as one reduces the cutoff energy Λ so the problem renormalizes to strong coupling and as a consequence the local moment forms a singlet bound state with a conduction electron spin, therefore getting quenched. The Kondo temperature can be estimated from the renormalization group equation above, as the energy scale at which the coupling g diverges:

$$T_K \sim \frac{1}{N(0)} e^{-1/2N(0)J_K}. \tag{1.16}$$

1.4.4 The Kondo lattice Model: the onset of coherence and the large-N approach

Metals with a small concentration of magnetic impurities display a logarithmic upturn in the resistivity around the Kondo temperature, as understood by Jun Kondo [31], followed by a saturation at lower temperatures with the formation of singlets and an effective Fermi liquid [33]. With the increase in the concentration of impurities we see a downturn in the resistivity at low temperatures, which indicates the development of coherent scattering,

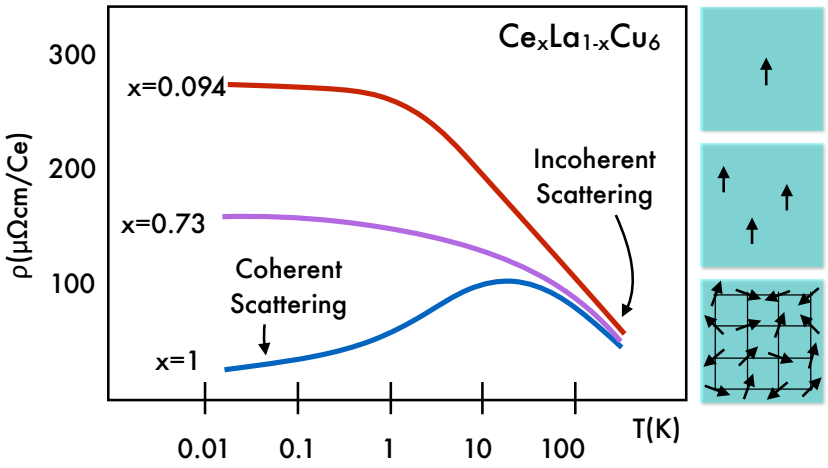

Figure 1.8: Temperature dependence of the resistivity for $Ce_xLa_{1-x}Cu_6$, adapted from [34]. When x is small we have the characteristic behavior of the resistivity in presence of dilute local moments. When $x = 1$ there is a local moment in every site of a lattice and the formation of a coherent state between the conduction electrons and local moments, with the corresponding decrease in resistivity.

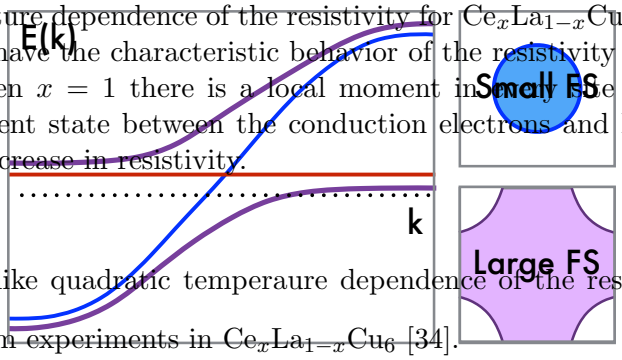

with a Fermi liquid-like quadratic temperaure dependence of the resistivity, as shown in Fig. 1.8, adapted from experiments in $Ce_xLa_{1-x}Cu_6$ [34].

The development of coherence can be understood within the Kondo lattice model:

$$H = \sum_{\mathbf{k}\sigma} \epsilon_{\mathbf{k}} c^\dagger_{\mathbf{k}\sigma} c_{\mathbf{k}\sigma} + J_K \sum_i \mathbf{S}_i \cdot \mathbf{s}_i, \tag{1.17}$$

in which there is a local moment in every site of a lattice, resonantly scattering conduction electrons, what leads to a strongly renormalized electronic band, which is said to be heavy because the effective mass of the quasiparticles are usually 100s to 1000s of times larger than the bare electron mass.

The treatment of this model within a path integral formalism is non-trivial due to the presence of the spin operators which are not canonical and consequently Wick's theorem does not apply [35]. In order to proceed with this kind of treatment, one can write the spin operators in terms of the canonical creation and annihilation operators $f^\dagger_\alpha$, f_α:

$$\mathbf{S}_F = \sum_{\alpha\alpha'} f^\dagger_\alpha \frac{\boldsymbol{\sigma}_{\alpha\alpha'}}{2} f_{\alpha'}, \tag{1.18}$$

where $\boldsymbol{\sigma}$ are the Pauli matrices in case of an SU(2) spin-1/2 operator. This form of the spin operator requires a constraint to restrict the four-dimensional fermionic Hilbert space down to the original two-dimensional space of spin states. The constraint for a SU(2) spin-1/2 is requires fixing $n_F = 1$ (see Chapter 4 for a detailed discussion).

Given the absence of a natural small energy scale in the problem, one cannot apply perturbative methods in the interactions, and in this case large-N approximations are very suitable. Large-N approaches were first introduced in particle physics [36], and are now extensively used in condensed matter physics. P. W. Anderson [37] proposed this kind of approach in the context of condensed matter physics based on the large spin degeneracy $N = (2j + 1)$ of the spin-orbit coupled f-electrons, which provides a natural small parameter $1/(2j + 1)$. This approach was successfully applied to the Kondo [38] and Anderson [39, 40] models and also to Heisenberg models [41]. The large-N approximations usually generalize the symmetry group of the spin (or the number of flavors of the fermionic operators introduced above) from SU(2) to SU(N) and allows the development of mean field theories, which are exact in the $N \to \infty$ limit, and the systematic inclusion of corrections in $1/N$. In the path integral formalism all possible filed configurations are summed over, weighted by e^{-iS}, where S is the action which is extensive in N in the large-N approach. If one now identifies $1/N$ with $\hbar$, we can understand this approach as a kind of semiclassical approximation [13].

Within a path integral formalism, one can perform a Hubbard-Stratonovich transformation [42] in order to decouple the interacting Kondo term, which now is a four-fermion term. This transformation introduces a fluctuating variable V which hybridizes conduction and f-electrons. In the large-N limit, the solution is dominated by the saddle point, which can be determined self-consistently by the minimization of the free energy with respect to the fluctuation fields introduced by the Hubbard-Stratonovich transformation. The constraint can be implemented by the introduction of the Lagrange multiplier λ, adding the term $\lambda(n_F - 1)$ to the Hamiltonian so that when the solution is minimized with respect to λ the constraint condition is satisfied. This kind of calculation will be explicitly performed in the following chapters of this thesis. In summary, one finds as solution two hybridized bands

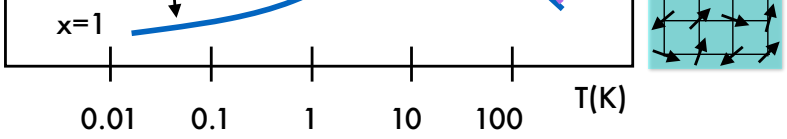

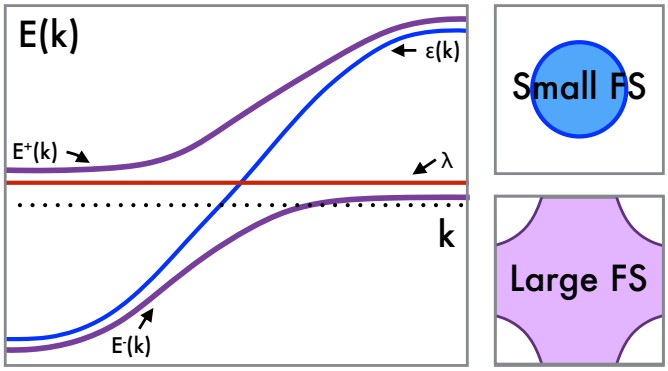

Figure 1.9: Schematic picture of the bare conduction band (blue) and f-electron level (red). The chemical potential is make with the dotted line. Once the hybridization develops there is the development of two hybrid bands (purple). The respective Fermi surfaces are indicated on the right: small Fermi surface for the conduction electrons and a large Fermi surface for the hybrid bands.

following:

$$E_{\mathbf{k}}^{\pm} = \frac{\epsilon_{\mathbf{k}} + \lambda}{2} \pm \sqrt{\left(\frac{\epsilon_{\mathbf{k}} - \lambda}{2}\right)^2 + V^2}, \tag{1.19}$$

where λ is the Lagrange multiplier introduced to enforce the constraint to singly occupied states, which has the role of the effective f-electron energy level. Note the development of a large Fermi surface, with contributions from both conduction and f-electrons below a coherence temperature, as depicted in Fig. 1.9.

1.4.5 Competition of energy scales

In the lattice limit, the Kondo temperature is not the only energy scale. Now there is an effective spin-spin interaction between the local moments mediated by the conduction electrons which introduces a new scale to the problem, the RKKY temperature, after Ruderman, Kittel, Kasuya and Yosida [43]. In Fig. 1.10 one can see that as the local moment on the left interacts with the conduction electrons by an antiferromagnetic exchange, it polarizes the conduction electrons surrounding it. Due to the sharp discontinuity of the occupation number around the Fermi surface the polarization of the spin of the conduction electrons actually follows an oscillating function with period $2k_F$ that decays asymptotically

as $1/(k_F r)^3$. This polarization will affect other local moments nearby by their antiferromagnetic exchange. The net effect can be thought as an effective interaction between the local moments, which can be either ferro or antiferromagnetic, depending on the interplay between $2k_F$ and the distance between the local moments (the lattice constant in the case of the lattice problem). As a second order process the energy scale associated with this interaction is:

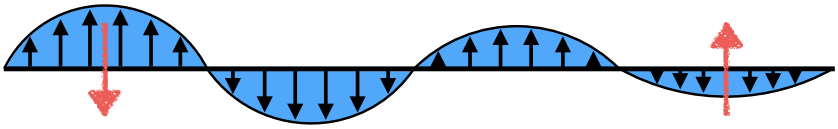

Figure 1.10: Schematic picture on the origin of the RKKY interaction.

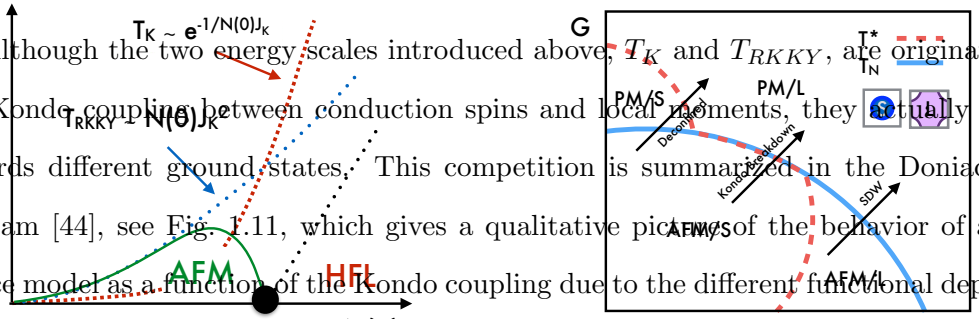

Although the two energy scales introduced above, T_K and T_{RKKY}, are originated from the Kondo coupling between conduction spins and local moments, they actually compete towards different ground states. This competition is summarized in the Doniach phase diagram [44], see Fig. 1.11, which gives a qualitative picture of the behavior of a Kondo lattice model as a function of the Kondo coupling due to the different functional dependence of the two energy scales on J_K. For small J_K, the RKKY scale dominates and the system becomes antiferromagnetic, but as J_K increases, above a critical value the Kondo scale is the dominant one and the system forms a heavy Fermi liquid. The Doniach picture is essentially a comparison of energy scales, and it does not tell us how the heavy Fermi liquid actually develops from the local moment antiferromagnetic state. It is important to notice that from the crude analysis of this picture the phase transition between the antiferromagnetic and heavy Fermi liquid phases occurs for $T_K \sim T_{RKKY}$, meaning $N(0)J_K \sim O(1)$. This estimate is in conflict with the condition of local moment formation ($U > U_C = \pi^2 N(0)V^2$, see [13]). This apparent inconsistency is solved once one considers the high degeneracy of the electrons in f-orbitals due to the strong spin-orbit coupling, which renormalizes T_K, but not T_{RKKY}, favoring the formation of the heavy fermion state [13].

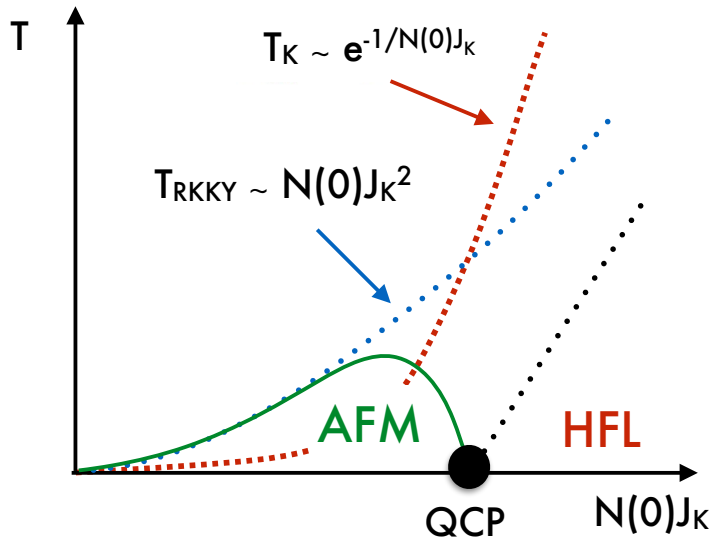

Figure 1.11: The Doniach phase diagram.

1.4.6 Quantum Criticality in Heavy Fermions

As suggested by Doniach [44], and later verified by experiments in several heavy fermion materials, there is a quantum critical point in the generic phase diagram of heavy fermions once the system is tuned at zero temperature by some external parameter such as pressure, magnetic field or chemical doping, leading to a change in the coupling $N(0)J_K$. As already defined, a quantum critical point is a critical point at zero temperature and the region of the phase diagram at finite temperature right above the quantum critical point is dominated by quantum fluctuations.

Fig. 1.12 illustrates the behavior observed in the archetypal quantum critical material $YbRh_2Si_2$ [45, 46]. A new energy scale, T^*, not predicted by Doniach, is shown in Fig. 1.12. To the left of the T^* line the Fermi surface is small and the local moments are not screened by the conduction electrons; while to the right of the T^* line the conduction and f-electrons are entangled in a singlet many-body state and the Fermi surface is large. The T^* line can be thought of as a the line that marks the localization-delocalization crossover of the f-electrons.

The large diagram in Fig. 1.12 shows the schematic phase diagram for pure $YbRh_2Si_2$.

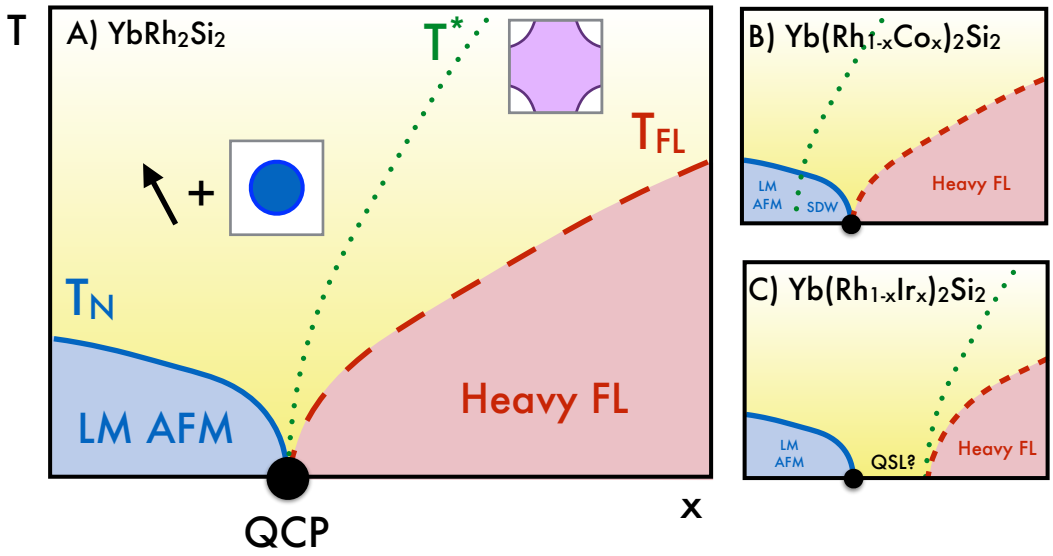

Figure 1.12: Schematic phase diagram for heavy fermions, based on experiments on $YbRh_2Si_2$, as a function of the running parameter x [45]. A) Pure $YbRh_2Si_2$; B) Co-doped, or compressed; C) Ir-doped, or expanded. The energy scales indicated in the diagrams are the following: T_N is the Néel temperature which characterizes the transition from the antiferromagnetic to a paramagnetic state; T_{FL} is a crossover temperature below which Fermi liquid behavior is verified, with a T^2 dependence of the resistivity; and T^* is the temperature across which the Hall coefficient has a crossover that sharpens up as the temperature is lowered, indicating a discontinuity in the Fermi surface properties at zero temperature.

One interesting feature of this diagram is the fact that the energy scales mentioned above all collapse to zero at the quantum critical point, and when this happens we have what has been called a *Kondo breakdown* quantum critical point [47, 48]. By contrast, when $YbRh_2Si_2$ is doped with Ir or Co, leading to expansion or compression of the material, respectively, these lines no longer coincide. The top right figure illustrates the case of the Co-doped or compression, in which case the T^* vanishes inside the antiferromagnetic phase. In this case the magnetic state is believed to emerge as an instability of a large Fermi surface, and the quantum critical point is characterized by a *spin density wave* quantum critical point [49]. On the other hand, when Rh is substituted by Ir, or the system expanded, as illustrated in the bottom right of Fig. 1.12, the antiferromagnetic phase is suppressed towards a phase in which the local moments are neither hybridizing with the conduction electrons nor forming a magnetically ordered state. The intermediate phase in between the antiferromagnetic and heavy Fermi liquid regions is believed to host a quantum spin liquid state, which is more

likely to occur in frustrated systems, and seems to fit within a *deconfined quantum criticality* scenario [50, 51]. An interesting property of the energy scales above (at least for $YbRh_2Si_2$) is that T_N is very sensitive under volume changes, while T^* is only weakly dependent [45].

From the experimental study of $YbRh_2Si_2$, it became apparent that the nature of the quantum phase transitions in heavy fermions is not unique and cannot be fully accounted for by the Landau paradigm, which purely analyzes how the order parameter behaves around the transition. Now magnetism can emerge from the magnetic exchange between local moments or as an instability of a heavy Fermi liquid [26]. The T^* line introduces a new energy scale that separates both possibilities, and characterizes the modification in the quasiparticle character and possibly of the quantum phase transition as well.

Recently, the Doniach diagram was generalized to what has been called the *Global phase diagram*, see Fig. 1.13. The horizontal axis governs the ratio of the Kondo and RKKY energy scales, while the new axis G gives a measure of the amount of quantum fluctuations in the material [52, 53, 54]. Quantum fluctuations are known to be enhanced in the presence of geometric frustration (as in the Kagome lattice, see the left of Fig. 1.14) or frustrated interactions (as in the Shastry-Suterland lattice, see the right of Fig. 1.14); or by the reduction of dimensionality, in which case the magnitude of a given spin is reduced by quantum fluctuations by an amount of the order $1/2z$, where z is the coordination number of the given lattice [55]. Along this new direction, for small Kondo coupling, the system will usually develop some kind of magnetic order. One can then increase the amount of frustration so that the magnetic order is suppressed, leading to exotic phases as the spin liquid of valence bond solid phases [54].

This new diagram provides a framework for understanding the interplay of zero-point spin fluctuations and the Kondo effect. In Fig. 1.13, we see two lines discussed above: T_N which indicates the transition from an antiferromagnetic state to a paramagnetic state, and T^* which indicates the transition from small (S) to large (L) Fermi surface. The arrows indicate different ways one can go from the antiferromagnetic region to the paramagnetic region. The middle arrow corresponds to the Kondo breakdown picture, with T_N and T^* coinciding; the rightmost arrow indicates a spin density wave kind of transition and

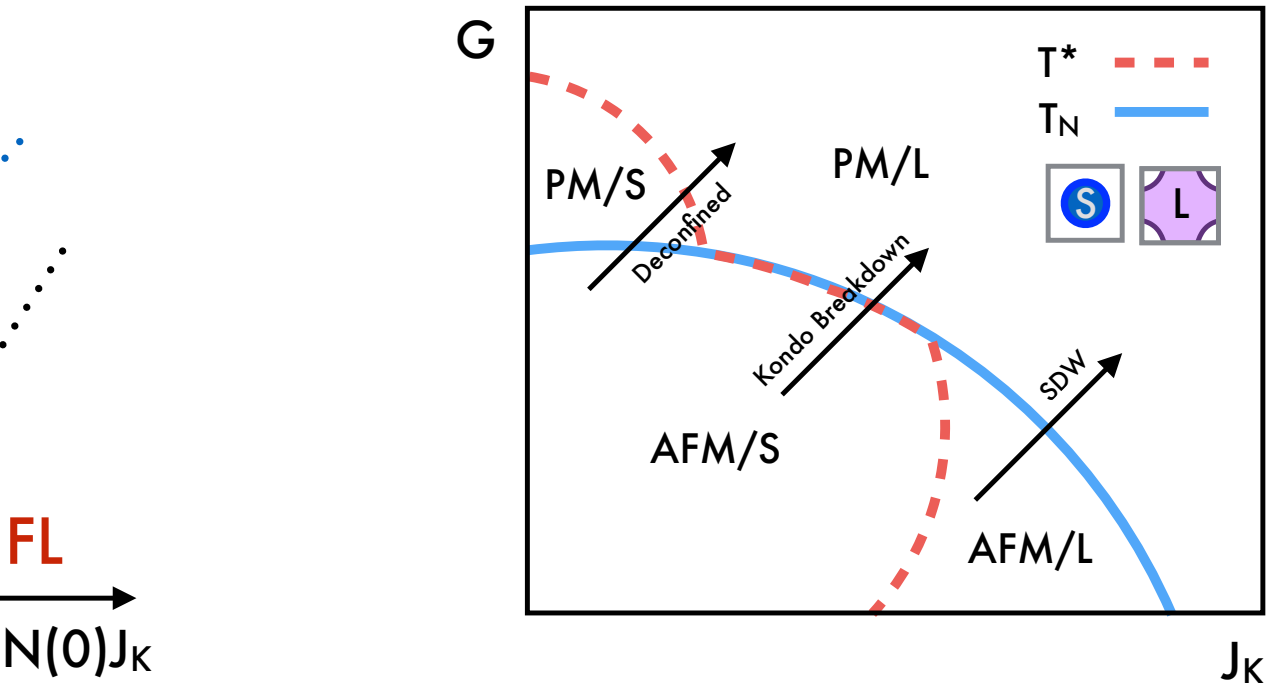

Figure 1.13: Global phase diagram for heavy fermions, adapted from [53]. T_N indicates the transition from an antiferromagnetic state (AFM) to a paramagnetic state (PM) and T^* indicates the transition from small (S) to large (L) Fermi surface. The black arrows indicate different ways to go from the antiferromagnetic phase to the paramagnetic phase, and can be associated with different theoretical proposals, see Section 1.4.8 for discussion.

the uppermost arrow indicates a path with a lot of frustration in which the system goes through an intermediate exotic state as a spin liquid before going to the heavy fermion state with a large Fermi surface. The mentioned theoretical proposals are briefly discussed in Section 1.4.8.

1.4.7 Unusual behavior in heavy fermions

In this subsection we highlight some recent experimental developments that we believe deserve attention due to their unusual features.

We start highlighting some of the most studied heavy fermion materials:

- **$YbRh_2Si_2$:** This system was already introduced above, and it is perhaps one of the best characterized heavy fermion materials due to the interest on its quantum critical

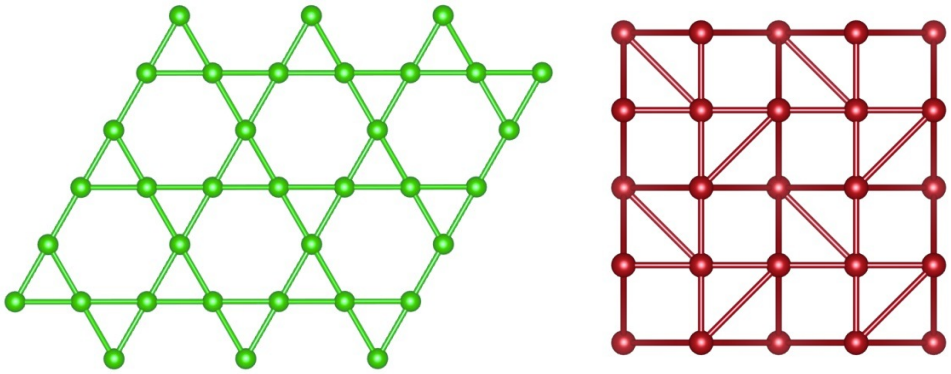

Figure 1.14: Frustrated Structures. Left: Kagome Lattice. Right: Shastry-Sutherland Lattice.

behavior. This material can also be doped, allowing experimentalists to explore great part of its phase diagram, as discussed in Section 1.4.6 above. This is the second Yb-based heavy fermion superconductor with the remarkably low critical temperature of $T_c \sim 2mK$ [56]. At the magnetic field tuned quantum critical point this system is known for displaying a linear temperature dependence of the resistivity, a logarithmically divergent specific heat coefficient and magnetic susceptibility $\chi \sim T^{3/4}$ at low temperatures [45];

- **$CeCu_{6-x}Au_x$:** The heavy fermion $CeCu_6$, when doped with Au with $x \sim 0.1$ displays logarithmic temperature dependence of the specific heat coefficient and linear temperature dependence of the resistivity, two indications of non Fermi liquid behavior [57]. This critical behavior fits in a 2D Spin density wave scenario (see discussion below), but recent neutron scatting and bulk magnetometry measurements have shown that the character of the quantum phase transition cannot be accounted for in this scenario, since it displays E/T scaling and the magnetic fluctuations are local in character [58].

- **$CeRhIn_5$:** This Ce-based heavy fermion is an antiferromagnet under ambient conditions, but when tuned by external pressure the magnetic phase is suppressed and superconductivity emerges around the antiferromagnetic quantum critical point [7]. There is evidence for microscopic coexistence of homogeneous magnetism and superconductivity in this system from nuclear quadrupolar resonance experiments [59];

Now we introduce some materials known to be intrinsic quantum critical:

- **β-$YbAlB_4$:** This material is believed to be an intrinsically quantum critical intermediate valent heavy fermion [60, 61]. Without tuning by external parameters β-$YbAlB_4$ exhibits non-Fermi liquid behavior, with a $T^{3/2}$ temperature dependence of the resistivity and a $T^{-1/2}$ divergence of the magnetic susceptibility and specific heat coefficient. A magnetic field induces an immediate cross-over into a Fermi liquid with a T^2 resistivity and a susceptibility which diverges as $B^{-1/2}$. Scaling of the free energy in T/B has been observed over 4 decades in T/B, pin-pointing the critical magnetic field within ± 0.1 mT of zero and demonstrating that the field-induced Fermi temperature is the Zeeman energy [61]. While the quantum critical properties are strongly dependent on the presence of magnetic field, the quantum critical point seems to be very robust against pressure [62]. Another interesting fact to point out is that this system has a polymorph, α-$YbAlB_4$, which has local structure similar to β-$YbAlB_4$, but does not display quantum critical behavior [61]. Interestingly enough β-$YbAlB_4$ is the first Yb-based heavy fermion superconductor, albeit with a very low transition temperature $T_c \sim 80mK$ [60]. This compound motivated great part of this work and we will introduce more details of its properties along this thesis;

- **$Au_{51}Al_{34}Yb_{15}$ Quasicrystal:** This quasicrystal also displays intrinsic quantum critical behavior. Experiments verified a diverging susceptibility $\chi \sim T^{-1/2}$ and specific heat coefficient $\gamma \sim \log T$ at low temperatures. As for β-$YbAlB_4$, the critical regime is very robust against hydrostatic pressure but it is immediately suppressed in the presence of magnetic field. The similarities with β-$YbAlB_4$ go further: this material is also intermediate valent and has a polymorth, in this case a crystalline approximant, $Au_{51}Al_{35}Yb_{14}$, which is not quantum critical [63]. From experiments on the nuclear spin relaxation rate $1/T_1T$ (which measures magnetic fluctuations averaged over momentum) and static magnetic susceptibility χ (which measures fluctuations at zero wave vector), it was noticed that $1/T_1T \propto \chi$, what suggests that the fluctuations related to quantum criticality in this system are local in nature [63];

- **CeRhSn:** More recently, intrinsic quantum criticality was also observed in CeRhSn, inferred from the divergence of the Grüneisen ratio[1] [64]. In this material the Ce atoms are located in a Kagome structure (see the left of Fig. 1.14), suggesting that frustration might play an important role in the determination of the ground state of this system. The non Fermi liquid behavior above the critical point is characterized by a resistivity with temperature dependence $T^{3/4}$, magnetic susceptibility $\chi \sim T^{-1/2}$ and a logarithmically divergent specific heat coefficient below $0.1K$ [64, 65]. In this material the Kondo temperature is of the order of $200K$, indicating it is in a valence fluctuation regime. For pressure applied along the c-axis no deviation from the critical behavior is observed, whereas when pressure is applied in plane, distorting the Kagome structure and relieving frustration, the quantum critical behavior is suppressed [64];

- **$Pr_2Ir_2O_7$:** This material is a pyrochlore iridate and another example of a frustrated Kondo lattice material, in which the Pr ions are located in the edges of corner-sharing tetrahedra [66]. Experiments suggest that the system has a chiral spin-liquid ground state, formed due to the interplay between the Kondo effect and frustrated magnetic interactions. Scaling of the magnetic Gruneisen ratio as $\Gamma_H H \sim f(T/H^{4/3})$ is verified indicating the presence of a zero field quantum critical point [2];

Recently new usual behavior was also verified in:

- **CePdAl:** This geometrically frustrated compound has Ce atoms placed in a Kagome structure (see the left of Fig. 1.14). It displays what has been called a partially ordered state. Neutron scattering experiments observe a state in which one third of the Ce moments do not participate in the long-range order and the other two thirds form a 2D magnetic structure [67].

- **YbPtBi:** The phase diagram of this system displays three phases at low temperatures: for fields up to about $4kOe$ an antiferromagnetic phase is observed; as the magnetic field increases, magnetic order is suppressed and a non-Fermi liquid state with $\rho \sim$

[1] The Grüneisen ratio is defined as $\Gamma = \beta/C$, where β is the volume thermal expansion and C the specific heat.

[2] The magnetic Grüneisen ratio is defined as $\Gamma_M = -(dM/dT)/C$, where M is the magnetization and C the specific heat.

$T^{3/2}$ is present up to fields of about $8kOe$, above which a heavy Fermi liquid is observed [68]. The phase diagram in this case is similar to the phase diagram C) in Fig. 1.12.

- **$YbNi_4P_2$:** This material is a heavy fermion metal which orders ferromagnetically below $0.17K$. Its crystal and electronic structures are quasi-1D, suggesting strong quantum fluctuations [69]. At low temperatures this systems displays linear temperature dependence of the resistivity and unusual power law behavior of the specific heat $C/T \sim T^{-0.42}$, indicating the presence of non Fermi liquid behavior [69].

1.4.8 Previous Theories

Now we proceed to make a short summary of the available theories and their ability to account for what is observed experimentally in heavy fermion systems. The main open questions focus on the origin and nature of the quantum critical regime and the non Fermi liquid it gives rise to.

- **Spin Density Wave Scenario**: This theory is based on the Hertz-Millis-Moriya formalism [49] and characterizes quantum critical points between a metallic magnetic phase and a metallic paramagnetic phase. Here magnetism emerges as an instability of the Fermi surface, what is favored by nesting. Within heavy fermions this theory assumes that the f-electrons are delocalized in both sides of the transition.

  The Hertz-Millis-Moriya formalism extends the study of critical phenomena to quantum systems. In classical continuous phase transitions, the system becomes ordered below a given critical temperature at which the correlation length ξ_r diverges. In continuous quantum phase transitions the system is at zero temperature and a second parameter x is tuned to drive the system through a transition at the critical value x_c. At this point the correlation length ξ_r and correlation time ξ_τ diverge, and the dynamical critical exponent z dictates how the time dimension scales with respect to the spacial dimensions $\xi_\tau = \xi_r^z$. For the case of antiferromagnetism $z = 2$ and in $d = 3$ we are above the upper critical dimension and mean field results should hold. The predictions for a 3D antiferromagnet include $C/T \sim T^{(d-z/z)} = \sqrt{T}$, no anomalous exponent for the magnetic susceptibility, resisitivity following $\rho \sim T^{3/2}$. Within this

formalism the quasiparticles are well defined in the Fermi surface with the exception of the hot lines along the Fermi surface, where they are critically scattered by the magnetic fluctuations, so the transport is expected to be dominated by a Fermi liquid behavior. Some materials seem to fall into variations of this description, with the assumption of reduced dimensionality usually associated with frustration. In case of $d = 2$ we have $C/T \sim \log T$ and $\rho \sim T$ [70], as observed in $CeCu_{6-x}Au_x$ [71].

Note that this scenario cannot generally account for the anomalous transport properties as linear resistivity in 3D. Also, despite the fact that some materials seem to follow a spin density wave behavior, it is known that the antiferromagnetism is not always itinerant in heavy fermion systems, so this description would not hold for all observed quantum critical points. In terms of the diagram in Fig. 1.12, this scenario accounts only for the B) type of quantum phase transition.

- **Local Quantum Criticality or Kondo Breakdown Scenario**: The classical theory of phase transitions involves the divergence of the correlation length in space at the quantum critical point. As briefly discussed above, Hertz introduces the time dimension for the study of quantum phase transitions; now correlations diverge also in time at the phase transition. An intriguing proposal involves the coexistence of local degrees of freedom, which have correlations that diverge only in time and not in space, with the traditional long wavelength critical degrees of freedom. This proposal was called *local quantum criticality* [47, 48].

  This idea was explored within an extended dynamical mean field theory (EDMFT) approach for the Kondo lattice model and introduces a new energy scale E_{Local}, as an effective Fermi energy scale. When this energy scale vanishes the Kondo screening becomes critical. This approach is able to find two kinds of quantum phase transitions: first, when magnetic order is suppressed and E_{Local} is finite, a spin density wave type of critical point is expected. Another possibility involves the suppression of both T_N and E_{Local} energy scales at the same time, in which the Kondo screening turns critical at the magnetic quantum critical point, which is the so called Kondo breakdown scenario.

  Here we note that this approach naturally accounts for E/T scaling but seems to be

valid only in 2D. Also, the approximation within the EDMFT involves the assumption that the self-energies are local, or momentum independent. At the same time that this seems to be a weak point of the theory, this approach naturally finds the local quantum critical behavior that seems to account for the critical phenomenology in several heavy fermion systems as in $YbRh_2Si_2$ and depicted in Fig. 1.12 A). The fact that the self-energy is local in this approach might give us a hint to understand the unusual quantum critical behavior in these systems.

- **Deconfined Quantum Criticality**: The concept of deconfined quantum critical points was proposed as a new paradigm for quantum criticality, which goes beyond the Landau framework in terms of order parameters. In this scenario the critical theory contains emergent gauge fields which mediate interactions between fractionalized quasiparticles [50, 51]. This scenario was explored on phase transitions between magnetically ordered states and exotic phases as valence bond solids and spin liquids, and is more likely to be realized in systems with magnetic frustration. In principle this scenario would account for phase diagrams as the one depicted in Fig. 1.12 C), but specific predictions on the anomalies in the thermodynamics and transport properties are not clear from the available theoretical work.

- **Two-fluid picture**: This is a phenomenological picture for heavy fermion systems, first proposed based on the analysis of the specific heat and magnetic susceptibility of $CeCoIn_5$ [72]. The two fluids consist of: 1) a lattice of non interacting Kondo centers and 2) a coherent state formed by the local moments and conduction electrons. This picture is consistent within both thermodynamic and transport experiments. The relative weight of the coherent fluid can be extracted from the data and can be interpreted as an order parameter, which is zero above the coherence temperature and increases as the temperature is lowered.

  Later on the Knight shift anomaly in nuclear magnetic resonance was also analyzed on the light of the two-fluid picture, and many other heavy fermion materials were explored within this framework [73]. Even more intriguing is the fact that the low temperature value of the fraction of the coherent fluid, f_0, what is called the *hybridization*

effectiveness, can be used as a parameter to predict the low temperature ground state of heavy electron systems and predicts the existence of a localization-delocalization line for the f-electrons as the T^* line discussed above [74].

Even though the two-fluid picture is a phenomenological construction, the fact that so many heavy fermions can be consistently classified in this framework suggests that it is a robust idea and one should expect that a complete microscopic theory should reproduce this phenomenology.

1.5 Perspectives

Given the current status of the field, it is clear that we need to search for new theoretical approaches. Ideally we are looking for an unified framework to identify new critical behavior since so far different kinds of quantum phase transitions have been studied in a case by case basis. Different theories of the quantum critical phenomena start from orthogonal perspectives; while the spin density wave scenario is a momentum space description and treated in weak coupling, the local criticality picture looks at the phenomena in real space and understands it as the breakdown of bound states [75]. In Cap. 5 we revisit the use of supersymmetric spin operators with a generalization to the symplectic-N approach and find promising results towards an united picture of heavy fermions and the presence of new critical modes.

Intrinsic quantum critical systems were recently discovered and are particularly interesting since they suggest that there are stable critical phases in real materials. Intrinsic quantum criticality has been attributed to many different causes: valence fluctuations, quasi-crystallinity, frustration, among others. In stead of looking for the origin the of intrinsic quantum critical behavior individually for each material, the answer might be in the understanding of what these systems have in common. Intrinsic quantum criticality is a phenomena that was not known until recently, and now we have a few examples of this unusual behavior in mixed valent systems, that does not seem to be due to fine-tuning of an ordinary critical point, but a critical point that is robust against external parameters as

pressure, but generally unstable under magnetic field. In Cap. 2 we discuss a phenomenological theory to account for much of the divergent behavior of β-$YbAlB_4$, which might be applicable to other systems as well.

Chapter 2

β-$YbAlB_4$: A Critical Nodal Metal

In this chapter we introduce the concept of *nodal metals* as systems in which the hybridization between the conduction electrons and f-states vanish along some directions in momentum space. These systems can present anomalous dispersion and density of states which reflect in unusual thermodynamic properties. Non-trivial topological character can also be veirfyed. We use the concept of nodal metals to propose a model for the intrinsic quantum criticality of β-$YbAlB_4$, in which a vortex in momentum space gives rise to a new type of Fermi surface singularity. We discuss the implications of this line-node in momentum space for our current understanding of quantum criticality and its interplay with topology. This work is published in *Phys. Rev. Lett. 109, 176404 (2012).*

2.1 Nodal Metals

In the low energy limit, effective theories depend on the structure of the quasiparticle spectrum, which is essentially determined by the symmetries and topological properties of the system. There can be different kinds of spectra and corresponding Fermi surfaces that can or cannot be stable with respect to small perturbations. The stability of a Fermi surface, which separates occupied from empty states in momentum space, can be verified in a similar fashion as the stability of defects in ordered media by the use of *topology* [76, 77].

In Kondo systems, the strong spin-orbit coupling of the f-electrons leads to a non-trivial hybridization matrix with the light conduction electrons. In case the f-electron ground state selected by the crystal electric field is a nodal state (state with zero probability distribution

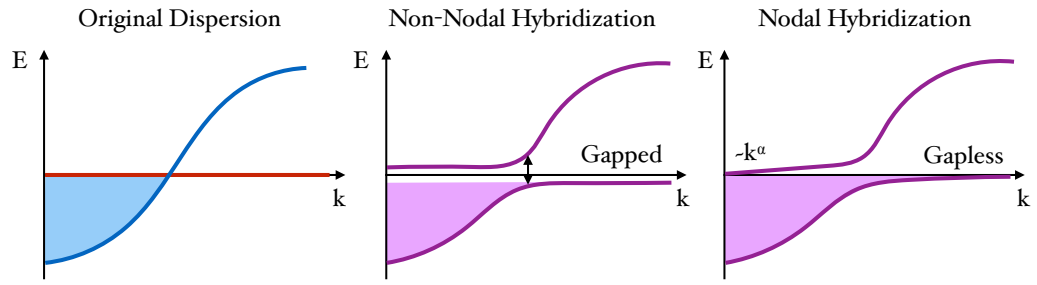

Figure 2.1: Schematic dispersions of: a) the bare conduction electron band in blue and the f-level in red; b) after the onset of an isotropic or non-nodal hybridization; c) after the onset of a nodal hybridization. Here we consider a half-filled band, so the chemical potential lying at zero energy.

along specific directions in space), the hybridization will also carry a node along the respective directions in momentum space and will consequently affect the effective quasiparticle spectrum. The presence of nodes in the spectrum can lead to new universal behavior at low energies, and one can talk about universality classes determined by topological invariants defined from properties of the line or point nodes [76].

Within the realm of Kondo systems, a nodal metal resembles a Kondo Insulator, but one in which the hybridization gap between the conduction and f-electrons vanishes along a line in momentum space. Fig. 2.1 summarizes schematically this idea: in the case of half-filled bands, if the hybridization does not have nodes a full gap opens and the system is a Kondo Insulator; if the hybridization is nodal there is a direct gap but no indirect gap, so the system is effectively gapless, and is called a Kondo semimetal or a *nodal metal*.

There are several known examples of such nodal materials: CeNiSn, CeRhSb and other isostructural compounds [78, 79]. In these systems the hybridization appears to vanish linearly along a line in momentum space, leading to strong anisotropic semimetallic behavior and a V-shaped density of states. In this case the 4f electrons in the Ce atoms have a $J = 5/2$ total angular momentum lower multiplet which is split by the crystal electric field that selects the pure $|5/2, \pm 3/2\rangle$ state as the ground state. This state has a node along the quantization axis, and this is the ultimate cause of the nodal metal behavior. In the following subsection we discuss the role of the spin-orbit coupling and crystal electric fields in the emergence of such nodal states.

2.1.1 Spin-Orbit coupling and Crystal Electric Fields

From the electron rest frame, the motion of the charged nuclei around the electron creates an effective magnetic field which couples to the electronic spin. This effect is stronger the larger the nuclear charge, and is called spin-orbit coupling:

$$H_{SO} = \frac{\hbar^2}{2m^2c^2}\frac{Ze^2}{r^3}\mathbf{S}\cdot\mathbf{L}, \tag{2.1}$$

where m and e are the mass and charge of the electron, c the speed of light, $\hbar$ the Planck's constant divided by 2π, Z the atomic number and $\mathbf{S}$ and $\mathbf{L}$ the spin and angular momentum of the electron, respectively. In case of strong spin-orbit coupling $\mathbf{S}$ and $\mathbf{L}$ are not good quantum numbers and one should think in terms of the total angular momentum $\mathbf{J} = \mathbf{L}+\mathbf{S}$.

From the addition of angular momentum we know that $\mathbf{L}+\mathbf{S}$ gives rise to states with total angular momentum ranging from $|L-S|$ up to $L+S$, and as $S = 1/2$ we actually have two multiplets of total angular momentum states. The lowest multiplet is determined by the third Hund's rule: if the orbital is less than half-filled the lowest multiplet has the lowest value of $J = L - S$, whereas when the orbital is more than half-filled the lowest multiplet has the highest value of total angular momentum $J = L + S$. Once we are interested in the low energy phenomena, in the case of rare-earth atoms, it is possible to consider only the lower total angular momentum multiplet since the spin-orbit interaction is strong (of the order of the bandwidth).

Given the lowest multiplet we now need to analyze the environment in which the rare earth atom is present. The charge distribution of the surrounding atoms breaks the full O(3) rotational symmetry of the atom in free space down to the point group symmetry of the given lattice. Group theory can tell us how the states will split based on the decomposition of the irreducible representations of O(3) in terms of those of the given point group symmetry of the lattice. This can be done by the analysis of the character table of the lattice symmetry group.

Using the example of the Ce-based nodal metals, in these systems the Ce ions are usually in a Ce^{3+} configuration with a single electron in the $4f$ level, with angular momentum $L = 3$.

Following Hund's rules the lowest multiplet has total angular momentum $J = 5/2$ since the shell is less than half-filled. In free space and in presence of time reversal symmetry, the states from a Kramers doublet:

$$|\pm\rangle = a|\pm 1/2\rangle + b|\mp 3/2\rangle + c|\pm 5/2\rangle, \tag{2.2}$$

with $a^2 + b^2 + c^2 = 1$ and the ket states denote $|\pm m_J\rangle$ for $J = 5/2$. For the specific case of CeNiSn and its isostructural compounds, the Ce ions are in a trigonal symmetry environment, very close to the center of hexagons with alternate Ni and Sn atoms. Under this local symmetry one can only form specific combinations of angular momentum states that is in accordance with time-reversal and the rotational symmetry around the 3-fold axis:

$$\begin{aligned} |\Psi_1\rangle &= |\pm 3/2\rangle, \\ |\Psi_2\rangle &= a'|\pm 1/2\rangle + b'|\pm 5/2\rangle, \end{aligned} \tag{2.3}$$

with $a'^2 + b'^2 = 1$. Here we note that $|\Psi_2\rangle$ has a contribution of the $|\pm 1/2\rangle$ state, so $|\Psi_2\rangle$ does not have a line node. Interestingly enough, for CeNiSn the ground state seems to be the pure $|\pm 3/2\rangle$ state, which gives a natural explanation for the strong anisotropy of this system seen in a variety of experiments and the existence of a linear DOS around the Fermi level [78]. The effect of the presence of the nodes in the density of states will be discussed in the following subsections.

Table 2.1 summarizes the possible combinations of states under different lattice symmetries in the presence of time reversal symmetry for the case of $J = 5/2$. It was constructed based on the properties of the respective double groups (see [55] for an introductory discussion), which are an extension of the point groups of interest. This extension is needed in order to guarantee that the character of each conjugacy class is single valued in case we are dealing with half-integer angular momentum. Knowing the character table of the double group related to the lattice symmetry we can deduce what are the irreducible representations.

Table 2.1: Examples of splittings of the total angular momentum states in presence of time reversal and several crystal symmetries for J=5/2.

Symmetry	States	Line Node
Cubic (O')	$c\|\pm 3/2\rangle + d\|\mp 5/2\rangle$	✓
	$\|\pm 1/2\rangle$;$d\|\pm 3/2\rangle - c\|\mp 5/2\rangle$	✗; ✓
Hexagonal (C_6')	$\|\pm 1/2\rangle$	✗
	$\|\pm 3/2\rangle$	✓
	$a\|\pm 5/2\rangle$	✓
Trigonal (C_3')	$\|\pm 3/2\rangle$	✓
	$a\|\pm 1/2\rangle + b\|\pm 5/2\rangle$	✗
	$-b\|\pm 1/2\rangle + a\|\pm 5/2\rangle$	✗
Tetragonal (C_4')	$\|\pm 1/2\rangle$	✗
	$a\|\pm 3/2\rangle + b\|\mp 5/2\rangle$	✓
	$-b\|\pm 3/2\rangle + a\|\mp 5/2\rangle$	✓
Monoclinic (C_2')	$a\|\pm 1/2\rangle + b\|\mp 3/2\rangle + c\|\pm 5/2\rangle$	✗
Triclinic (C_1')	$\|\pm 1/2\rangle$	✗
	$\|\pm 3/2\rangle$	✓
	$\|\pm 5/2\rangle$	✓

Note that group theory can define how the multiplet of states splits and the resulting degeneracy, but it does not tell us which state is the ground state or how large the splitting actually is. To know this information a more thorough analysis of the nature of the neighboring atoms and their positions in the material of interest is needed.

In rare-earth systems the spin-orbit coupling is much larger than the crystal field splitting, and Hund's rules hold. That is not always the case, for example, in d-electron systems the crystal fields are usually stronger than the spin-orbit coupling and the analysis is based only on the orbital angular momentum since in this case it is a good quantum number. For rare-earth systems we have the advantage that the effective theories can be constructed considering only the lower total angular momentum multiplet and sometimes even considering only the lower crystal field state, in case the crystal field splitting is larger than the temperature of the phenomena we are interested in modeling. In case the crystal field splittings are small, crossovers are expected to take place at the temperatures related to the respective crystal field splittings. This point will be important in the analysis of the Electron Spin Resonance of β-$YbAlB_4$ in the next chapter.

In summary, the spin-orbit coupling and the symmetry of the lattice are crucial for the

determination of the possible combinations of m_J states and the presence or absence of line nodes in momentum space.

2.1.2 A note on Topological Kondo Insulators

Differently from the nodal metals discussed above, in case we have any finite contribution of a $|\pm 1/2\rangle$ state we do not have a nodal line but only a nodal point in the hybridization, what usually leads to a spectrum with a direct gap, and to what has been called a *Kondo Insulator* [80].

The fact that we have a full gap can sound as if there is no interesting physics, and that we have a simple insulator. Actually, the strong spin-orbit coupling in the f-electrons leads to a *Topological Kondo Insulator*, as was first analyzed in [81]. Despite the fact that the full gap opens, the hybridization brings in a non-trivial twist to the electronic states, which is robust against perturbations. Interestingly enough, the topological insulators are systems that are insulating in the bulk but have a conducting surface. Surface states are present due to the change in topology as one go from the non-trivial insulator to the vacuum, and are protected by time-reversal symmetry [82].

2.2 The Nodal Hybridization

Here we start with the Anderson impurity model:

$$\mathcal{H} = \sum_{k} \epsilon_{\mathbf{k}\sigma} c^{\dagger}_{\mathbf{k}\sigma} c_{\mathbf{k}\sigma} + \sum_{\alpha} \lambda f^{\dagger}_{\alpha} f_{\alpha} + \sum_{\mathbf{k},\sigma,\alpha} (V_{\mathbf{k}\sigma\alpha} c^{\dagger}_{\mathbf{k}\sigma} f_{\alpha} + V^{*}_{\mathbf{k}\sigma\alpha} f^{\dagger}_{\alpha} c_{\mathbf{k}\sigma}), \tag{2.4}$$

where $c^{\dagger}_{\mathbf{k}\sigma}$ creates one conduction electron with momentum $\mathbf{k}$, spin σ and energy dispersion $\epsilon_{\mathbf{k}\sigma}$, $f^{\dagger}_{\alpha}$ creates localized electron at the impurity site with angular momentum component α at the energy level λ, and $V_{\mathbf{k}\sigma\alpha}$ is the momentum and spin dependent hybridization matrix which mixes f- and conduction electrons.

As discussed in the previous section, there are other energy scales that play an important role in defining the ground state of the f-electrons in rare-earth compounds. In the

presence of strong spin orbit coupling the f-electron states are given in terms of total angular momentum states and we can neglect the higher J multiplet. In the presence of crystal electric fields the lower J multiplet will split in a series of states that should follow the local symmetry around the f-electron sites. In the presence of time reversal symmetry the states in the lower multiplet form Kramers doublets. An f-electron state is then written in terms of a combination of different $|J, m_J\rangle$ states following time reversal and the symmetries of the system of interest, with the weight of each state being determined by the energy minimization of the crystal field Hamiltonian.

Given the lower f-electron state, the hybridization matrix can be written as the overlap of the c- and f-electron states within the lattice potential. Considering the c-electrons as plane waves:

$$|\mathbf{k}\sigma\rangle = \frac{e^{i\mathbf{k}\cdot\mathbf{r}}}{\sqrt{\mathcal{V}}}\chi_\sigma = \frac{4\pi}{\sqrt{\mathcal{V}}}\sum_l i^l j_l(kr)\sum_{m=-l}^{l} Y_l^{m*}(\theta_\mathbf{k},\phi_\mathbf{k})Y_l^m(\theta_\mathbf{r},\phi_\mathbf{r})\chi_\sigma, \tag{2.5}$$

where $\mathcal{V}$ is the volume of the system, $j_l(x)$ are spherical Bessel functions of order l, $Y_l^m(\theta_\mathbf{x},\phi_\mathbf{x})$ spherical harmonics and χ_σ the spin state. The atomic f-electron state at site i with angular momentum component α can be written as:

$$|if\alpha\rangle = R_{nl}(|\mathbf{r}-\mathbf{R}_i|)\sum_{m\sigma} C^{J\alpha}_{lms\sigma}Y_l^m(\theta_{\mathbf{r}-\mathbf{R}_i},\phi_{\mathbf{r}-\mathbf{R}_i})\chi_\sigma, \tag{2.6}$$

where $R_{nl}(x)$ is the radial solution of the atomic Schrödinger equation with principal quantum number n and orbital quantum number l, and $C^{J\alpha}_{lms\sigma} = \langle J\alpha|lm,s\sigma\rangle$ are Clebsh-Gordan coefficients. The overlap of these states under the lattice potential $V(\mathbf{r})$ gives the hybridization matrix:

$$\begin{aligned} V_{\mathbf{k}\sigma\alpha} &= \langle\mathbf{k}\sigma|V(\mathbf{r})|if\alpha\rangle \\ &= \frac{4\pi}{\sqrt{\mathcal{V}}}\sum_l \int r^2 dr(-i)^{l'} j_{l'}(kr)V(\mathbf{r})R_{nl}(|\mathbf{r}-\mathbf{R}_i|)\times \\ &\times \sum_{mm'\sigma}\int d\Omega Y_{l'}^{m'*}(\theta_r,\phi_r)Y_l^m(\theta_{\mathbf{r}-\mathbf{R}_i},\phi_{\mathbf{r}-\mathbf{R}_i})C^{J\alpha}_{lms\sigma}Y_{l'}^{m'}(\theta_\mathbf{k},\phi_\mathbf{k})\chi^*_\sigma\chi_{\sigma'} \\ &= V_0\sum_m C^{J\alpha}_{l'ms\sigma'}Y_{l'}^m(\theta_\mathbf{k},\phi_\mathbf{k}), \end{aligned} \tag{2.7}$$

where we used the orthogonality condition for the spherical harmonics and spin states. The quantity V_0 comes from the radial part of the integral and is equal to a constant. Note that in $V_{\mathbf{k}\sigma\alpha}$ the σ index is determined by the spin state of the conduction electron and the α index by the projection of the total angular momentum of the f-electron. For f-electrons $l' = 3$ and $J = \{7/2, 5/2\}$, depending if the shell is more or less than half-filled, respectively.

The most general form for the hybridization matrix considers the possibility of the f-electron ground states to be a superposition of $|J\alpha\rangle$ states labelled by M [83]:

$$|ifM\rangle = \sum_{\alpha} b_{\alpha}^{M} |if\alpha\rangle, \tag{2.8}$$

in which case,

$$V_{\mathbf{k}\sigma M} = V_0 \sum_{\alpha} b_{\alpha}^{M} \sum_{m\sigma} C_{lms\sigma}^{J\alpha} Y_l^m(\hat{\mathbf{k}}), \tag{2.9}$$

where b_{α}^{M} is the weight of each pure α state in the mixed state labelled by M and determined by the analysis of the crystal electric field.

From the form of the hybridization above it is possible to verify that for $l > 0$ the spherical harmonics carry nodes in particular directions in momentum space. The presence of line nodes in the hybridization matrices are known for a long time [83, 84], but attention to their importance was given only recently [78, 85].

2.2.1 Hybridization in the lattice model

If we are interested in modeling heavy fermions we should start with the Anderson lattice model, which is a generalization of the impurity model discussed above with one f-electron in every site i of the lattice. Now the conduction plane waves hybridize with the Bloch states of f-electrons, determined by the Fourier transform:

$$f_{\mathbf{k}\alpha} = \frac{1}{\sqrt{\mathcal{N}}} \sum_{i} e^{i\mathbf{k}\cdot\mathbf{R}_i} f_{i\alpha}, \tag{2.10}$$

where $\mathcal{N}$ is the number of sites, so we can write:

$$\begin{aligned}\mathcal{H} &= \sum_{k} \epsilon_{\mathbf{k}\sigma} c^{\dagger}_{\mathbf{k}\sigma} c_{\mathbf{k}\sigma} + \sum_{i\alpha} \lambda f^{\dagger}_{i\alpha} f_{i\alpha} \\ &+ \frac{1}{\sqrt{\mathcal{N}}} \sum_{i,\mathbf{k},\sigma,\alpha} (V_{\mathbf{k}\sigma\alpha} e^{i\mathbf{k}\cdot\mathbf{R}_i} c^{\dagger}_{\mathbf{k}\sigma} f_{i\alpha} + V^{*}_{\mathbf{k}\sigma\alpha} e^{-i\mathbf{k}\cdot\mathbf{R}_i} f^{\dagger}_{i\alpha} c_{\mathbf{k}\sigma}).\end{aligned} \tag{2.11}$$

There is actually more than one way to look into this problem. One can start with the conduction plane-wave estate and find the overlap with the atomic f-states in every site in the lattice, or one can write the conduction electron states as Wannier states with the symmetry of the local f-state by means of a form factor with an angular dependence as in the hybridization matrix above. The discussion boils down to choosing where we want to absorb the form factor coming from the spherical harmonics. In cases in which the hybridization is not on-site, the second choice is usually more convenient, so one can also write:

$$\mathcal{H} = \sum_{k} \epsilon_{\mathbf{k}\alpha} c^{\dagger}_{\mathbf{k}\alpha} c_{\mathbf{k}\alpha} + \sum_{i\alpha} \lambda f^{\dagger}_{i\alpha} f_{i\alpha} + \sum_{i,\alpha} (V c^{\dagger}_{i\alpha} f_{i\alpha} + V^{*} f^{\dagger}_{i\alpha} c_{i\alpha}), \tag{2.12}$$

where V now is a number which characterizes the magnitude of the hybridization and

$$c_{i\alpha} = \sum_{\mathbf{k}\sigma} \mathcal{Y}_{\alpha\sigma}(\mathbf{k}) e^{-i\mathbf{k}\cdot\mathbf{R}_i} c_{\mathbf{k}\sigma}, \tag{2.13}$$

is the Wannier state of the conduction electrons at site i with the symmetry of the f-state, with the form factor

$$\mathcal{Y}_{\alpha\sigma}(\mathbf{k}) = \sum_{m} C^{J\alpha}_{lms\sigma} Y^{m}_{l}(\mathbf{k}), \tag{2.14}$$

where

$$Y^{m}_{l}(\mathbf{k}) = \frac{1}{Z} \sum_{NN} Y^{m}_{l}(\mathbf{R}) e^{i\mathbf{k}\cdot\mathbf{R}}, \tag{2.15}$$

is the minimal generalization of the Fourier transform which captures the symmetry of the lattice, with the sum over the nearest neighbors (NN).

2.2.2 Effects in the electronic spectrum and density of states

Going back to the original notation in which the non-trivial form factor is absorbed in the hybridization matrix, we can write the matrix explicitly as:

$$V_{\mathbf{k}\sigma\alpha} = V_0 \begin{pmatrix} v_1 & v_2 \\ (-1)^{\Delta+1} v_2^* & (-1)^{\Delta} v_1^* \end{pmatrix} \tag{2.16}$$

where

$$v_1 = C^{J\alpha}_{l,(\alpha-1/2),1/2,1/2} Y_3^{\alpha-1/2}(\mathbf{k}), \tag{2.17}$$

$$v_2 = C^{J(-\alpha)}_{l,(-\alpha-1/2),1/2,1/2} Y_3^{-\alpha-1/2}(\mathbf{k}), \tag{2.18}$$

$$\Delta = l + s - J + \alpha - 1/2 = \begin{cases} \alpha + 1/2 & \text{for Ce} \\ \alpha - 1/2 & \text{for Yb} \end{cases} \tag{2.19}$$

The electronic spectrum is computed by the diagonalization of the following Hamiltonian:

$$\hat{H} = \begin{pmatrix} \hat{\epsilon}_{\mathbf{k}} & \hat{V}_{\mathbf{k}} \\ \hat{V}^*_{\mathbf{k}} & \hat{\epsilon}_f \end{pmatrix}, \tag{2.20}$$

where

$$\hat{\epsilon}_{\mathbf{k}} = \begin{pmatrix} \epsilon_{\mathbf{k}\uparrow} & 0 \\ 0 & \epsilon_{\mathbf{k}\downarrow} \end{pmatrix}, \qquad \hat{\epsilon}_f = \begin{pmatrix} \epsilon_{f\alpha} & 0 \\ 0 & \epsilon_{f-\alpha} \end{pmatrix}, \tag{2.21}$$

where α is the projection of the total angular momentum and $\epsilon_{\mathbf{k}\sigma} = \epsilon_{\mathbf{k}} + \tilde{\sigma} g_c \mu_B B$, $\epsilon_{f\alpha} = \epsilon_f + \tilde{\alpha} g_f \mu_B B$, where $\tilde{\sigma}, \tilde{\alpha} = sign(\sigma, \alpha)$.

In the absence of magnetic fields we have two doubly degenerate states with dispersion:

$$E = \frac{\epsilon_{\mathbf{k}} + \epsilon_f}{2} \pm \sqrt{\left(\frac{\epsilon_{\mathbf{k}} - \epsilon_f}{2}\right)^2 + V_0^2(|v_1|^2 + |v_2|^2)}. \tag{2.22}$$

In general a gap will open when the hybridization develops. In the case of a nodal hybridization, the hybridization matrix will vanish in some directions in momentum space and there is no indirect gap.

Systems with flat f-electron bands and nodal hybridization can be modeled by effective models that consider only the low energy behavior. These systems have Fermi lines instead of Fermi surfaces and generally have a non-linearizable dispersion around the Fermi surface dictated by the form of the hybridization matrix. The hybridization matrix elements close to the z-axis (the Fermi line) behave as:

$$v_1 \sim Y_3^{\alpha-1/2}(\mathbf{k}) \sim P_3^{\alpha-1/2}(\cos\theta_{\mathbf{k}}) \sim (\sin\theta_{\mathbf{k}})^{\alpha-1/2}, \tag{2.23}$$

$$v_2 \sim Y_3^{-\alpha-1/2}(\mathbf{k}) \sim P_3^{-\alpha-1/2}(\cos\theta_{\mathbf{k}}) \sim (\sin\theta_{\mathbf{k}})^{\alpha+1/2}. \tag{2.24}$$

Note that all the hybridization matrices for $m_J > 1/2$ vanish along the z-axis (they are all proportional to some power of $\sin\theta_{\mathbf{k}}$) and that the diagonal terms dominate the behavior as $\theta \to 0$. Now, taking $\epsilon_f = 0$ and $W \gg V$, the dispersion emerging from the z-axis goes as:

$$E = \begin{cases} V_{\mathbf{k}}^2/W \sim v_1^2/W \sim k_p^{2\alpha-1} & \text{upper band} \\ -W - V_{\mathbf{k}}^2/W \sim -W & \text{lower band} \end{cases} \tag{2.25}$$

what leads to a possibly unusual dispersion along the direction perpendicular to the z-axis, with momentum dependence going as $k_p^{2\alpha-1}$.

Under the condition above, the density of states will have a contribution proportional to:

$$\rho \sim E^{\frac{d-2\alpha}{2\alpha-1}}, \tag{2.26}$$

which can be anomalous or even singular for several combinations of dimensionality and α. In particular, for d=3 and a $|\pm 5/2\rangle$ state we find $\rho \sim E^{-1/2}$.

The form factor and consequently the dispersion are universally determined in the small momentum limit by the dominant total angular momentum component of the f-electrons (the component with smaller α). At larger momenta the dispersion depends on the microscopic details of the lattice.

2.2.3 Topological Features

Systems with topologically protected Fermi points or lines belong to the broad class of topological matter. Distinctly from topological insulators and superconductors which belong to the fully gapped topological matter, these are gapless topological matter. However, they have features which were earlier ascribed only to topological insulators with protected gapless states on the surface or inside vortex cores [76].

In case of point defects, one can write a Chern number, as proposed in [81] for a Kondo insulator, to classify different non-trivial topological states. From the hybridization matrix above we can define the vector $\mathbf{n}$ by the normalization of the vector $\mathbf{m}$ in $V_{\mathbf{k}} = \boldsymbol{\sigma} \cdot \mathbf{m}$ and write the Chern number as the following surface integral over the Brillouin zone:

$$C = \frac{1}{8\pi} \int_{S^2} d\mathbf{S} \cdot \epsilon_{\mathbf{ijk}} \mathbf{n_i} (\nabla_{\mathbf{k}} \mathbf{n_j} \times \nabla_{\mathbf{k}} \mathbf{n_k}). \tag{2.27}$$

Evaluating the Chern number for different f-states, one finds $C = 1$ only for Ce in the $|5/2, \pm 1/2\rangle$ state; all the other nodal cases give zero Chern number, including the Yb $|7/2, \pm 1/2\rangle$ state. Apparently one needs to define the vector $\mathbf{m}$ from $\hat{V}_{\mathbf{k}} = (\sigma\sigma_3) \cdot \mathbf{m}$ for the Yb case in order to find $C = 1$ for the Yb $|\pm 1/2\rangle$ state.

A vanishing hybridization amplitude along some directions in momentum space, within the assumption that the f-level is pinned to the chemical potential, brings in an emergent Fermi line in three dimensions. This special kind of Fermi surface is protected the integer number of electrons per unit cell and by the crystal electric field of the environment surrounding the rare-earth atoms.

Here we note that the Chern number above is not able to capture the non-trivial topology of the line nodes due to the different nature of the topological defect, or Fermi surface, in the case of a nodal hybridization. Now one needs to define an invariant in a different homotopy class [76]. For a point node in the case of $|\pm 1/2\rangle$, wrapping a surface around the defect seems the natural thing to do in order to quantify and classify the defect. In case of a line node one needs to compute a line integral around the defect, as shown in Fig. 2.2.

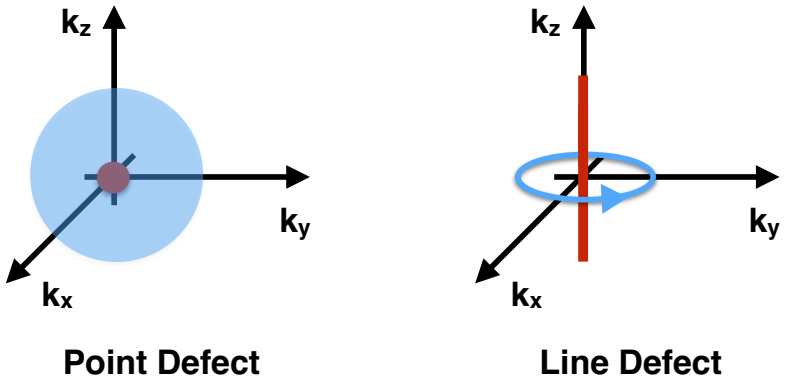

Figure 2.2: Defects in momentum space. Left: Surface covering a point defect. Right: A contour wrapping around a line defect.

We can now define a winding number from the hybridization matrix:

$$W = \frac{1}{2\pi i} \oint_C dl \frac{Tr[V^\dagger_{\mathbf{k}\sigma\alpha} \sigma_3 \partial_\phi V_{\mathbf{k}\sigma\alpha}]}{Tr[V^\dagger_{\mathbf{k}\sigma\alpha} V_{\mathbf{k}\sigma\alpha}]}, \tag{2.28}$$

which gives, for the case of the nodal metal described above,

$$W = \alpha - 1/2, \tag{2.29}$$

computed asymptotically close to the nodal axis.

2.3 Theory for the critical behavior of β-YbAlB$_4$

In the light of the discussion above, we start building the theory for β-YbAlB$_4$ by looking at the main ingredient that gives rise to the non-trivial behavior in this material: the Yb atoms which carry f-electrons. We shall assume that the Yb ions are in a nominal Yb^{3+}, $4f^{13}$ configuration, with total angular momentum $J = 7/2$, according to Hund's rules. Photoemission spectroscopy indicates a microscopic valence of 2.75 due to moment-conserving valence fluctuations $Yb^{3+} \leftrightarrow Yb^{2+} + e^-$ [86].

2.3.1 β-$YbAlB_4$ structure

β-$YbAlB_4$ has a peculiar crystal structure in which the Yb atoms form a squeezed honeycomb lattice, sandwiched between layers of B atoms, with the Yb atoms sitting between pairs of 7-member B rings, giving rise to a local environment with local seven-fold symmetry [60], as shown in Fig. 2.3.

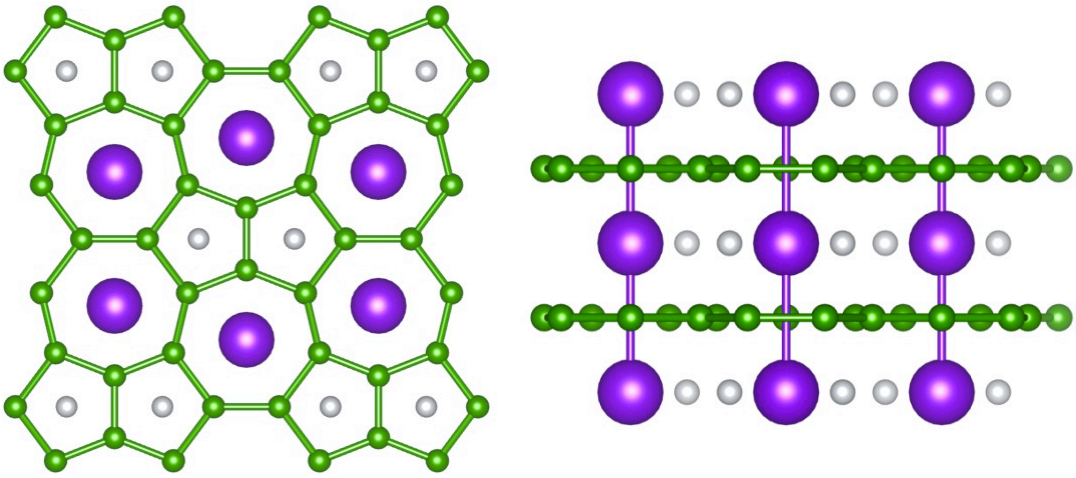

Figure 2.3: Left: Top view; Right: Side view of the β-$YbAlB_4$ crystal structure. The large purple spheres are Yb atoms, the small connected green spheres are B and the small gray disconnected spheres are Al. Note the seven-fold symmetric environment around the Yb atoms: there are 7-fold B rings above and below them. Figure generated by the VESTA software [10].

The $J = 7/2$ crystal field operators with 7-fold and time-reversal symmetries conserve J_z, splitting the $J = 7/2$ Yb multiplet into four Kramers doublets, each with definite $|m_J|$. The Curie constant and the Ising anisotropy of the magnetic susceptibility of β-$YbAlB_4$ are consistent with a pure Yb ground-state doublet $|J = 7/2, m_J = \pm 5/2\rangle$ [87]. This can be understood heuristically since this is the configuration that exhibits maximal overlapp with the electrons in the seven-fold boron rings and consequently lowers the total energy. This Ising ground-state is also consistent with the large anisotropic g-factor observed in electron spin resonance measurements on β-$YbAlB_4$ [88], as will be discussed in the next chapter.

2.3.2 Model and mean field treatment

We model the low energy physics of β-$YbAlB_4$ as a layered Anderson lattice [87],

$$H = \sum_{n,k,\sigma} \epsilon_{\mathbf{k}n} c^{\dagger}_{\mathbf{k}n\sigma} c_{\mathbf{k}n\sigma} + \sum_{j} H_m(j), \tag{2.30}$$

where the first term describes tight-binding boron conduction electron bands; $c^{\dagger}_{\mathbf{k}n\sigma}$ creates a conduction electron with momentum $\mathbf{k}$, spin component σ in the band n; and

$$H_m(j) = V_0(c^{\dagger}_{j\alpha} X_{0\alpha}(j) + \text{h.c.}) + E_f X_{\alpha\alpha}(j), \tag{2.31}$$

describes the hybridization of the conduction electrons with the f-electrons at the Yb ion at site j and E_f is the energy level of the f-electrons. The operator

$$c^{\dagger}_{j\alpha} = \sum_{p\in(1,14),\sigma} c^{\dagger}_{\sigma}(\mathbf{R}_{jp})\ \mathcal{Y}_{\sigma\alpha}(\mathbf{r}_p), \tag{2.32}$$

creates a conduction electron in a Wannier state delocalized across the seven-fold boron rings directly above and below the Yb ion at site j, with local f symmetry and $\alpha = \pm 5/2$. The $\mathbf{R_{jp}} = \mathbf{R_j} + \mathbf{r_p}$ are the locations of the fourteen boron sites ($p = 1, ..., 14$) around the upper and lower rings surrounding the given Yb site j (see Fig. 2.3). The form factor matrix is written as:

$$\mathcal{Y}_{\sigma\alpha}(\mathbf{r}) = C^{\frac{7}{2}}_{\sigma\alpha} Y^3_{\alpha-\sigma}(\mathbf{r}) = \frac{1}{\sqrt{7}} \begin{pmatrix} \sqrt{6}Y^3_2 & Y^3_3 \\ Y^3_{-3} & \sqrt{6}Y^3_{-2} \end{pmatrix} (\hat{\mathbf{r}}), \tag{2.33}$$

where the $C^{\frac{7}{2}}_{\sigma\alpha} = \langle 3\alpha - \sigma, \frac{\sigma}{2} | \frac{7}{2}, \alpha \rangle$ are Clebsch-Gordan coefficients for the Yb^{3+}, $\alpha = \pm 5/2$ configurations, allowing the change of basis from spin to total angular momentum for the conduction electrons.

Here $X_{\alpha\beta}$ are Hubbard operators, which are written in terms of the $|4f^{13}, m_J \equiv \alpha = \pm 5/2\rangle$ "hole" states of the Yb^{3+} ion with total angular momentum component equal to α and the completely filled shell (or empty state in the language of holes) Yb^{2+} state $|4f^{14}\rangle$,

omitting the site index, as:

$$X_{\alpha\alpha} = |4f^{13},\alpha\rangle\langle 4f^{13},\alpha|, \tag{2.34}$$

$$X_{0\alpha} = |4f^{14}\rangle\langle 4f^{13},\alpha|, \tag{2.35}$$

$$X_{\alpha 0} = |4f^{13},\alpha\rangle\langle 4f^{14}|, \tag{2.36}$$

$$X_{00} = |4f^{14}\rangle\langle 4f^{14}|. \tag{2.37}$$

Here we note that these operators do not follow canonical commutation relations but:

$$[\chi_{\alpha\beta}(i),\chi_{\gamma\delta}(j)]_{\pm} = \delta_{ij}(\delta_{\beta\gamma}\chi_{\alpha\delta} \pm \delta_{\alpha\delta}\chi_{\gamma\beta}), \tag{2.38}$$

where we have anti-commutation relations (+) between the "fermionic" Hubbard operators ($\chi_{0\gamma}$ and $\chi_{\gamma 0}$) and commutation relations (−) between the "bosonic" Hubbard operators (χ_{00} and $\chi_{\gamma\gamma'}$) and between fermionic and bosonic operators as well.

Given the non-canonical commutation relations for the Hubbard operators, we cannot simply apply approaches as diagrammatic expansion since Wick's theorem does not hold [35]. In order to proceed with such kind of formalism we employ a slave boson decomposition of the Hubbard operators [89, 39], which can be written at each site as:

$$X_{\alpha\alpha}(j) = f^{\dagger}_{j\alpha}f_{j\alpha}, \tag{2.39}$$

$$X_{0\alpha}(j) = b^{\dagger}_{j}f_{j\alpha}, \tag{2.40}$$

$$X_{\gamma 0}(j) = f^{\dagger}_{j\alpha}b_{j}, \tag{2.41}$$

$$X_{00}(j) = b^{\dagger}_{j}b_{j}, \tag{2.42}$$

where b_j and $f_{j\gamma}$ are a slave boson and Abrikosov pseudo-fermion, following the canonical bosonic and fermionic commutation relations, respectively. Here the charge degree of freedom is assigned to the bosons, while the spin degree of freedom is assigned to the fermions. This assignment can be understood in the following way: the filled shell (or empty state), is represented by a bosonic state, while the states with one or two holes (or electrons) are

represented by fermionic states. Now the number operator at each site is written as:

$$\sum_{\alpha} X_{\alpha\alpha}(j) + X_{00}(j) = \sum_{\alpha} f^{\dagger}_{j\alpha} f_{j\alpha} + b^{\dagger}_{j} b_{j} = 1, \tag{2.43}$$

which guarantees that the sites are never doubly occupied. The sites can be "empty" (with the full filled shell) when $n_B = 1$, or singly occupied (by a hole) when $n_F = 1$. This condition is implemented within a path integral formalism as a constraint in the theory. Here we note the convenience of the slave-particle approach in which case we have a holonomic constraint in stead of the non-holonomic constraint $n_F < 2$ in case we do not introduce the slave particle.

Within a mean-field approximation we can rewrite the Hamiltonian as

$$H_m(j) = V_0^* [c^{\dagger}_{j\alpha} f_{j\alpha} + \text{h.c.}] + \tilde{E}_f f^{\dagger}_{j\alpha} f_{j\alpha} + \lambda_0 (r^2 - 1), \tag{2.44}$$

where $V_0^* = V_0 r$ is the quasiparticle hybridization, renormalized by the mean-field amplitude of the slave boson field, $r = |\langle b \rangle|$, taken to be uniform. The parameter λ_0 imposes the mean-field constraint $\langle n_f \rangle + r^2 = 1$ as a Lagrange multiplier, excluding double occupancy due to the strong Coulomb interaction, what was already encoded in the original form of the Hubbard operators. Here we defined the renormalized position of the f-level as $\tilde{E}_f = \lambda_0 + E_f$.

Next, we transform the Hamiltonian from real space into momentum space and evaluate the form-factor of the seven-fold symmetric Yb-B cluster. To obtain a simplified model, let us assume a single band of dispersion $\epsilon_{\mathbf{k}}$ hybridizing with the Yb ion. Rewriting the creation operator at a given boron site in terms of plane wave states

$$c^{\dagger}_{\sigma}(\mathbf{R}_{jp}) = (4\mathcal{N})^{-1/2} \sum_{\mathbf{k}} c^{\dagger}_{\mathbf{k}\sigma} e^{-i\mathbf{k}\cdot\mathbf{R}_{jp}}, \tag{2.45}$$

and similarly for the f-operators:

$$f_{j\alpha} = \mathcal{N}^{-1/2} \sum_{\mathbf{k}} f_{\mathbf{k}\alpha} e^{i\mathbf{k}\cdot\mathbf{R}_j}, \tag{2.46}$$

where $\mathcal{N}$ is the number of Yb sites, Eq. (2.32) becomes:

$$c^{\dagger}_{j\alpha} = (4\mathcal{N})^{-1/2} \sum_{\mathbf{k}\sigma} c^{\dagger}_{\mathbf{k}\sigma} \gamma_{\sigma\alpha}(\mathbf{k}) e^{-i\mathbf{k}\cdot\mathbf{R}_j}, \tag{2.47}$$

where the form-factor of the Yb-B cluster can be written as

$$\gamma_{\sigma\alpha}(\mathbf{k}) = \sum_{p=1,14} \mathcal{Y}_{\sigma\alpha}(\mathbf{r}_p) e^{-i\mathbf{k}\cdot\mathbf{r}_p}. \tag{2.48}$$

The mean-field Hamiltonian in Eq. 2.44 can then be written in terms of the plane-wave $c_{\mathbf{k}\sigma}$ and $f_{\mathbf{k}\alpha}$ operators as

$$H_{eff} = \sum_{\mathbf{k}} (c^{\dagger}_{\mathbf{k}}, f^{\dagger}_{\mathbf{k}}) \begin{pmatrix} \epsilon_{\mathbf{k}}\mathbb{I} & \underline{V}(\mathbf{k}) \\ \underline{V}^{\dagger}(\mathbf{k}) & \tilde{E}_f\mathbb{I} \end{pmatrix} \begin{pmatrix} c_{\mathbf{k}} \\ f_{\mathbf{k}} \end{pmatrix}, \tag{2.49}$$

where all details of the hybridization are hidden in the matrix $[\underline{V}(\mathbf{k})] = \frac{1}{2} V_0^* \underline{\gamma}(\mathbf{k})$.

We can now look into the form factor in more detail. In polar co-ordinates

$$\mathcal{Y}(\hat{\mathbf{r}}) = \sqrt{\frac{5}{64\pi}} s_\theta^2 \begin{pmatrix} 6c_\theta e^{2i\phi} & -s_\theta e^{3i\phi} \\ s_\theta e^{-3i\phi} & 6c_\theta e^{-2i\phi} \end{pmatrix}, \tag{2.50}$$

where we denote $(\cos\theta, \sin\theta) \equiv (c_\theta, s_\theta)$. The important point here is that the hybridization vanishes as $\sin^2\theta$ along the c-axis. To obtain an analytic expression, we approximate the discrete sum over the positions in the seven-fold B ring by a continuous integral: $\sum_p \to 7 \sum_{\pm} \int \frac{d\phi}{2\pi}$. We find that $V(\mathbf{k})$ is proportional to a unitary matrix,

$$V(\mathbf{k}) = i\tilde{V}_0 \begin{pmatrix} v_{1\mathbf{k}} & v_{2\mathbf{k}} \\ -v^*_{2\mathbf{k}} & v^*_{1\mathbf{k}} \end{pmatrix}, \tag{2.51}$$

where $\tilde{V}_0 = \frac{7V_0^*}{16}\sqrt{\frac{5}{\pi}}$ and

$$\begin{aligned} v_{1\mathbf{k}} &= 6\sin(k_z a/2)(\hat{k}_x + i\hat{k}_y)^2 J_2(k_\perp R) \\ v_{2\mathbf{k}} &= \cos(k_z a/2)(\hat{k}_x + i\hat{k}_y)^3 J_3(k_\perp R), \end{aligned} \tag{2.52}$$

where J_n are Bessel functions of order n, R is the radius of the seven-fold rings and a is the distance between boron layers. Since $J_n(x) \propto x^n$ for small x, near the c-axis, the diagonal terms are the dominant ones and the hybridization vanishes as $k_\perp^2$:

$$V(\mathbf{k}) \sim \begin{pmatrix} (k_x + ik_y)^2 & 0 \\ 0 & (k_x - ik_y)^2 \end{pmatrix}. \tag{2.53}$$

As one proceeds around the c-axis, the phase of the hybridization advances by 4π, forming a double vortex in the hybridization along the c-axis. Computing the winding number introduced in the previous section:

$$W = \frac{1}{2\pi i} \oint_C dl \frac{Tr[V^\dagger_{\mathbf{k}\sigma\alpha} \sigma_3 \partial_\phi V_{\mathbf{k}\sigma\alpha}]}{Tr[V^\dagger_{\mathbf{k}\sigma\alpha} V_{\mathbf{k}\sigma\alpha}]}, \tag{2.54}$$

we find $W = \alpha - 1/2 = 2$. This *vorticity* associated with the line defect is a consequence of angular momentum conservation about the c-axis: plane waves $|\mathbf{k}\sigma\rangle$ traveling along the c-axis carry a spin angular momentum of $\pm 1/2$ along the c-axis, and because the f-states are in an $|\pm 5/2\rangle$ state, angular momentum conservation prevents the mixing of conduction electrons traveling along the c-axis and f-electrons.

We can now diagonalize the mean-field Hamiltonian, to obtain the hybridized dispersion

$$E^\pm_{\mathbf{k}} = \frac{\epsilon_{\mathbf{k}} + \tilde{E}_f}{2} \pm \sqrt{\left(\frac{\epsilon_{\mathbf{k}} - \tilde{E}_f}{2}\right)^2 + |V(k)|^2}, \tag{2.55}$$

where $|V(k)|^2 = \tilde{V}_0^2[|v_{1\mathbf{k}}|^2 + |v_{2\mathbf{k}}|^2]$. Fig. 2.4 illustrates the hybridized band-structure. Near the c-axis, the squared hybridization vanishes as $V(\mathbf{k})^2 = A(k_z)k_\perp^4$. The dispersion in the vicinity of the c-axis is then given by

$$E(k_\perp, k_z) = \tilde{E_f} + \frac{|V(\mathbf{k})|^2}{-\epsilon(k_z)} \approx \tilde{E}_f + \eta(k_z)k_\perp^4, \tag{2.56}$$

where $\eta(k_z) = \frac{A(k_z)}{-\epsilon(k_z)}$ and we have assumed that $|\epsilon(k_z)|$ is large compared to $|V(k)|$. In other words, the system develops an emergent two-dimensional Fermi surface, with a $k_\perp^4$ dispersion. A hole band is formed in the region where $\epsilon(k_z) > 0$, while an electron band is

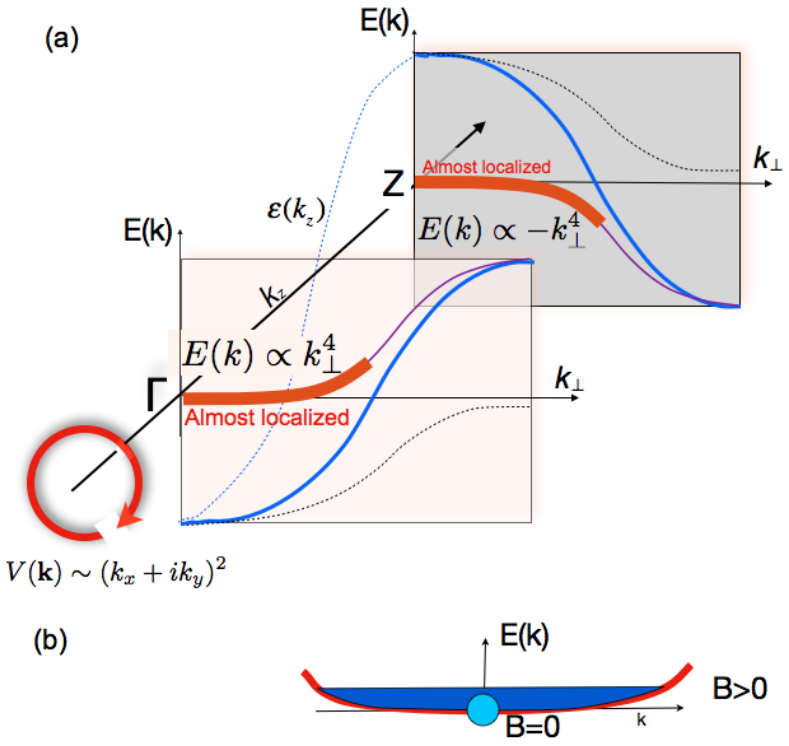

Figure 2.4: (a) Showing dispersion around the c-axis, with an electron pocket at the Γ point and a hole pocket at the Z point. (b) Magnetic field fills the $k_\perp^4$ flat band.

formed in the region where $\epsilon(k_z) < 0$. In the case where $\epsilon(k_z)$ changes sign along the c-axis, a two dimensional electron and hole band is formed above and below the f-level.

To explain the intrinsic criticality of β-$YbAlB_4$ we conjecture that the f-level is pinned to zero energy $\tilde{E}_f = 0$. A heuristic argument for this assumption, is to regard β-$YbAlB_4$ as a Kondo insulator in which the nodal hybridization closes the gap along the c-axis, pinching the f-level in the gap at precisely zero energy. At the current stage of understanding, this assumption is purely phenomenological, a point we return to later. If $\tilde{E}_f = 0$, the density of states for this dispersing system is then given by

$$N^*(E) = \sum_{\pm} N^*_{\pm}(E)\theta(\pm E), \tag{2.57}$$

where for each branch:

$$\begin{aligned} N^*_{\pm}(E) &= 2\int k_{\perp}\frac{dk_{\perp}}{dE_{\pm}}\frac{dk_z}{(2\pi)^2}, \\ &= \frac{1}{\sqrt{|E|T_0^{\pm}}}, \end{aligned} \tag{2.58}$$

and

$$\frac{1}{\sqrt{T_0^{\pm}}} = \frac{1}{8\pi^2}\int \frac{dk_z}{\sqrt{|\eta(k_z)|}}\theta[\mp\epsilon(k_z)] \tag{2.59}$$

determines the characteristic scales $T_0^{\pm}$ for the electron (+) and hole (−) branch of the dispersion. Powerlaw scaling will extend out to characteristic Kondo temperature T_K of the system, so that the total weight x of f-electrons contained within the divergent peak is

$$2x = \int_{-T_K}^{T_K} N^*(E) \approx 4\sqrt{T_K/T_0}, \tag{2.60}$$

giving $T_0 = 4T_K/x^2$.

If the f-level is pinned to zero energy, then at low temperatures a Fermi line of zero energy excitations forms along the c-axis. In a field, the Zeeman-splitting of the f-level induces a singular polarization of nodal electron and hole bands, broadening the Fermi line into a distinct tubular Fermi surface. When a field is introduced, a spin-polarized Fermi surface grows around the line-zero in the hybridization, giving rise to a density of states of order $N^*[\frac{g}{2}\mu_B B] \sim B^{-1/2}$, leading to a Pauli susceptibility that diverges as $\chi \sim B^{-1/2}$. We call this field-induced Fermi surface transition a *vortex transition*, see Fig. 2.5. Vortex transitions are reminiscent of a Lifshitz transition, but whereas Lifshitz transitions involve point defects in momentum space [81, 90], the vortex transition involves a line defect.

The non Fermi liquid physics of $YbRh_2Si_2$ was also associated with a Lifshitz transitions driven by Zeeman splitting [90], with a model based on the presence of shallow bands close to the Fermi level and consequently a large density of states. In this case a magnetic field of the order of the shallow band width Zeeman splits the bands causing a Lifshitz transition and anomalies in both the thermodynamics and transport properties.

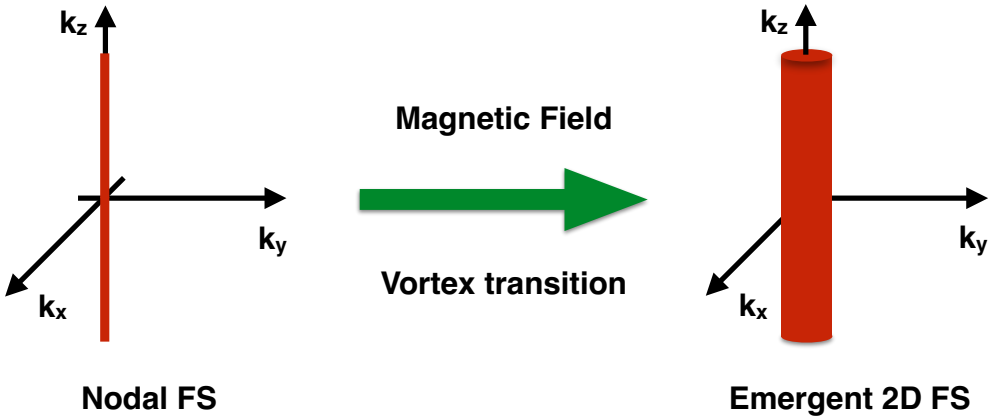

Figure 2.5: Schematic picture of the vortex transition. Under magnetic field the nodal Fermi surface evolves towards an emergent 2D Fermi surface as a new kind of Lifshitz transition.

2.3.3 T/B Scaling

We can model the singular thermodynamics of the system writing the Free energy

$$F[B,T] = -T \sum_{\alpha=\pm 5/2} \int_{-\infty}^{\infty} dE N(E) \ln[1 + e^{-\beta(E - g\mu_B B\alpha)}] \tag{2.61}$$

using the explicit form for the density of states from Eq. 2.58. Writing the free energy as a function of T/B:

$$F[B,T] = T^{3/2}\Phi\left(\frac{g\mu_B B}{T}\right) \tag{2.62}$$

where

$$\Phi(y) = -\frac{1}{\sqrt{T_0}} \int_0^{\infty} \frac{dx}{\sqrt{|x|}} \sum_{\alpha=\pm 5/2} \ln[1 + e^{-x - y\alpha}], \tag{2.63}$$

and $T_0^{-1/2} = (1/2)\sum_{\pm}(T_0^{\pm})^{-1/2}$. Fig. 2.6 compares the experimental scaling curve [61] with that predicted by our simple model. While a qualitatively good fit to the observations is obtained using a gyromagnetic ratio consistent with the single ion properties of Yb in β-$YbAlB_4$, the characteristic energy scale required to fit the experimental results is $T_0 \sim 6.5eV$, far greater than the characteristic Kondo temperature ($\sim 200K$) of this system [61].

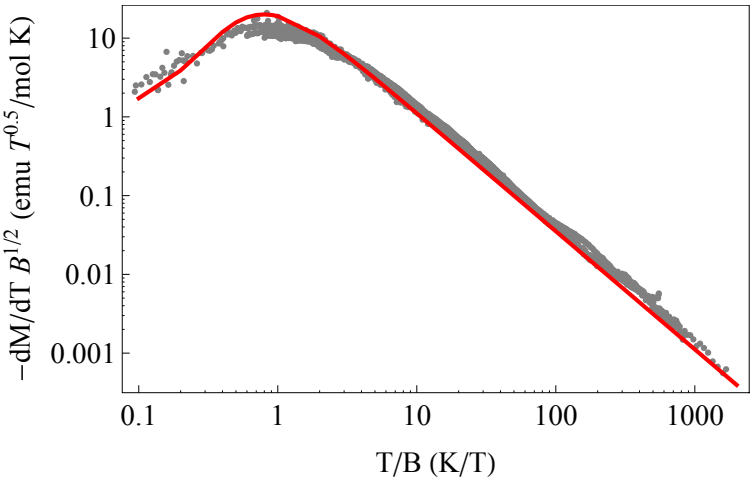

Figure 2.6: Theoretical fit (red line) to the measured field-dependent magnetization of β-$YbAlB_4$ from [61] (gray dots) using Eq. 2.62 with $gm_J = 2.85$ and $T_0 = 6.65eV$.

Using our relationship $T_0 = 4T_K/x^2$, we can understand this scale by assuming that about $x \sim 0.1$ of the f-spectral weight is contained within the vortex metal contribution to the density of states.

2.3.4 Discussion and Perspectives

We now turn to discuss some of the assumptions behind our model. One issue is whether the plane-wave description of the vortex metal survives inclusion of band-structure effects. In this situation, angular momentum is only conserved modulo n$\hbar$, where n refers to the presence of n-fold rotation axis in the Yb site, requiring $n \geq 5$ to avoid any admixture of $|\pm 3/2\rangle$ or $|\pm 1/2\rangle$ states into the perfect $|\pm 5/2\rangle$ doublet. In a model of β-$YbAlB_4$, using tight-binding coupling within the B planes and perfect heptagonal Yb rings, the nodal structure does indeed survive, as shown in Fig. 2.7. However more work is required to understand whether the nodes persist in a more realistic model of β-$YbAlB_4$. Another key assumption is that the the node in the hybridization perfectly pins the f-level to the Fermi surface. Ultimately, this must arise from Coulomb screening, an effect that also needs inclusion in future work.

Support for our model is provided by the locally isostructural polymorph α-$YbAlB_4$, which has a comparable characteristic Kondo scale $T_K \approx 200K$ [86] to the beta phase, but

develops a Fermi liquid ground state [91]. Recent experiments indicate that α-$YbAlB_4$ develops a two dimensional Fermi liquid at fields $B > 3T$ [92], suggesting it is a phase in which the f-level has become detached from the Fermi energy, but that can be tuned towards behavior similar to β-$YbAlB_4$ by large magnetic fields. More direct confirmation of our nodal hybridization model of β-$YbAlB_4$ might be obtained from de Haas-van Alphen measurements. Using Onsager's arguments, the free energy of an extremal orbit of area A_{FS} in the field-doped Fermi liquid will be a periodic function of $\hbar A_{FS}/(2\pi eB)$, and since $A_{FS} \propto \sqrt{B}$, unlike conventional metals, we predict the low-field quantum oscillations will be periodic in $1/\sqrt{B}$ rather than $1/B$.

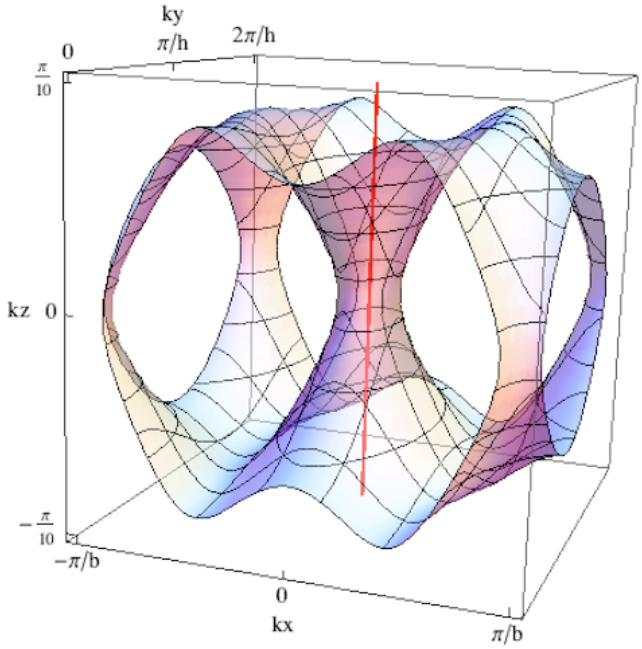

Figure 2.7: Fermi surface from a tight-binding calculation. Note the cylindrical feature along the z-axis linked to an almost 2D surface in the $k_x - k_y$ plane. For clarity, the 1st BZ has been shifted by π/h to move the node into the center of the zone.

Finally, we note that the vortex structure in the hybridization suggests a kind of topological line defect in momentum space. In Kondo insulators, the hybridization vanishes at the high symmetry points forming point defects [81], corresponding to a homotopy $\Pi_2(\mathcal{H}) = \mathbb{Z}_2$. Vortices in the hybridization suggest a further one dimensional homotopy, $\Pi_1(H) = \mathbb{Z}$. This is an interesting direction for future work.

Chapter 3

Theory of the Electron Spin Resonance in β-$YbAlB_4$

This chapter briefly reviews and adds new contributions to the theory for Electron Spin Resonance in heavy fermion systems. Motivated by striking experiments in β-$YbAlB_4$ we develop a phenomenological model based on the Anderson Lattice Model, building up on early works by considering also the effects of spin-orbit coupling, crystal electric fields and hyperfine coupling. We show that the key features of the observed ESR signal in β-$YbAlB_4$, including the shift in the g-factor and the development of anisotropy can be understood as a result of the development of a coherent many-body hybridization between the conduction electrons and the localized f-states. These results are published in *Phys. Rev. Lett. 112, 116405 (2014).*

3.1 Electron Spin Resonance

Electron Spin Resonance (ESR) is traditionally used as a probe of isolated magnetic ions in dilute rare-earth systems [93], but recently emerged as a fascinating new tool to probe the low energy paramagnetic spin fluctuations in heavy fermion systems with the discovery of sharp bulk ESR absorption lines in certain heavy fermion materials.

The technique is based in the following setup: a static magnetic field H Zeeman splits the originally degenerate spin states of a sample inside a resonant cavity in which a transverse microwave field with a given frequency ν_0 is present. The external magnetic field can be tuned and in case the frequency of the microwave field matches the Zeeman energy a resonance condition is satifyed:

$$\Delta E_Z = g_{eff}\mu_B H = \nu_0, \tag{3.1}$$

where g_{eff} is the effective g-factor, μ_B is the Bohr magneton and H the magnitude of the applied static magnetic field. Under this condition some of the radiation in the cavity is absorbed by the electrons when they are excited from the lower to the upper energy level (see Fig. 3.1 top). Succinctly, the ESR experiment probes the absorbed power P of a transverse magnetic microwave field at a fixed frequency ν_0, as a function of an external

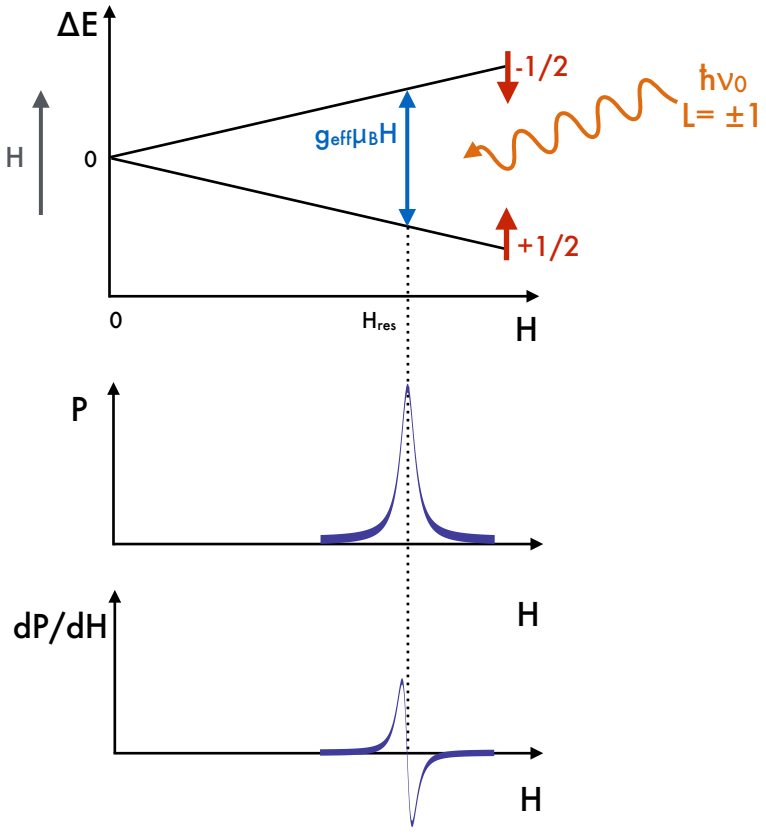

Figure 3.1: Schematic figure depicting the energy levels shift in the presence of magnetic field (top); the power absorption curve with a peak at the resonance field (middle); and the derivative of the absorption curve, which is the form the experimental data is usually displayed (bottom).

In the study of magnetic moments in metals the line-shapes accessed experimentally give us information about the local moment state and the environment surrounding it, which includes neighboring ions and conduction electrons. The main features of the line-shapes are:

- **Resonance position:** The resonance field is given by the field for which the absorption of the microwave power has a maximum (Fig. 3.1 middle), or for which the derivative dP/dH passes through zero (Fig. 3.1 bottom). The resonance condition allows one to extract the effective g-factor as:

$$g_{eff} = \frac{\nu_0}{\mu_B H_{res}}. \tag{3.2}$$

For free electrons $g \sim 2$, and for electrons with strong spin-orbit coupling the g-factor is given by the Landé formula:

$$g_L = \frac{3}{2} + \frac{S(S+1) - L(L+1)}{2J(J+1)}, \tag{3.3}$$

where S, L and J are the spin, orbital, and total angular momentum, respectively.

- **Linewidth:** It gives information about the relaxation of the magnetic moment being probed by ESR. It is extracted as the width (or half width) at half maximum of the resonance peak, as in Fig. 3.2 A). There are several relaxation mechanisms that have distinct temperature dependences [93]. If the relaxation process is dominated by relaxation towards the conduction electrons we have the so called Korringa mechanism [94] with:

$$\Delta H \sim (N(0)J)^2 k_B T, \tag{3.4}$$

where $N(0)$ is the density of states of the conduction electrons at the Fermi level, J the exchange constant between conduction and localized electrons and k_B the Boltzmann constant. Other mechanisms can dominate the relaxation process, as a direct relaxation to the lattice, for example [93]. The system can also be in what is called a "bottleneck regime", in which the relaxation of the angular momentum from the conduction electrons back to the local moments happens faster than the relaxation to the lattice, so effectively the relaxation of the local moments is determined by the small relaxation rate from the conduction electrons to the lattice, leading to a narrowing

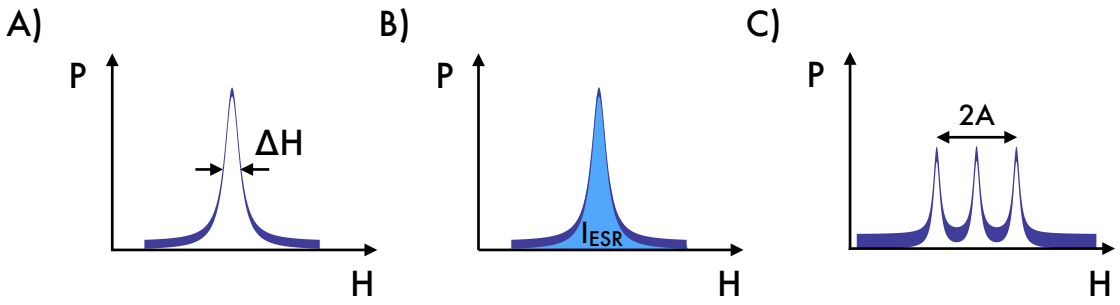

Figure 3.2: Schematic figure depicting the main features of the ESR line shape. A) Indicates the linewidth ΔH as the width at half maximum. B) The shaded area indicates the intensity of the ESR signal. C) Splitting of the ESR resonance in three peaks due to hyperfine coupling, with the splitting being proportional to the hyperfine coupling A.

of the ESR lineshape [93]. Another mechanism that can lead to the narrowing of the linewidth is the proximity to a ferromagnetic transition, in which case the linewidth is essentially reduced by a factor $(1 - \Theta/T)$, where Θ is the Curie-Weiss temperature [93].

In case excited CEF states are present and energetically close to the ground state, they can also be accessed by ESR since they have a finite thermal population. Under this circumstance there is an extra contribution to the relaxation rate is given by:

$$\Delta H \sim e^{-\Delta_X/T}, \tag{3.5}$$

where Δ_X is the magnitude of the CEF splitting.

- **Intensity:** The intensity of the ESR signal is defined as the field integral over the power, or the double field integral over dP/dH:

$$I_{ESR} \propto \int_0^{H_{max}} P(\nu_0, H) dH, \tag{3.6}$$

and can be understood as the area under the absorption curve, as depicted in Fig. 3.2 B).

- **Hyperfine Structure:** The hyperfine structure in ESR lines can be present in case there are nuclei with non-zero magnetic moment **I** in the sample. The nuclear spins

have a much larger relaxation time then the electronic spins, consequently the electrons see the nuclear moments as static and the hyperfine coupling $\mathbf{I}\cdot\mathbf{S}$ generates an effective magnetic field for the local moments, which causes a shift in the ESR resonance proportional to the hyperfine coupling A_{HF}, as depicted in Fig. 3.2 C). The nuclear moments $\mathbf{I}$ can be in any of the allowed $(2I+1)$ states with equal probability, so consequently the ESR lines will acquire a structure with extra $(2I+1)$ resonances with equal intensity [93]. In case there are only a small concentration of isotopes with non-zero nuclear moment, the intensity of the shifted resonances will be proportional to the concentration of isotopes.

3.2 Electron Spin Resonance in Heavy Fermions

Normally, rare-earth ions display an ESR signal when they are weakly coupled to the surrounding conduction sea, acting as dilute "probe atoms". A bulk f-electron ESR signal in heavy fermion metals was unexpected, for here the lattice of local moments is strongly coupled to the conduction electron environment. Naively, one expects the ESR resonance to be washed out by the Kondo effect since the spin-fluctuation rate increases the line-width to values larger than the magnetic field window of most experiments, making the signal undetectable. Given $\Delta H \sim k_B T_K / g_{eff}\mu_B$, a naive prediction for a small $T_K \sim 10K$, using $g_{eff} = 2$, finds $\Delta H \sim 10T$. Yet, surprisingly, sharp ESR lines have been seen to develop at low temperatures in a variety of heavy electron materials. Some examples of heavy fermion materials in which ESR is observed are:

- **YbCuAl** is the heavy fermion compound in which ESR was first observed in the absence of doping by magnetic impurities [95]. A large g-factor shift is seen with $\Delta g \approx -0.4$, and the authors already point our the that the origin of the shift might be related to a gradual mixing between the conduction and f-electrons.

- **$YbRh_2Si_2$** is another heavy fermion which can be accessed by ESR. The anisotropic ESR signal (clear only below 20K) reflects the crystalline structure surrounding the Yb atoms. The intensity of the signal follows a Curie-like behavior, in accordance with the static susceptibility. The width of the resonance displays a linear behavior at low

temperatures due to the relaxation of the local moments in a metallic environment, while at higher temperature the temperature dependence follows an exponential behavior, related to the presence of excited CEF states at higher energies. The authors point out that the presence of local magnetic moments coming from the Yb^{3+} well below the characteristic Kondo temperature $T_K \sim 25K$ indicates a lack of Kondo screening in this regime, related to the proximity to a quantum critical point [96]. Interestingly enough, experiments on $Yb_{1-x}Lu_xRh_2Si_2$ show that the ESR signal only survives up to $x = 0.15$ dilution with non-magnetic Lu, indicating that the ESR signal is a collective resonance of a Kondo lattice rather than a single impurity phenomenon [97, 98].

- **$YbIr_2Si_2$** also displays an anisotropic ESR signal below $T_K \sim 40K$. Again, the intensity of the signal follows the static susceptibility. The width of the resonance is dominated by an activated exponential behavior, what suggests that the main relaxation mechanism for the local moments is by the presence of excited CEF states and not by the Korringa mechanism [99].

- **CeRuPO** is a ferromagnetic Kondo lattice system, while CeOsPO is the homologue antiferromagnetic compound. The fact that the Ru compound displays ESR signal while the Os compound does not suggests that the presence of ferromagnetic fluctuations are important for the narrowing and observation of the ESR signal [100]. They authors in investigate several other compounds and conclude that the presence of ferromagnetic fluctuations might be the key for the observation of ESR signal.

- ESR signals were also observed in **YbBiPt**, **$YbRh_2Pb$** and **YbT_2Zn_{20}** (T=Fe, Co) [101].

- The case of **β-$YbAlB_4$** , in which the ESR signal evolves from a room temperature conduction electron signal into an Ising-anisotropic f-electron signal at low temperatures, is particularly striking. As the temperature is lowered, the g-factor changes from an isotropic $g \approx 2$ to an anisotropic g-factor with magnitude characteristic of the spin-orbit coupled magnetic Yb ions. Moreover, the signal develops hyperfine

satellites characteristic of localized magnetic moments below 10K, yet the intensity of the signal remains constant, a signature of Pauli paramagnetism [88]. In contrast, the same measurements for the reference compound β-$LuAlB_4$ displays no temperature dependence of the ESR line shape, with a constant isotropic $g \approx 2$, no hyperfine structure and constant signal intensity. These results challenge our current understanding and motivate the development of a theory of electron spin resonance in the Anderson lattice.

The observation of ESR signal in both Ce and Yb compounds, close and far from quantum criticality indicates that these are not important parameters for the presence of the signal; by contrast, ferromagnetic correlations (and large Wilson ratios) are a recurrent feature in the systems above, including β-$YbAlB_4$, and seems to play an important role in the narrowing of the otherwise very broad resonance [100, 102].

Previous theories in the Anderson and Kondo lattice [84, 103] have shown that the development of the hybridization between the conduction and f-electrons, giving origin to heavy quasiparticles, and the presence of ferromagnetic exchange interactions between the local moments are two mechanisms that can narrow the otherwise broad ESR line shape in heavy fermion systems. The last mechanism can be understood by the fact that the presence of ferromagnetic fluctuations prevents a spin-flip to be passed on to other sites, what makes the relaxation process more difficult [103]. Note that motional narrowing is also favored in presence of ferromagnetic correlations since the hopping of f-electrons is more favorable if all sites have the same kind of local effective field. Also, the fact that the heavy fermion systems are possibly in a bottleneck regime is an important factor to be considered towards the understanding of the narrow linewidth [102].

These theories cannot pinpoint if the ESR signal seem in $YbRh_2Si_2$ and other heavy fermion systems comes from the local moments or from the conduction electrons. The experiments performed in β-$YbAlB_4$ can shed some light on this point since it will be clear from the discussion in the next section that the signal is originated from the conduction electrons.

3.3 Theory of the Electron Spin Resonance in β-YbAlB$_4$

Here we formulate a phenomenological theory for the ESR of an Anderson lattice containing anisotropic magnetic moments. Our theory builds on earlier works [83, 84, 103], focussing on the interplay between the lattice Kondo effect and the paramagnetic spin fluctuations while considering the effects of spin-orbit coupling, crystal electric field and hyperfine coupling. We show that the key features of the observed ESR signal in β-YbAlB$_4$, including the shift in the g-factor and the development of anisotropy can be understood as a result of the development of a coherent many-body hybridization between the conduction electrons and the localized f-states. We are able to account for the emergence of an hyperfine structure as a consequence of the static Weiss field created by the nuclei of the odd-spin isotopes of Yb. Moreover, using a spectral weight analysis, we show that the constancy of the intensity can be understood as a consequence of the intermediate value of the CEF excitations, comparable to the hybridization strength in this material.

ESR measurements probe the low frequency transverse magnetization fluctuations in the presence of a static magnetic field. The power absorbed from a transverse AC electromagnetic field at fixed frequency ν_0 as a function of the static external magnetic field H, is given by

$$P(\nu_0, H) \propto \chi''_{+-}(\nu_0, H), \tag{3.7}$$

where $\chi''_{+-}(\nu_0, H)$ is the imaginary part of

$$\chi_{+-}(\nu_0, H) = -i \int_0^\infty dt e^{i\nu_0 t} \langle [M_+(t), M_-(0)] \rangle_H \tag{3.8}$$

is the dynamical transverse magnetic susceptibility and $M_\pm = M_x \pm iM_y$ are the raising and lowering components of the magnetization density.

In β-YbAlB$_4$, the Yb ions are sandwiched between two heptagonal rings of boron atoms [60], occupying a magnetic 4f^{13} state with total angular momentum J=7/2. Crystal fields with 7-fold symmetry conserve J_z, splitting the J=7/2 Yb multiplet into four Kramers doublets, each with definite $|m_J|$. Based on the maximal degree of overlap, the Curie constant and the anisotropy of the magnetic susceptibility of β-YbAlB$_4$, the low lying Yb

doublet appears to be $|7/2, \pm 5/2\rangle$, with first excited state $|7/2, \pm 3/2\rangle$ [87, 104].

Since β-$YbAlB_4$ is a mixed valent system we start with an infinite-U Anderson lattice model, based on the overlap of the boron orbitals with the $|7/2, \pm 5/2\rangle$ f-electron ground state doublet and the first excited CEF level, the pure $|7/2, \pm 3/2\rangle$ state, given by

$$H = H_c + H_f + H_{fc} - \mathbf{M}.\mathbf{H}, \tag{3.9}$$

where

$$H_c = \sum_{\mathbf{k},\sigma} \epsilon_{\mathbf{k}} c^\dagger_{\mathbf{k}\sigma} c_{\mathbf{k}\sigma}, \tag{3.10}$$

$$H_f = \sum_{j,\gamma} \epsilon_{f\gamma} \chi_{\gamma\gamma}(j), \tag{3.11}$$

$$H_{fc} = \sum_{j\mathbf{k}\sigma\gamma} (e^{-i\mathbf{k}\mathbf{R}_j} V_{\mathbf{k}\sigma\gamma} c^\dagger_{\mathbf{k}\sigma} X_{0\gamma}(j) + \text{H.c.}) \tag{3.12}$$

describe the conduction electron band (here taken to be a single band for simplicity); the f-electron levels; and the hybridization between them, respectively. Here

$$\mathbf{M} = \sum_j \mu_B \Big(g_c \mathbf{S}_c(j) + g_f \mathbf{J}_f(j) \Big) \tag{3.13}$$

is the total magnetization, with $g_c = 2$ and $g_f = 8/7$ the conduction and f-electron g-factors, $\mathbf{S}_c(j)$ is the conduction electron spin density and $\mathbf{J}_f(j)$ is the total angular momentum operator of the f-states at site j. The operator $c^\dagger_{\mathbf{k}\sigma}$ creates a conduction hole in the boron band with dispersion $\epsilon_{\mathbf{k}}$. The composite Hubbard operators in the slave boson approach can be written as $X_{0\gamma} = (b^\dagger f_\gamma) \equiv |4f^{14}\rangle\langle 4f^{13}, \gamma|$ in terms of the $|4f^{13}, \gamma\rangle \equiv f^\dagger_\gamma |0\rangle$, "hole" states of the Yb^{3+} ion and the filled shell Yb^{2+} state $|4f^{14}\rangle \equiv b^\dagger|0\rangle$, as introduced in Sec. 2.3.2. The azimuthal quantum number $\gamma \equiv m_J$ has values $\gamma \in [\pm 5/2, \pm 3/2]$ corresponding to ground state doublet with energy $\epsilon_{f\pm 5/2} = \epsilon_f$ and the next CEF level, with energy $\epsilon_{f\pm 3/2} = \epsilon_f + \Delta_X$.

3.3.1 Addendum: Energy Scales and Anisotropy Regimes

Now we highlight the main energy scales in this problem and find different regimes of interest. First we compare the Zeeman energy available experimentally with the typical Kondo energy scales: for fields of the order of $H \sim 1T$, the Zeeman energy is of the order of $\Delta E_z \sim 0.1meV \sim 1K$, one to two orders of magnitude smaller than the usual $T_K \sim 10 - 100K$, so we can consider that the Kondo physics is only slightly perturbed by the presence of the magnetic field.

In the ground-state of the Anderson lattice model, the ratio $\tilde{V}^2/W \sim T_K$ determines the Kondo temperature T_K, where $\tilde{V}$ is the characteristic size of the renormalized hybridization (which will be defined in the next subsection) and W is the conduction electron band-width. The degree of magnetic anisotropy in the Kondo lattice is set by the size of the crystal field splitting Δ_X. In a Kondo impurity problem, one can project out the crystal field excited states, provided $\Delta_X/T_K \gtrsim 1$, and crystal symmetry prevents any admixture of the projected states with the Abrikosov-Suhl resonance. However, in a Kondo lattice the non-conservation of crystal symmetry becomes important once $\Delta_X \gtrsim \tilde{V} \sim \sqrt{T_K W}$, a situation that can occur even though $\Delta_X \gg T_K$. In this situation, the hybridization will admix the mobile f-quasiparticles with the higher crystal field states. We shall show that this produces significant modification to the magnetization operator of the quasiparticles. There are thus three regimes of interest:

1. **Ising limit:** $\Delta_X/\tilde{V} \gg 1$, $\Delta_X/T_K \gg 1$;

   In this limit the problem can be projected into the ground state manifold, with the total angular momentum multiplet being substituted by the pseudo-spin operator in the reduced space of states.

2. **Intermediate anisotropy:** $\Delta_X/\tilde{V} \gtrsim 1$, $\Delta_X/T_K \gg 1$;

   This intermediate regime the main features of the ESR experiment can be understood with base on the Ising limit, but the details might depend on the inclusion of the next CEF levels into the theory.

3. **Weak anisotropy:** $\Delta_X/\tilde{V} < 1$;

In case the CEF splitting is smaller than the hybridization strength one should include all the CEF levels in the computation.

3.3.2 Mean Field Approximation

We employ a mean-field approximation $X_{0\gamma}(j) \to r f_\gamma(j)$, where the mean-field amplitude of the slave boson, $r = |\langle b_j \rangle|$ describes the emergence of the Abrikosov-Suhl resonance at each site, resulting from Kondo screening. In the mean field theory, $H \to H_c + \tilde{H}_f + \tilde{H}_{fc} - \mathbf{M}\cdot\mathbf{H}$, where

$$\begin{aligned} \tilde{H}_f &= \sum_{\mathbf{k}\gamma} \tilde{\epsilon}_{f\gamma} f^\dagger_{\mathbf{k}\gamma} f_{\mathbf{k}\gamma} + \lambda(r^2 - 1), \\ \tilde{H}_{fc} &= \sum_{\mathbf{k}\sigma\gamma} \big[c^\dagger_{\mathbf{k}\sigma} \tilde{V}_{\mathbf{k}\sigma\gamma} f_{\mathbf{k}\gamma} + \text{h.c.} \big], \end{aligned} \tag{3.14}$$

whith $\tilde{V}_{\mathbf{k}\sigma\gamma} = V_{\mathbf{k}\sigma\gamma} r$ and $\tilde{\epsilon}_{f\gamma} = \epsilon_{f\gamma} + \lambda$ the renormalized quasiparticle hybridization and f-level energy, and λ the Lagrange multiplier that enforces the average constraint $\langle n_f \rangle + \langle b^\dagger b \rangle = 1$. The temperature dependence of the many body amplitude $r(T)$ determines the evolution of the ESR signal, as will be shown below.

Although β-$YbAlB_4$ almost certainly lies in the Intermediate anisotropy regime, the Ising limit captures most of the physics. In this limit, the $|\pm 3/2\rangle$ and higher CEF states are projected out, leading to a two-band model in which the matrix elements of the transverse f-magnetization $J_f^\pm$ are absent. This happens due to the conservation of angular momentum: the incoming photon has angular momentum $l = 1$ (see Fig. 3.1), so it cannot flip the large Ising spin since the f-electrons are in the $|\pm 5/2\rangle$ state;

$$\langle \pm 5/2 | J^\pm | \pm 5/2 \rangle = 0, \tag{3.15}$$

thus the f-moments do not have a magnetic response to the microwaves and the transverse susceptibility is purely determined by the fluctuations of the conduction electrons magnetization in the presence of a Kondo lattice effect:

$$P(\nu, H) \propto \chi''_{c+-}(\nu, H), \qquad \text{(Ising Limit)} \tag{3.16}$$

and now the absorbed power is proportional to the imaginary part of the conduction electron transverse magnetic susceptibility.

As a

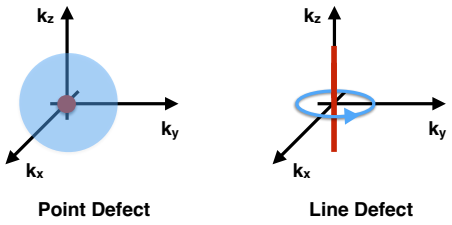

which the complex momen o be spin-diagonal, replaci sceptibility can be calcula ıe following bubble diagrar

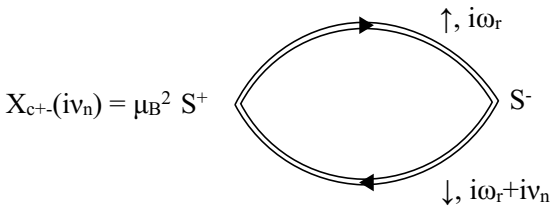

and written as:

$$\chi_{c+-}(i\nu_n) = -\mu_B^2 k_B T \sum_{\mathbf{k},r} G_{c\downarrow}(\mathbf{k}, i\tilde{\omega}_r + i\nu_n) G_{c\uparrow}(\mathbf{k}, i\tilde{\omega}_r). \tag{3.17}$$

Note that the double lines in the bubble diagram above are referent to the effective conduction electron propagator:

$$G_{c\sigma}(\mathbf{k}, z) = [z - \epsilon_{\mathbf{k}\sigma} - \Sigma_{c\sigma}(z)]^{-1}, \tag{3.18}$$

is the conduction electron propagator and $\Sigma_{c\sigma}(z) = V^2 r^2/(z - \tilde{\epsilon}_{f\sigma})$ is the self-energy generated by resonant scattering off f-states. Note also that the Zeeman energy is now absorbed in the definition of the spin dependent dispersions:

$$\epsilon_{\mathbf{k}\sigma} = \epsilon_{\mathbf{k}} - \frac{g_c \mu_B}{2} \boldsymbol{\sigma} \cdot \mathbf{H}, \tag{3.19}$$

$$\epsilon_{f\sigma} = \epsilon_f - \frac{g_f \mu_B}{2} \bar{\boldsymbol{\sigma}} \cdot \mathbf{H}, \tag{3.20}$$

where $\boldsymbol{\sigma}$ refers to the spin for the conduction electrons in the $|\pm 1/2\rangle$ state, and $\bar{\boldsymbol{\sigma}}$ refers to the pseudo-spin for the f-electrons in the $|\pm 5/2\rangle$ state.

Here vertex corrections have been neglected and the spin relaxation has been included as a white noise Weiss field acting on both conduction and f-electrons, shifting the Matsubara frequency by the spin-relaxation rate: $\tilde{\omega}_n = \omega_n + i\frac{\Gamma}{2}\mathrm{sgn}(\omega_n)$.

Carrying out the momentum sum as an energy integral, and expanding the self-energy to linear order in frequency, at low temperatures we obtain, for the magnetic field along the z-direction:

$$\chi_{c+-}(\nu - i\delta, H) = \mu_B^2 Z_c N_c(0) \left(\frac{g^* \mu_B H + i\Gamma}{g^* \mu_B H + i\Gamma - \nu} \right). \tag{3.21}$$

Here $N_c(0)$ is the density of states of the conduction electrons at the Fermi level, $Z_c = (1 - \partial\Sigma_c/\partial\omega)^{-1} = (1 + V^2 r^2/\tilde{\epsilon}_f^2)^{-1}$ is the conduction electron quasiparticle weight and

$$g^* = g_c Z_c + g_f^*(1 - Z_c), \tag{3.22}$$

is the effective g-factor of the new quasiparticles, where $g_f^* = g_f(2m_J) = 5.7$. At high temperatures we have $Z_c = 1$ and consequently $g^* \approx 2$ reflects the conduction character of the Fermi surface, but as the temperature is lowered Z_c diminishes and the g-factor rises towards g_f^* as the Fermi surface acquires f-character.

Temperature dependence

The temperature dependence of the ESR signal is determined by the temperature evolution of the mean field parameters $r(T)$ and $\lambda(T)$. These are computed by the extremization of the free energy, which can be written as:

$$F = -\beta^{-1} \sum_{\mathbf{k},\sigma,n=\pm} ln(1 + e^{-\beta E^n_{\mathbf{k}\sigma}}) + \lambda(r^2 - 1), \tag{3.23}$$

where $\beta^{-1} = k_B T$ and

$$E^{\pm}_{\mathbf{k}\sigma} = \frac{\epsilon_{\mathbf{k}\sigma} + \tilde{\epsilon}_{f\gamma}}{2} \pm \sqrt{\left(\frac{\epsilon_{\mathbf{k}\sigma} - \tilde{\epsilon}_{f\gamma}}{2} \right)^2 + \tilde{V}^2}, \tag{3.24}$$

is obtained by the diagonalization of the mean field Hamiltonian within the assumption that the hybridization is momentum independent and spin-diagonal.

The extremization of the free energy with respect to the mean field parameters r and λ gives two coupled equations:

$$\frac{\partial F}{\partial r} = 0 \Rightarrow \sum_{\mathbf{k},\sigma,n} f(E^n_{\mathbf{k}\sigma}) \frac{\partial E^n_{\mathbf{k}\sigma}}{\partial r} + 2\lambda r = 0, \tag{3.25}$$

$$\frac{\partial F}{\partial \lambda} = 0 \Rightarrow \sum_{\mathbf{k},\sigma,n} f(E^n_{\mathbf{k}\sigma}) \frac{\partial E^n_{\mathbf{k}\sigma}}{\partial \lambda} + r^2 - 1 = 0, \tag{3.26}$$

where $f(\epsilon) = 1/(e^{\epsilon/k_B T} + 1)$ is the Fermi-Dirac distribution.

For the numerical solution we use the equations above in a two dimensional square lattice with hopping parameter $t = 1eV$, chemical potential $\mu = -0.2eV$. The bare location of the f-level is $\epsilon_f = -0.15eV$ and $V = 0.26eV$. The temperature evolution of the mean field parameters is shown in the figure below:

Figure 3.3: Temperature dependence of the mean field parameters r (solid line) and λ (dashed line) determined numerically.

We can now calculate the temperature dependence of the g-factor from the ratio between the photon energy ν_0 and the Zeeman energy $2\mu_B H_{res}(T)$ at the resonance field:

$$g(T) = \nu_0 / 2\mu_B H_{res}(T), \tag{3.27}$$

where H_{res} is determined from the maximum of the imaginary part of the dynamical spin

susceptibility

$$\chi_{c+-}(\nu_0 - i\delta, H) = -\mu_B^2 \sum_{\mathbf{k},n,m=\pm} Z^n_{\mathbf{k}\downarrow} Z^m_{\mathbf{k}\uparrow} \frac{f(E^n_{\mathbf{k}\downarrow}) - f(E^m_{\mathbf{k}\uparrow})}{-\nu_0 + E^n_{\mathbf{k}\downarrow} - E^m_{\mathbf{k}\uparrow} + i\Gamma}, \tag{3.28}$$

where

$$Z^n_{\mathbf{k}\sigma} = \frac{E^n_{\mathbf{k}\sigma} - \epsilon_{f\sigma}}{E^n_{\mathbf{k}\sigma} - E^{-n}_{\mathbf{k}\sigma}}, \tag{3.29}$$

calculated at a fixed frequency, as a function of magnetic field. In our calculations we used the experimental value for the fixed ESR frequency $\nu_0 = 3.9 \times 10^{-5}$eV (for the X-band frequency of 9.5 GHz) and $\Gamma = 7.2 \times 10^{-7} eV$. Note that the definition of $g^* = g_c Z_c + g_f^*(1 - Z_c)$ as a simple closed form for the effective g-factor comes from a zero temperature calculation and gives only the value of the g-factor at the Fermi surface, what is a good estimate of the real value of this parameter. The results of the numerical calculations are plotted in Fig. 3.4 and are qualitatively similar to that observed in β-$YbAlB_4$, but the asymptotic value at low temperatures is twice as large as that seen experimentally.

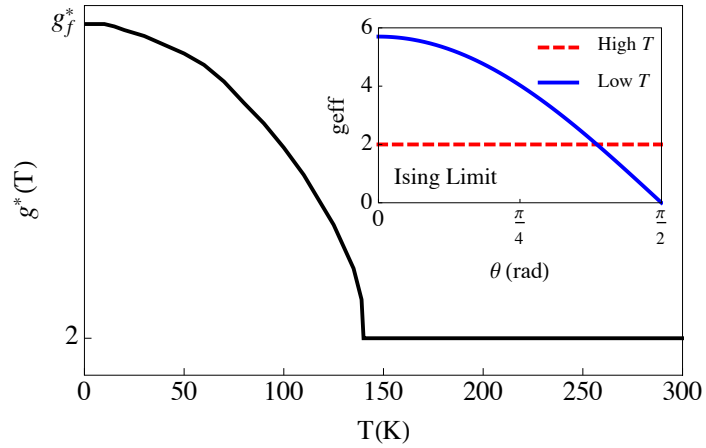

Figure 3.4: Temperature dependence of the g-factor. The value of g_f^* is equal to 5.7 in the Ising limit and smaller for intermediate anisotropy. Inset shows the anisotropy of the g-factor in the Ising limit.

Anisotropy

The computation above was performed for the magnetic field applied along the z-direction. In the Ising limit, the f-band responds uniquely to z-axis fields, so that when a field is

applied at an angle θ out of the z-axis, we may decompose the g-factor in parallel and perpendicular components:

$$g^*_{\|} = g_c Z_c + g^*_f (1 - Z_c), \tag{3.30}$$

$$g^*_{\perp} = g_c Z_c, \tag{3.31}$$

and the effective g-factor as a function of the angle θ can be written as:

$$g^*(\theta) = \sqrt{(g^*_{\|} \sin\theta)^2 + (g^*_{\perp} \cos\theta)^2}. \tag{3.32}$$

At high temperatures $g^*(\theta) = g_c$ is isotropic, but at low temperatures $g^*(\theta) \sim g^*_f \cos\theta$ exhibits extreme Ising anisotropy (see inset of Fig. 3.4).

Note that this anisotropy analysis only considered the anisotropy due to the Ising nature of the local moments. The fact that the hybridization between the conduction and f-electrons is not isotropic will also affect the magnitude and anisotropy of the effective g-factor. The hybridization anisotropy will also give rise to some linewidth broadening due to the different values that g can acquire around the Fermi surface. This effect will depend on the details of the Fermi surface and hybridization function and can be explored in more detail.

Hyperfine Structure

Next we consider the effect of hyperfine coupling on the heavy fermion ESR signal. A small isotopic percentage of the Yb atoms in β-$YbAlB_4$ carry nuclear spins, which give rise to a hyperfine coupling between the f-states and the nuclei.

The hyperfine term in the Hamiltonian can be written as:

$$H_{HF} = A_{HF} \sum_{\{i\}} \mathbf{I}_i \cdot \mathbf{S}_i, \tag{3.33}$$

where A_{HF} is the magnitude of the hyperfine coupling, $\mathbf{I}_i$ the nuclear moment at site i, with the sum over sites which have a non-zero nuclear moment.

The effect of the isotopes ^{173}Yb (I=5/2, present at a concentration $\sim$ 16%) is much smaller than the effect of the isotope^{171}Yb (I=1/2, present at a concentration $\sim$ 14%) since the former has its contribution divided in six new lines, while the last is divided just in two [88, 105]. Here we consider only the presence of the ^{171}Yb isotope. The f-electrons at these sites experience a Weiss field of magnitude A_{HF} that shifts the central energy $\tilde{\epsilon}_f$ of the Abrikosov-Suhl resonance. The dominant isotope ^{170}Yb (present at a concentration $\sim$ 70%) does not carry a nuclear moment.

Since the f-moments are in the pure $|\pm 5/2\rangle$ state there is no spin flip processes allowed by the hyperfine coupling with spin-1/2 nuclear spins, so effectively the hyperfine interaction is this case reduces to $H_{HF} = A_{HF} \sum_{\{i\}} I_i^z S_i^z$ and can be treated as a random potential. Here we consider only multiple scattering on a single impurity given the low concentration of the odd isotopes and the localized character of the f-electrons. When we impurity average over the positions of the isotopic impurities, this modifies the conduction electron self-energy $\Sigma_{c\gamma}(z) \to \Sigma_{c\gamma}(z) + \delta\Sigma_{c\gamma}(z)$, where

$$\delta\Sigma_{c\gamma}(z) = \quad + \quad + \quad + \ldots \tag{3.34}$$

$$= \frac{n_i \tilde{V}^2}{2} \sum_{\sigma=\pm 1} \left(\frac{1}{z - \tilde{\epsilon}_{f\gamma} + A_{HF}\sigma} - \frac{1}{z - \tilde{\epsilon}_{f\gamma}} \right),$$

with the crosses representing the hyperfine field $A_{HF}\sigma$ ($\sigma = \pm 1$). The resulting electron self energy

$$\Sigma_{c\gamma}(z) = \frac{(1-n_i)\tilde{V}^2}{z - \tilde{\epsilon}_{f\gamma}} + \frac{\frac{n_i}{2}\tilde{V}^2}{z - \tilde{\epsilon}_{f\gamma} + A_{HF}} + \frac{\frac{n_i}{2}\tilde{V}^2}{z - \tilde{\epsilon}_{f\gamma} - A_{HF}} \tag{3.35}$$

contains two extra resonances, shifted by the hyperfine coupling constant A_{HF}, which lead to two corresponding side peaks in the ESR lines at low temperatures, as shown in Fig. 3.5. We are thus able to interpret the appearance of hyperfine peaks in the ESR signal of β-$YbAlB_4$ as a consequence of the hyperfine splitting of the resonant scattering in this Kondo lattice.

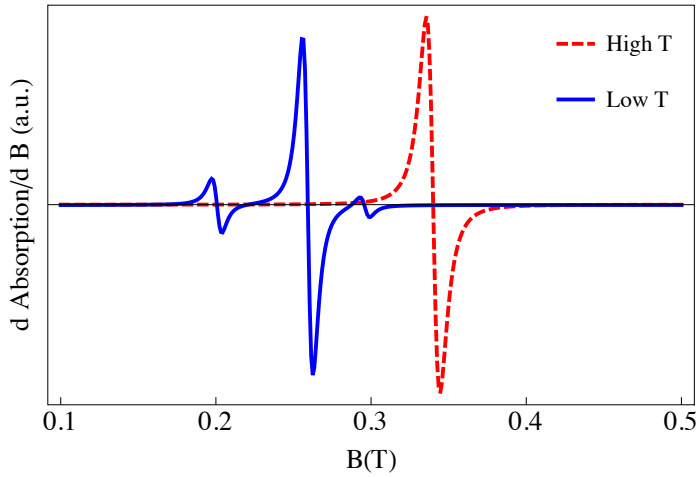

Figure 3.5: ESR line shape computed using the mean-field theory. Note the development of the hyperfine satellite peaks at low temperatures.

Intensity

Now we turn to a discussion of the ESR signal intensity in β-$YbAlB_4$. Here we employ a sum rule relating the quasiparticle, or Pauli component of the magnetization to the ESR intensity. The ESR intensity is the field-integral of the absorbed power:

$$I_{ESR} \propto \int_0^{H_{max}} \chi''_{+-}(\nu_0, H) dH, \tag{3.36}$$

where H_{max} is the maximum field applied and ν_0 the fixed ESR frequency. We can write this in the form

$$I_{ESR} \propto H_0 \int_0^{H_{max}} \frac{\chi''_{+-}(\nu_0, H)}{\nu_0} g^* \mu_B dH, \tag{3.37}$$

using the identity $H_0 = \nu_0/(g^*\mu_B)$ at the resonance field. Due to the narrowness of the peak we can replace $\nu_0 \to \nu$ in the denominator, what makes the integrand an even function of $\nu_0 - g^*\mu_B H$, as can be seen from Eq. 3.21, and it follows that $\chi''_{+-}(\nu_0, H) = \chi''_{+-}(\nu, H_0)$, where $\nu = g^*\mu_B H$. Writing $d\nu = g^*\mu_B dH$, then

$$I_{ESR} \propto H_0 \int_0^{\nu_{max}} \frac{\chi''_{+-}(\nu, H_0)}{\nu} d\nu, \tag{3.38}$$

where $\nu_{max} = g^* \mu_B H_{max}$.

There is also a sum rule for the total transverse static susceptibility, given by the Kramers-Krönig relation:

$$\chi'_{+-}(\nu = 0, H_0) = \frac{1}{2\pi} \int_{-\infty}^{\infty} \frac{\chi''_{+-}(\nu, H_0)}{\nu} d\nu. \tag{3.39}$$

In anisotropic f-electron systems like β-$YbAlB_4$, the transverse susceptibility is dominated by Van Vleck paramagnetism, and is temperature independent. In this situation, (3.39) plays the role of a magnetic f-sum rule. In fact, the static susceptibility

$$\chi'_{Total}(\nu = 0, H_0) = \chi_{\text{Pauli}} + \chi_{VV} \tag{3.40}$$

is a sum of Pauli and Van-Vleck (VV) susceptibilities, where the Pauli contribution derives from low-frequency spin-flip processes, lying within the frequency range detected by ESR, whereas the Van-Vleck contributions derive from much larger frequencies of the order of the crystal-field splitting Δ_X. In this way, we see that the ESR intensity measures the Pauli component of the transverse magnetization,

$$I_{ESR}(T) \propto 2\pi H_0 \chi_{\text{Pauli}}(T). \tag{3.41}$$

Experimentally, both the transverse static susceptibility ($\chi_{Total}(T) = \chi_0$, [106]) and the ESR intensity ($I_{ESR}(T) = I_0$, [88]) are temperature independent. While the large constant value of the total susceptibility reflects its Van-Vleck character, telling us that the total spectral weight in Eq. 3.39 is conserved, the temperature independence of the ESR intensity tells us that the Pauli contribution to the spectral weight is *also* conserved. In the Ising limit, as the hybridization turns on, there is a large reduction in the conduction electron character at the Fermi surface, giving rise to a much reduced transverse magnetization and ESR intensity. Thus to account for these features we need to reinstate the finite CEF.

In the presence of a CEF level, the decomposition of the quasiparticles into conduction

and f-electrons contains an additional amplitude to be in the excited state $|f_{3/2}\beta\rangle$,

$$|n\mathbf{k}\sigma\rangle = a_{n\sigma}|c\mathbf{k}\sigma\rangle + b_{n\alpha}|f_{5/2}\alpha\rangle + c_{n\beta}|f_{3/2}\beta\rangle. \tag{3.42}$$

The low temperature Pauli part of the transverse susceptibility is written as $\chi_{Pauli} = N^*(0)|\langle 1\mathbf{k}\uparrow|M_+|1\mathbf{k}\downarrow\rangle|^2$, where $N^*(0) \sim 1/T_K$ is the low temperature quasiparticle density of states, thus the ratio between the zero and room temperature intensities is given by

$$\frac{I_{ESR}(0)}{I_{ESR}(T > T_K)} \propto \frac{N^*(0)}{N_c(0)} \frac{|\langle 1\mathbf{k}\uparrow|M_+|1\mathbf{k}\downarrow\rangle|^2}{\mu_B^2}, \tag{3.43}$$

where $N_c(0) \sim 1/W$ is the conduction electron density of states and the matrix element squared at high temperatures is equal to μ_B^2. The matrix element squared of the lower band (n=1) is $|\langle 1\mathbf{k}\uparrow|M_+|1\mathbf{k}\downarrow\rangle|^2 = |a_{1\uparrow}a_{1\downarrow} + g_f\sqrt{3}(b_{1\uparrow}c_{1\downarrow} + c_{1\uparrow}b_{1\downarrow})|^2$. Transitions between the 5/2 and 3/2 states happens via an intermediate conduction state:

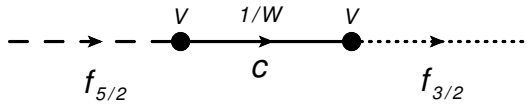

giving rise to a transition matrix element between the crystal field states of magnitude $\tilde{V}^2/W \sim T_K$. The ground-state quasiparticle amplitudes $(a_{1\sigma}, b_{1\alpha}, c_{1\beta})$ are thus of order $(\sqrt{T_K/W}, 1, T_K/\Delta_X)$, respectively. In the pure Ising limit ($\Delta_X \to \infty$) we have $I_{ESR}(0)/I_{ESR}(T > T_K) \sim T_K/W \ll 1$ but at intermediate anisotropy ($\Delta_X/\tilde{V} \gtrsim 1$) new contributions to the transverse magnetization appear and it acquires a value of order unity, $I_{ESR}(0)/I_{ESR}(T > T_K) \sim WT_K/\Delta_X^2 = (\tilde{V}/\Delta_X)^2 \sim 1$.

The preservation of ESR intensity at low temperatures can also be understood in terms of magnetic sum rules (see Fig. 3.3.2). From Eq. 3.38, we see that the ESR signal is a kind of "magnetic Drude peak" in the dynamical spin susceptibility, slightly shifted from zero frequency by the applied magnetic field. In a simple hybridization model with Ising spins, there is a transfer of magnetic Drude weight to high energies, a magnetic analog of the spectral weight transfer which develops in the optical conductivity [107]. However, when a crystal field is introduced, the transfer of spectral weight to high energies is compensated by the downwards transfer of spectral weight from the crystal field levels due to admixture

of $\pm 3/2$ states into the heavy bands. This preserves a fraction of order $O(\tilde{V}/\Delta_X)^2$ of the low frequency spectral weight.

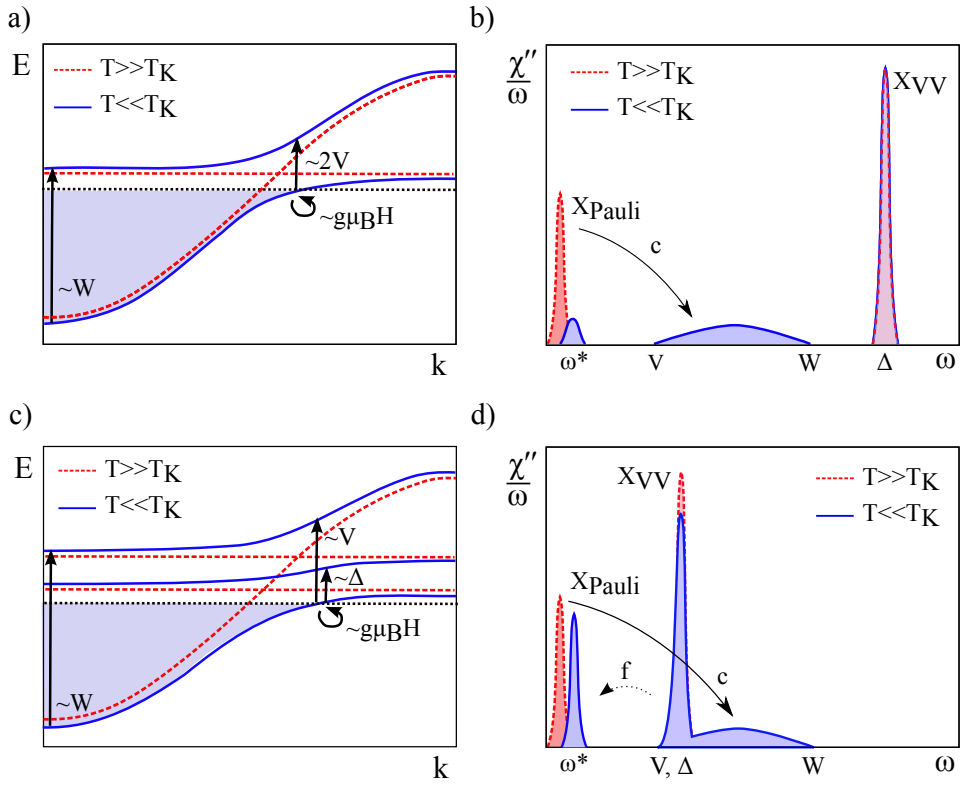

Figure 3.6: Schematic plots of the bands a) Ising limit and c) Intermediate anisotropy. The arrows indicate the order of magnitude of the possible excitations. Imaginary part of the transverse spin susceptibility b) Ising limit and d) Intermediate anisotropy The arrows indicate the flow of spectral weight as the temperature is lowered.

Although we have not calculated it in detail, we note that the intermediate anisotropy limit allows us to understand the reduction of the ESR anisotropy. In particular, the momentum-space anisotropy of the hybridization matrices $V_{\mathbf{k}\sigma\gamma}$ will introduce a k-dependent rotation of the field quantization axes. Quite generally, this effect will broaden the ESR line, reducing both the average value of the g-factor and the degree of anisotropy of the signal.

3.3.3 Perspectives

Our theory suggests various experiments to shed further light on our understanding on the spin paramagnetism of heavy fermion systems. In particular, since β-$YbAlB_4$ is a Pauli

limited superconductor, we expect its upper critical field H_{c2} to be inversely proportional to the effective g-factor, so measuring the angular dependence of H_{c2} would allow us to independently confirm the size and anisotropy of the g-factor on the Fermi surface. It would also be interesting to examine whether similar Ising anisotropic systems, such as $CeAl_3$ or URu_2Si_2 and the recently discovered heavy electron quasicrystal $Au_{51}Al_{34}Yb_{15}$ [63] exhibit ESR signals. Our emergent hybridization model also raises many interesting questions. For example, what is the underlying origin of the sharp f-electron ESR line, which we have modeled phenomenologically? Another aspect that remains unanswered, is the possible connection between the ESR resonance and quantum criticality in both β-$YbAlB_4$ [60, 61, 88, 85, 108] and $YbRh_2Si_2$ [45, 109]. Tantalizingly, α-$YbAlB_4$, a system with a structure locally similar to the β phase does not exhibit a g-shift, yet iron doping appears to drive it into quantum criticality where a g-shift develops in the ESR [110], suggesting these two effects are closely related. Clearly, these are issues for further investigation.

Chapter 4

The Spin Dilemma and Supersymmetric Symplectic Spins

The *spin dilemma* can be simply stated as the ambiguity in the choice of a spin representation in terms of canonical creation an annihilation operators and the consequences a given choice brings to the theoretical description and to our ability to account for different phases of matter. In this chapter we discuss this dilemma and introduce the traditional formalisms, highlighting their successes and limitations. From this discussion we motivate the need to introduce the idea of *supersymmetric symplectic spins*. We define and explore some of the properties of this new spin representation in this chapter.

In this chapter we discuss the ambiguity in the choice of how to write spin operators in terms of canonical creation and annihilation operators in order to approach the heavy fermion problem within a path integral formalism. Spin operators are present in the Kondo model and represent the local moments originated from f-electrons, when both empty and doubly occupied states are projected out and the only remaining degree of freedom of the f-electrons is the spin. In this case the Hilbert space is very constrained, and in order to proceed with canonical operators one needs to make a choice: to write the spin operator using bosons or fermions.

In Section 4.1 we discuss the traditional ways one can write the spin operators in terms of bosons, fermions or even Majorana fermions. From this discussion one can see that different representations are more suitable for the description of different phenomena. Once we are interested in describing systems as heavy fermions, with a complex phase diagram which usually includes magnetic order, heavy Fermi liquid state and superconductivity, we would like to start with an approach that is less biased and would allow us to explore this kind of

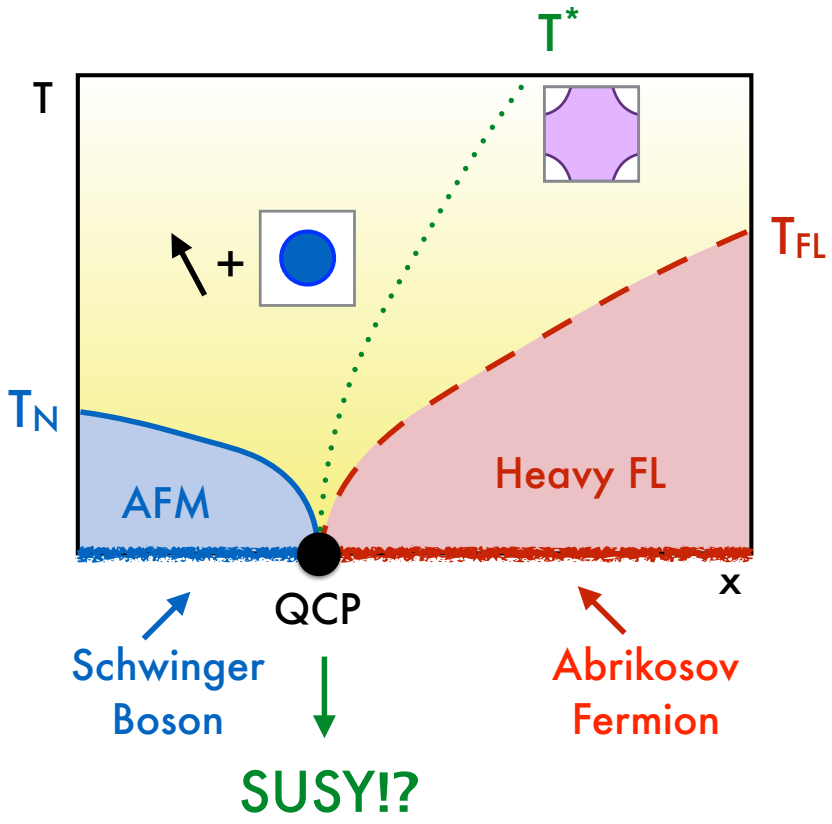

Figure 4.1: Here we revisit the figure of the schematic phase diagram of heavy fermions pointing out the different spin representations that are traditionally used in different regions of the phase diagram.

phase diagram on its entirety. More importantly, if we want to study the character of the quantum phase transitions in these systems, it is not clear which is the most appropriate spin representation to work with.

From Fig. 4.1, we have a suggestive direction to loot at. We know that magnetism is well described in terms of a bosonic representation of the spin (in blue), while a heavy fermion state asks for a fermionic representation of the spin (in red). The phases arbitrarily close to the quantum critical point approaching from the left and from the right appear to be described by completely different representations. If we want to characterize the quantum critical point, we need a description that can properly account for the phases of matter in both sides of the phase transition. One way to unify the approaches discussed above is to build what is called a *supersymmetric* representation, the topic that will permeate the rest of

this thesis. In Sections 4.1 and 4.2 we give more technical motivations for the construction of a supersymmetric symplectic representation of the spin. In Section 4.4 we introduce the necessary definitions and study the properties and implications of a new representation which unifies supersymmetry and symplectic symmetry. The supersymmetric symplectic spin representation provides an approach which carries less bias and is more powerful in accounting for the correct physics in different regions of the phase diagram of heavy fermion systems, as will be shown in the next chapter by the study of two toy models.

4.1 Spin Representations

When modeling systems in the integer valent regime we usually start with effective models in which the operators relative to the f-electrons are in fact spin operators, reflecting the complete loss of the charge degree of freedom of these electrons at low temperatures due to the strong Coulomb repulsion.

Spin operators do not follow canonical commutation relations:

$$[S_a, S_b] = i\epsilon_{abc} S_c, \tag{4.1}$$

so in principle we cannot use the standard many-body techniques as diagrammatic expansion since Wick's theorem cannot be applied in this case [35]. One way to go around this issue is to write the spin operators in terms of creation and annihilation operators plus a constraint or projection operator that will restrict the states to the correct Hilbert subspace. Below we introduce some representations for the spin operators, highlighting its uses and limitations.

4.1.1 Schwinger-Boson representation

In his report to the US Atomic Energy Commission [111], J. Schwinger shows that "the commutation relations of an arbitrary angular momentum vector can be reduced to those of the harmonic oscillator". That means that it is possible to write the spin operator in terms of bosonic creation and annihilation operators. Introducing bosonic operators $(b_\alpha, b_\alpha^\dagger)$ with

an index which can assume two values $(\uparrow, \downarrow)$, following the commutation relations:

$$\begin{aligned} [b_\alpha, b_{\alpha'}] &= [b_\alpha^\dagger, b_{\alpha'}^\dagger] = 0, \\ [b_\alpha, b_{\alpha'}^\dagger] &= \delta_{\alpha,\alpha'}, \end{aligned} \tag{4.2}$$

one can write the spin operators as:

$$\mathbf{S}_B = \sum_{\alpha\alpha'} b_\alpha^\dagger \frac{\boldsymbol{\sigma}_{\alpha\alpha'}}{2} b_{\alpha'}, \tag{4.3}$$

where, for spin-1/2, $\boldsymbol{\sigma}$ are the three Pauli matrices:

$$\sigma_1 = \begin{pmatrix} 0 & 1 \\ 1 & 0 \end{pmatrix}, \qquad \sigma_2 = \begin{pmatrix} 0 & -i \\ i & 0 \end{pmatrix}, \qquad \sigma_3 = \begin{pmatrix} 1 & 0 \\ 0 & -1 \end{pmatrix}. \tag{4.4}$$

Writing the spin components explicitly we have:

$$\begin{aligned} S_1 &= \frac{b_\uparrow^\dagger b_\downarrow + b_\downarrow^\dagger b_\uparrow}{2}, \\ S_2 &= \frac{b_\uparrow^\dagger b_\downarrow - b_\downarrow^\dagger b_\uparrow}{2i}, \\ S_3 &= \frac{b_\uparrow^\dagger b_\uparrow - b_\downarrow^\dagger b_\downarrow}{2} = \frac{n_\uparrow - n_\downarrow}{2}, \end{aligned} \tag{4.5}$$

and using the bosonic commutation relations above it is a straightforward task to show that the commutation relations in Eq. 4.1 for the spin operators are satisfied.

Now the spin states $|\uparrow\rangle$ or $|\downarrow\rangle$ can be written in terms of the bosonic operators acting on the vacuum state $|0\rangle$ as $b_\uparrow^\dagger|0\rangle$ and $b_\downarrow^\dagger|0\rangle$, respectively. Note, though, that the Hilbert space for the bosons actually has many more states, it can be empty or multiply occupied with

several bosons:

$$\begin{aligned} &|0\rangle \Rightarrow \times \\ &\left.\begin{aligned} b_\uparrow^\dagger|0\rangle \Rightarrow \quad &|\uparrow\rangle \\ b_\downarrow^\dagger|0\rangle \Rightarrow \quad &|\downarrow\rangle \end{aligned}\right\} \text{Physical States} \\ &(b_\downarrow^\dagger)^n (b_\uparrow^\dagger)^m |0\rangle \Rightarrow \times \quad \text{for } (m,n) \neq (0,1) \text{ or } (1,0) \end{aligned} \tag{4.6}$$

In order to restrict the states to the physical spin subspace we need to introduce a constraint in the number of bosons $n_B = n_{B\uparrow} + n_{B\downarrow} = 1$. This condition can also be obtained by the analysis on the magnitude of the spin, written in terms of the bosonic operators:

$$\begin{aligned} \mathbf{S}_B \cdot \mathbf{S}_B &= \sum_{\alpha\alpha'} b_\alpha^\dagger \frac{\boldsymbol{\sigma}_{\alpha\alpha'}}{2} b_{\alpha'} \cdot \sum_{\beta\beta'} b_\beta^\dagger \frac{\boldsymbol{\sigma}_{\beta\beta'}}{2} b_{\beta'} \\ &= \frac{1}{4} \sum_{\alpha\alpha'\beta\beta'} b_\alpha^\dagger b_{\alpha'} b_\beta^\dagger b_{\beta'} \boldsymbol{\sigma}_{\alpha\alpha'} \cdot \boldsymbol{\sigma}_{\beta\beta'}, \end{aligned} \tag{4.7}$$

where we can use the completeness relation of the Pauli matrices:

$$\boldsymbol{\sigma}_{\alpha\alpha'} \cdot \boldsymbol{\sigma}_{\beta\beta'} = 2\delta_{\alpha\beta'}\delta_{\alpha'\beta} - \delta_{\alpha\alpha'}\delta_{\beta\beta'}, \tag{4.8}$$

and the bosonic commutation relations above to find:

$$\mathbf{S}_B \cdot \mathbf{S}_B = S(S+1) = \frac{n_B}{2}\left(\frac{n_B}{2} + 1\right), \tag{4.9}$$

where $n_B = \sum_\alpha b_\alpha^\dagger b_\alpha$. Note that we can identify $n_b = 1$ for $S = 1/2$.

This spin representation has been extensively used in the study of magnetism, mainly within large-N treatments, in which case the rotation group of the spin is generalized from SU(2) to a larger group, usually taken to be SU(N) [41, 112, 113]. In this case the spin-spin interactions in the Hamiltonian lead to bosonic interacting terms which can be decoupled by the use of Hubbard-Stratonovich transformations and the solution determined by a saddle point solution in the large-N limit . The bosons can condense below a critical temperature at

which the chemical potential for the bosons reaches zero, indicating the onset of long-range order [114].

4.1.2 Abrikosov-Fermion representation

In an analogous fashion, we can write the spin operator in terms of fermionic operators, as first proposed by Abrikosov and Dzyaloshinski [115]. Abrikosov noticed that the non-commutativity of the spins is what in fact makes the calculation difficult since Wick's theorem does not apply.

Introducing fermionic operators $(f_\alpha, f_\alpha^\dagger)$ with an index which can assume two values $(\uparrow, \downarrow)$ and follow the commutation relations:

$$\begin{aligned} \{f_\alpha, f_{\alpha'}\} &= \{f_\alpha^\dagger, f_{\alpha'}^\dagger\} = 0, \\ \{f_\alpha, f_{\alpha'}^\dagger\} &= \delta_{\alpha,\alpha'}, \end{aligned} \tag{4.10}$$

one can write the spin operators as:

$$\mathbf{S}_F = \sum_{\alpha\alpha'} f_\alpha^\dagger \frac{\boldsymbol{\sigma}_{\alpha\alpha'}}{2} f_{\alpha'}, \tag{4.11}$$

where $\boldsymbol{\sigma}$ are the three Pauli matrices, as defined above for spin-1/2. As for the bosonic representation, one can write the components explicitly and check that the spin commutation relations hold.

Now the spin states $|\uparrow\rangle$ or $|\downarrow\rangle$ can be written in terms of the fermionic operators acting on the vacuum state $|0\rangle$ as $f_\uparrow^\dagger|0\rangle$ and $f_\downarrow^\dagger|0\rangle$, respectively. Note, though, that the Hilbert space for the fermions actually has two more states, it can be empty or doubly occupied:

$$\begin{aligned} &|0\rangle \Rightarrow \times \\ &\left.\begin{aligned} f_\uparrow^\dagger|0\rangle &\Rightarrow \quad |\uparrow\rangle \\ f_\downarrow^\dagger|0\rangle &\Rightarrow \quad |\downarrow\rangle \end{aligned}\right\} \text{Physical States} \\ &f_\downarrow^\dagger f_\uparrow^\dagger|0\rangle \Rightarrow \times \end{aligned} \tag{4.12}$$

In order to restrict the states to the correct spin subspace we proceed as before and introduce a constraint in the number of fermions $n_F = n_{F\uparrow} + n_{F\downarrow} = 1$. This condition can also be obtained by the analysis on the magnitude of the spin, written in terms of the fermionic operators:

$$\begin{aligned} \mathbf{S}_F \cdot \mathbf{S}_F &= \sum_{\alpha\alpha'} f_\alpha^\dagger \frac{\boldsymbol{\sigma}_{\alpha\alpha'}}{2} f_{\alpha'} \cdot \sum_{\beta\beta'} f_\beta^\dagger \frac{\boldsymbol{\sigma}_{\beta\beta'}}{2} f_{\beta'} \\ &= \frac{3n_F(2-n_F)}{4}, \end{aligned} \tag{4.13}$$

where $n_F = \sum_\alpha f_\alpha^\dagger f_\alpha$. Note that for $S = 1/2$, we can identify $n_F = 1$.

The fermionic spin representation seems to be a more natural representation given the fact that the spins we are talking about are actually localized electrons, therefore fermions, with a constrained Hilbert space due to the large Coulomb repulsion. This representation was first proposed in the treatment of the Kondo impurity model [115] and is very appropriate for problems in which spins interact with other electrons which have their complete set of degrees of freedom. In case of a large spin, within a bosonic representation, the spin can only be partially screened since only one boson can be in an antisymmetric state with the fermionic conduction electrons; in order to compeltely screen the spin one needs to introduce other conduction electron channels. On the other hand, a large spin within a fermionic representation can be successfully screened if there are enough conduction electrons available. Within the Kondo lattice model, due to the fermionic character of the excitations in the heavy fermi liquid state, a fermionic representation of the spin is more appropriate if one is interested in describing this metallic phase of matter.

Despite this advantage in the description of the Kondo physics, the fermionic representation is not very successful in the description of magnetism, with the fermionic mean field theories usually giving higher energy solutions if compared to the bosonic counterpart.

From the discussion above on the Schwinger boson and Abrikosov fermion representations of the spin, one can conclude that each spin representation properly satisfies the spin commutation relations and that the Hilbert space can be appropriately constrained so we explore only the physical states related to the original spin states. In principle these

representations are completely equivalent. But once we apply them to different problems this statement does not hold anymore.

4.1.3 Other spin representations

The Schwinger-boson and Abrikosov-fermion representations described above are not the only possible ways to write the spin in terms of canonical operators. Below we briefly introduce other spin representations in terms of spin operators.

Holstein-Primakoff

The Holstein-Primakoff representation was introduced with the aim of studying the small deviations of the spin from a fully polarized state [116]. In this case the spin is written as:

$$\begin{aligned} S_+ &= S_x + iS_y = \sqrt{2S - b^\dagger b}\ b, \\ S_- &= S_x + iS_y = b^\dagger \sqrt{2S - b^\dagger b}, \\ S_z &= S - b^\dagger b, \end{aligned} \tag{4.14}$$

where S is the magnitude of the spin (and its maximum component in the z-direction) and b a bosonic operator. Note that $b^\dagger b$ gives a measure of the deviation of the spin from the fully polarized state in the z-direction. This representation has the inconvenience of the square root of operators, which is ultimately expanded, what is justified for $b^\dagger b/2S \ll 1$. This representation leads to the well known spin wave theory of magnetism [41].

Majorana Fermion Representation

The Majorana fermion representation was introduced in condensed matter theory by A. M. Tsvelik as an interesting way to study antiferromagnets with strong quantum fluctuations in order to describe spin-liquid states [117]. In this representation the states built from the Majorana fermions are only (several copies of the) physical states so a constraint is not required. Once there are no constraints, the trial state gives a variational upper bound for

the ground-state energy. The spin operator can be written as:

$$S_a = -i\epsilon_{abc}\eta_b\eta_c, \tag{4.15}$$

where η_i are real fermions following the anti-commutation relations:

$$\{\eta_a, \eta_b\} = \delta_{ab}, \tag{4.16}$$

and $a, b, c = \{1, 2, 3\}$ label three different kinds of fermions.

Drone Fermion Representation

This representation was used by Kenan [118] and is essentially a fermionic representation of the spin that uses an auxiliary (drone) fermion in order to guarantee the commutativity of the spin in different sites. Noticing that fermionic operators follow:

$$(c_i)^2 = 0, \qquad (c_i^\dagger)^2 = 0, \qquad c_i c_i^\dagger + c_i^\dagger c_i = 1 \tag{4.17}$$

and that these relations resemble the behavior of the Pauli matrices:

$$(\sigma_i^-)^2 = 0, \qquad (\sigma_i^+)^2 = 0, \qquad \sigma_i^+\sigma_i^- + \sigma_i^-\sigma_i^+ = 1, \tag{4.18}$$

one is led to identify [119]:

$$\sigma_i^+ \to c_i^\dagger, \tag{4.19}$$

$$\sigma_i^- \to c_i. \tag{4.20}$$

The issue with this mapping is the fact that the spin operators commute in different sites but the fermionic operators anticommute in different sites. One can introduce auxiliary fermionic operators $(d_i, d_i^\dagger)$ at each site, which anticommute with the original fermionic operators $(c_i, c_i^\dagger)$ in order to guarantee the commutation of the spins in different sites. A

construction that achieves this objective is:

$$\begin{aligned} S_i^+ &= c_i^\dagger (d_i + d_i^\dagger), \\ S_i^- &= (d_i + d_i^\dagger) c_i, \\ S_i^z &= c_i^\dagger c_i - 1/2. \end{aligned} \tag{4.21}$$

It is interesting to notice that the Majorana and Drone fermion representations are actually related [120]. We can write three Majorana fermions in terms of only two complex fermions as:

$$\eta_1 = \frac{(c^\dagger + c)}{\sqrt{2}}, \qquad \eta_2 = \frac{(c^\dagger - c)}{i\sqrt{2}}, \qquad \gamma_3 = \frac{(d^\dagger + d)}{\sqrt{2}}, \tag{4.22}$$

in which case the Majorana representation leads to the drone representation.

4.2 Symplectic Spins

One of the defining characteristics of the spin operator $\mathbf{S}$ is its property of inverting under time reversal $\mathcal{T}$:

$$\mathcal{T}\mathbf{S} = -\mathbf{S}. \tag{4.23}$$

When writing spin Hamiltonians we have terms as $\mathbf{S} \cdot \mathbf{S}$ which are invariant under time reversal and under SU(2) transformations. As these invariances are independent, it follows that:

$$[\mathcal{T}, U] = 0, \tag{4.24}$$

where U is an SU(2) transformation. If we now write the time-reversal operator as $\mathcal{T} = \boldsymbol{\epsilon} K$, where $\boldsymbol{\epsilon} = \epsilon_{ab}$ is an antisymmetric matrix and K is the complex conjugation operation, it follows that:

$$U \boldsymbol{\epsilon} U^T = \boldsymbol{\epsilon}, \tag{4.25}$$

a condition which states that an orthogonal transformation by U should leave an anti-symmetric matrix invariant. This is a symplectic condition, and SU(2) transformations do follow it since $SU(2) \sim SP(2)$.

As mentioned previously in this thesis, when dealing with strongly correlated systems large-N approaches are very convenient as a way to perform controlled calculations. The large-N parameter usually comes from generalizing the rotation group of the spin from SU(2) to a larger group, usually taken as SU(N). Turns out that the SU(N) generalization does not follow the symplectic condition above, therefore it is not in accordance with one of the fundamental properties of the spin. As thoroughly explored by Flint [121], the symplectic-N generalization preserves this property and that is the one we are going to use in this work.

On the top of satisfying a very fundamental property of the spin, there are a couple of advantages that we bring in to our theory by using the symplectic-N generalization:

- **Geometric Frustration**: For the study of antiferromagnetism the SU(N) generalization is restricted to the study of bipartite lattices, in which a given representation and its conjugate are assigned to each sublattice [41, 112, 113]. This assignment is necessary since the product of a representation and its conjugate always include a singlet in its decomposition, fact that is not true for the product of a generic representation with itself, unless it is self-conjugate. In case of geometrical frustration as in the triangular or Kagome lattices, in which there is no bipartite structure, this approach fails to describe magnetism since it does not provide a systematic way to form singlets with spins in neighboring sites.

  A first step in the solution of this issue was proposed by Read and Sachdev by the generalization of SU(2) to SP(N) in stead of SU(N) [122]. The advantage of this generalization is that the product of a representation with itself in SP(N) always includes a singlet, so one can assign the same representation in every site and be able to form singlets consistently. In this approach the spin-spin interacting terms in the Hamiltonian are decoupled in terms of antiferromagnetic bond variables. Recently, Coleman and Flint proposed what is called the *symplectic-N* generalization which includes the decoupling of the spin-spin interacting terms by means of antiferromagnetic

bond variables and variables that promote the resonance of these bonds [121, 123]. This is a more appropriate description for frustrated systems since it introduces the possibility of both ferro and antiferromagnetic correlations.

- **Superconductivity**: Within an SU(N) generalization of the rotation group of the spin, Kondo-like terms can only be decoupled in the particle-hole channel. Based on the known SU(2) symmetry of the fermionic spin representation [124], previous works would perform an SU(2) rotation of the fermions as an after thought in order to be able to decouple the interacting terms in the particle-particle channel as well [125]. The use of the symplectic-N generalization naturally brings into the problem terms that can be decoupled in the particle-particle channel in the large-N limit, so superconductivity can be properly accounted for.

Note that within the symplectic-N generalization we still fall in the dilemma of choosing a bosonic of fermionic representation for the spin.

4.2.1 Bosonic symplectic-N

The generalization of the bosonic spin representation in the symplectic-N approach can be written as:

$$\mathbf{S}_B = \sum_{\alpha\alpha'} b^\dagger_\alpha \frac{\mathbf{\Gamma}_{\alpha\alpha'}}{2} b_{\alpha'}, \tag{4.26}$$

where $\mathbf{\Gamma}$ are the $N(N-1)/2$ generators of the symplectic group SP(N), for N even. These follow the completeness relation:

$$\mathbf{\Gamma}_{\alpha\alpha'} \cdot \mathbf{\Gamma}_{\beta\beta'} = \delta_{\alpha\beta'}\delta_{\alpha'\beta} - \tilde{\alpha}\tilde{\beta}\delta_{\alpha-\beta}\delta_{\beta'-\alpha'}, \tag{4.27}$$

where $\tilde{\alpha} = sign(\alpha)$. As before, to guarantee we are working on the physical subspace we need to fix the value of $\mathbf{S}_B \cdot \mathbf{S}_B$:

$$\begin{aligned} \mathbf{S}_B \cdot \mathbf{S}_B &= \sum_{\alpha\alpha'} b_\alpha^\dagger \frac{\mathbf{\Gamma}_{\alpha\alpha'}}{2} b_{\alpha'} \cdot \sum_{\beta\beta'} b_\beta^\dagger \frac{\mathbf{\Gamma}_{\beta\beta'}}{2} b_{\beta'}, \\ &= \frac{N^2}{4} \frac{n_B}{N} \left(\frac{n_B}{N} + 1 \right), \end{aligned} \tag{4.28}$$

which falls back into the SU(2) constraint for $N = 2$.

Here we note that writing the spin as in Eq. 4.26 we introduce some redundancy to the problem: we can introduce an arbitrary phase $b_\alpha \to e^{i\phi} b_\alpha$, so that the spin is left invariant. This means that there is an U(1) local gauge invariance in the description of the spin in terms of bosonic operators.

The bosonic spin representations can be labelled by Young diagrams (for a brief introduction to Young diagrams see Appendix B.1). In this case the indexes composing the spin are all symmetrized given the commutation relation of the bosons, and the Young diagrams are depicted as a single row of boxes:

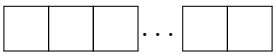

with the number of boxes ranging from one to infinity. The number of boxes, or n_B in this case, defines which representation of the spin we are working with and assigns a magnitude for the spin.

4.2.2 Fermionic symplectic-N

In analogous fashion, we can write down the symplectic-N generalization for the fermionic spin representation introduced above:

$$\mathbf{S}_F = \sum_{\alpha\alpha'} f_\alpha^\dagger \frac{\mathbf{\Gamma}_{\alpha\alpha'}}{2} f_{\alpha'}, \tag{4.29}$$

where $\mathbf{\Gamma}$ are the $N(N-1)/2$ generators of the symplectic group SP(N) for N even. In order to guarantee we are working on the physical subspace we need to fix the value of $\mathbf{S}_F \cdot \mathbf{S}_F$:

$$\begin{aligned} \mathbf{S}_F \cdot \mathbf{S}_F &= \sum_{\alpha\alpha'} f^\dagger_\alpha \frac{\mathbf{\Gamma}_{\alpha\alpha'}}{2} f_{\alpha'} \cdot \sum_{\beta\beta'} f^\dagger_\beta \frac{\mathbf{\Gamma}_{\beta\beta'}}{2} f_{\beta'}, \\ &= \frac{N^2}{4}\left[\frac{n_F}{N}\left(1+\frac{2}{N}-\frac{n_F}{N}\right)-\frac{\Psi^\dagger\Psi}{N^2}\right], \end{aligned} \tag{4.30}$$

where now

$$\Psi = \frac{1}{2}\sum_\alpha \tilde{\alpha} f_{-\alpha} f_\alpha, \tag{4.31}$$

$$\Psi^\dagger = \frac{1}{2}\sum_\alpha \tilde{\alpha} f^\dagger_\alpha f^\dagger_{-\alpha}. \tag{4.32}$$

Perhaps a more interesting way to look at this constraint is the following:

$$\mathbf{S}_F \cdot \mathbf{S}_F = \frac{N}{4}\left(\frac{N}{4}+1\right) - \mathbf{\Psi}\cdot\mathbf{\Psi}, \tag{4.33}$$

where $\mathbf{\Psi} = \frac{1}{2}(\Psi_1, \Psi_2, \Psi_3)$ is a three component vector which components are the following fermionic bilinears:

$$\begin{aligned} \Psi_1 &= \frac{\Psi^\dagger + \Psi}{2}, \\ \Psi_2 &= \frac{\Psi^\dagger - \Psi}{2i}, \\ \Psi_3 &= n_F - N/2. \end{aligned} \tag{4.34}$$

Here we note that the bilinears above actually follow an SU(2) commutation relation:

$$[\Psi_a, \Psi_b] = 2i\epsilon_{abc}\Psi_c, \tag{4.35}$$

and commute with the spin operator:

$$[\mathbf{S}_F, \Psi_a] = 0, \tag{4.36}$$

for $a, b, c = \{1, 2, 3\}$, what means that the spin operator is invariant under transformations generated by these operators. So, in the case of a fermionic representation of the spin, the gauge invariance that is introduced is a local SU(2).

Since fermionic operators anticommute, they give rise to a completely antisymmetric representation of the spin, depicted by column Young diagrams:

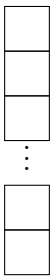

4.3 Supersymmetric Spins

Following the motivations above we can now construct a supersymmetric spin representation of the spin as an unification of the previously introduced bosonic and fermionic representations. First we review the history of the supersymmetric spin operators in condensed matter physics and its potential.

Supersymmetric spin operators were first proposed by Coleman and Gan [126] with the aim of studying the micromagnetism experimentally observed in some heavy fermions at the time. They focused on the single underscreend impurity Kondo model as a toy model which includes both Fermi liquid excitations and magnetic degrees of freedom [127]. The authors already identify the need for a *two-fluid* description, in which they assign a bosonic character to the part of the spin which is not screened and a fermionic character to part screened by the conduction electron spins. It is curious that the two-fluid picture proposed in this work came much before the phenomenological construction of the two-fluid picture [72, 73, 74].

A few years later Pépin and Lavagna [128] propose an enlarged representation of the spin, writing:

$$\mathbf{S} = \mathbf{S}_F + \mathbf{S}_B = \sum_{\alpha\alpha'} \left(f_\alpha^\dagger \frac{\boldsymbol{\sigma}_{\alpha\alpha'}}{2} f_{\alpha'} + b_\alpha^\dagger \frac{\boldsymbol{\sigma}_{\alpha\alpha'}}{2} b_{\alpha'} \right), \tag{4.37}$$

where $\boldsymbol{\sigma}$ are the Pauli matrices in case of a spin-1/2, which is essentially a combination of the previously proposed bosonic and fermionic representations. Note now that there is again an over counting of states: besides the already discussed non-physical states for the bosonic and fermionic cases (which can be dealt with by the implementation of the constraint $n_B + n_F = 1$), now there are two states associated with each spin state:

$$\left.\begin{matrix} f^\dagger_\uparrow|0\rangle \\ b^\dagger_\uparrow|0\rangle \end{matrix}\right\} |\uparrow\rangle, \qquad\qquad \left.\begin{matrix} f^\dagger_\downarrow|0\rangle \\ b^\dagger_\downarrow|0\rangle \end{matrix}\right\} |\downarrow\rangle.$$

The authors suggest that this double counting of states does not interfere in the computation of physical quantities since both representations are faithful representations of the spin. The new feature of this work is that they find the ratio of bosons and fermions self-consistently for a given value of the Kondo coupling over the bandwidth.

The next step by Coleman, Pépin and Tsvelik [129] proposes a large-N treatment of the supersymmetric spin by generalizing the rotation group of the spin from SU(2) to SU(N). Within this approach they showed that it is possible to develop a treatment in which both the Kondo physics and magnetism can be considered concomitantly. The focus now was to understand the character of the antiferromagnetic quantum critical points in heavy fermions from a different perspective, after the observation of spin correlations which are critical in time in $CeCu_{1-x}Au_x$ [71]. They introduce the notation of Young diagrams to the discussion in order to label different spin representations and note that for an SU(2) spin-1/2 the Young diagram is a single box which can have either bosonic or fermionic character, but as SU(2) is generalized to a larger group there is a whole new plethora of representations one can work with, as schematically depicted in Fig. 4.2.

The study and application of the SU(N) supersymmetric spins was limited to the investigation of the single impurity Kondo model, what suggests that more work on this area is needed to elucidate the real potential of this spin representation. Also, given the discussion in the previous subsection a symplectic-N generalization seems to be more appropriate. Below we introduce the *supersymmetric-symplectic spins* for large-N approaches.

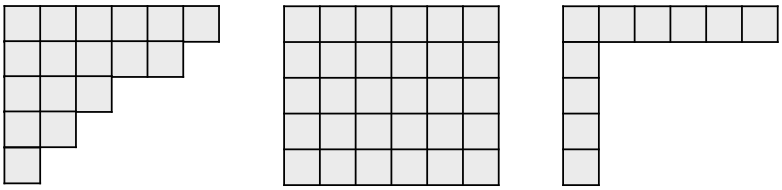

Figure 4.2: Young diagrams. Left: generic diagram. Center: rectangular diagram. Right: L-shaped diagram.

4.4 Supersymmetric-Symplectic Spins

We start defining the supersymmetric-symplectic spin as:

$$S^a = \sum_{\sigma\sigma'} \left(f^\dagger_\sigma \frac{\Gamma^a_{\sigma\sigma'}}{2} f_{\sigma'} + b^\dagger_\sigma \frac{\Gamma^a_{\sigma\sigma'}}{2} b_{\sigma'} \right), \tag{4.38}$$

where $f^\dagger_\sigma(b^\dagger_\sigma)$, $f_\sigma(b_\sigma)$ are fermionic (bosonic) creation and annihilation operators of particles with spin component σ and Γ^a are the generators of the $sp(N)$ algebra, with $a = 1, ...N(N+1)/2$, which follow the completeness relation:

$$\sum_a \Gamma^a_{\sigma_1\sigma_2} \cdot \Gamma^a_{\sigma_3\sigma_4} \quad = \quad \delta_{\sigma_1\sigma_4}\delta_{\sigma_2\sigma_3} - \epsilon_{\sigma_1\sigma_3}\epsilon_{\sigma_2\sigma_4}. \tag{4.39}$$

Alternatively, the supersymmetric-symplectic spin can also be written as:

$$S_{\sigma\sigma'} = f^\dagger_\sigma f_{\sigma'} - \tilde{\sigma}\tilde{\sigma}' f^\dagger_{-\sigma'} f_{-\sigma} + b^\dagger_\sigma b_{\sigma'} - \tilde{\sigma}\tilde{\sigma}' b^\dagger_{-\sigma'} b_{-\sigma}, \tag{4.40}$$

where $\tilde{\sigma} = sgn(\sigma)$. In this form the oddness of the spin under time reversal is made explicit. Note that the way the spin components are labelled now differs from the labeling in Eq. 4.38. In SP(N) $\sigma = -N/2, ..., N/2$, assuming N different values (for N even), so apparently there are N^2 components. Note that not all $S_{\sigma\sigma'}$ are independent and one can show that the correct number of independent components in this representation is $N(N+1)/2$. This can be checked by noticing that $S_{\sigma\sigma'} = -\tilde{\sigma}\tilde{\sigma}' S_{-\sigma'-\sigma}$, so the generators are not all independent. For $\sigma, \sigma' > 0$, we have $S_{\sigma\sigma'} = -S_{-\sigma'-\sigma}$, so the generators with both indexes negative are linearly dependent on the generators with both indexes positive.

For $\sigma > 0, \sigma' < 0, \sigma \neq -\sigma'$ we have $S_{\sigma\sigma'} = S_{-\sigma'-\sigma}$, but note that for the case of $\sigma = \sigma'$ we have the condition $S_{\sigma,-\sigma} = S_{\sigma,-\sigma}$, which does not give a relation between the generators in the off diagonal. One can check that indeed $S_{\sigma,-\sigma}$ is not linearly dependent on $S_{-\sigma,\sigma}$. Within these considerations the number of independent spin components is $N(N+1)/2$, as expected.

More concisely the spin can be written as:

$$S_{\sigma\sigma'} = \Psi^{\dagger}_{\sigma}\gamma_0\Psi_{\sigma'} = \bar{\Psi}_{\sigma}\Psi_{\sigma'}, \tag{4.41}$$

with $\bar{\Psi}_{\sigma} = \Psi^{\dagger}_{\sigma}\gamma_0$ after the introduction of the spinors,

$$\Psi_{\sigma} = \begin{pmatrix} f_{\sigma} \\ \tilde{\sigma} f^{\dagger}_{-\sigma} \\ b_{\sigma} \\ \tilde{\sigma} b^{\dagger}_{-\sigma} \end{pmatrix}, \tag{4.42}$$

and the matrix

$$\gamma_0 = \begin{pmatrix} 1 & 0 & 0 & 0 \\ 0 & 1 & 0 & 0 \\ 0 & 0 & 1 & 0 \\ 0 & 0 & 0 & -1 \end{pmatrix}. \tag{4.43}$$

4.4.1 Symmetries of the Supersymetric Symplectic Spin

The supersymmetric-symplectic spin commutes with the following operator bilinears and the respective conjugates:

$$\begin{aligned} \hat{n}_F &= f_\sigma^\dagger f_\sigma, \\ \hat{n}_B &= b_\sigma^\dagger b_\sigma, \\ \hat{\psi} &= \tilde{\sigma} f_\sigma f_{-\sigma}, \\ \hat{\theta} &= b_\sigma^\dagger f_\sigma, \\ \hat{\eta} &= \tilde{\sigma} f_\sigma b_{-\sigma}, \end{aligned} \tag{4.44}$$

in which an implicit sum over σ should de understood. Note that $\hat{\psi}$ and $\hat{\eta}$ are present in the symplectic but not in the SU(N) generalization of the supersymmetric spin [129]. Note also that $\hat{n}_F, \hat{n}_B$ and $\hat{\Psi}$ have bosonic character, while $\hat{\theta}$ and $\hat{\eta}$ have fermionic character.

We can redefine these operators in order to make the symmetry of the supersymmetric-symplectic spin more evident:

$$\begin{aligned} \psi_0 &= \hat{n}_B + N/2, \\ \psi_1 &= \frac{\hat{\psi}^\dagger + \hat{\psi}}{2}, \\ \psi_2 &= \frac{\hat{\psi}^\dagger - \hat{\psi}}{2i}, \\ \psi_3 &= \hat{n}_F - N/2, \\ A_1 &= \hat{\theta} - \hat{\theta}^\dagger, \\ A_2 &= -i(\hat{\theta} + \hat{\theta}^\dagger), \\ B_1 &= \hat{\eta} - \hat{\eta}^\dagger, \\ B_2 &= -i(\hat{\eta} + \hat{\eta}^\dagger), \end{aligned} \tag{4.45}$$

so that the bosonic operators are Hermitian and the fermionic operators are anti-Hermitian.

These form a representation of the super-algebra $su(2|1)$ [130]:

$$\left.\begin{array}{l} \psi_0 \quad \}\mathrm{U}(1) \\ [\psi_a, \psi_b] = 2i\epsilon_{abc}\psi_c \quad \}\mathrm{SU}(2) \end{array}\right\} \text{Even}$$

$$\left.\begin{array}{l} \{A_n, A_m\} = -2\delta_{nm}(\Psi_0 + \Psi_3) \\ \{B_n, B_m\} = -2\delta_{nm}(\Psi_0 - \Psi_3) \\ \{A_n, B_m\} = \delta_{nm}(\delta_{1n} - \delta_{2n})\Psi_1 + (1 - \delta_{nm})\Psi_2 \end{array}\right\} \text{Odd} \tag{4.46}$$

where $a, b, c = \{1, 2, 3\}$ and $m, n = \{1, 2\}$. Note the $U(1)$ sub-algebra generated by ψ_0, related to phase redundancy of the bosonic part of the spin; the $SU(2)$ sub-algebra generated by $\psi_{i=1,2,3}$, coming from the possible rotations of the fermionic part of the spin. These two sub-algebras together form the even part of the super-algebra, the part that closes under commutation on itself. The operators with fermionic character A_n and B_n form the odd part of the super-algebra; they follow anti-commutation relations which close into the even part of the super-algebra; these are present due to the supersymmetric character of the spin.

Note that one can perform a super-rotation on the spinors $\Psi_\sigma \to g\Psi_\sigma$ such that the spin is left invariant:

$$S_{\sigma\sigma'} = \Psi^\dagger_\sigma \gamma_0 \Psi_{\sigma'} \to \Psi^\dagger_\sigma g^\dagger \gamma_0 g \Psi_{\sigma'}, \tag{4.47}$$

if g satisfies

$$g^\dagger \gamma_0 g = \gamma_0, \tag{4.48}$$

what is essentially the unitarity condition to the transformation after taking appropriate care of the commutativity of the bosons.

The most general transformation g can be obtained by exponentiation of the generators

of the algebra introduced in Eqs. 4.45. Exponentiation of the even part of the algebra gives:

$$g_E = \begin{pmatrix} u & v & 0 & 0 \\ -\bar{v} & \bar{u} & 0 & 0 \\ 0 & 0 & x & 0 \\ 0 & 0 & 0 & \bar{x} \end{pmatrix}, \tag{4.49}$$

where the parameters u, v and x are complex numbers satisfying $|u|^2+|v|^2 = 1$ and $|x|^2 = 1$. Note the SU(2) and U(1) substructure of this transformation for the fermionic and bosonic parts of the spinor Ψ_σ, respectively.

Exponentiating the odd part of the algebra we find:

$$g_A = \begin{pmatrix} 1+\frac{\alpha\bar{\alpha}}{2} & 0 & -\bar{\alpha} & 0 \\ 0 & 1+\frac{\alpha\bar{\alpha}}{2} & 0 & -\alpha \\ \alpha & 0 & 1-\frac{\alpha\bar{\alpha}}{2} & 0 \\ 0 & -\bar{\alpha} & 0 & 1-\frac{\alpha\bar{\alpha}}{2} \end{pmatrix}, \tag{4.50}$$

and

$$g_B = \begin{pmatrix} 1-\frac{\beta\bar{\beta}}{2} & 0 & 0 & -\bar{\beta} \\ 0 & 1-\frac{\beta\bar{\beta}}{2} & \beta & 0 \\ 0 & -\bar{\beta} & 1+\frac{\beta\bar{\beta}}{2} & 0 \\ -\beta & 0 & 0 & 1+\frac{\beta\bar{\beta}}{2} \end{pmatrix}, \tag{4.51}$$

where the parameters α and β are complex Grassmann numbers.

The most general transformation can be obtained by the composition of the three transformations above:

$$g = g_E g_A g_B, \tag{4.52}$$

which satisfies the condition $g^\dagger \gamma_0 g = \gamma_0$, as required.

4.4.2 Time reversal and charge conjugation

Now we analyze the linear dependence of the particle and hole components of the spinor Ψ_σ, showing that the spinors are also invariant under a transformation that combines time reversal and particle-hole transformation. For that we define:

$$[\Psi]_{\nu,\sigma} = \begin{pmatrix} f_{N/2} & f_{N/2-1} & \cdots & f_{-N/2+1} & f_{-N/2} \\ f^\dagger_{-N/2} & f^\dagger_{-N/2+1} & \cdots & -f^\dagger_{N/2-1} & -f^\dagger_{N/2} \\ b_{N/2} & b_{N/2-1} & \cdots & b_{-N/2+1} & b_{-N/2} \\ b^\dagger_{-N/2} & b^\dagger_{-N/2+1} & \cdots & -b^\dagger_{N/2-1} & -b^\dagger_{N/2} \end{pmatrix}, \tag{4.53}$$

in such a away that the previously defined Ψ_σ are selected columns of this more general object. The first index ν is related to the particle/hole and bosonic/fermionic character of the operators and can assume values $\nu = \{1, 2, 3, 4\}$. Now we can write the spin as:

$$S_{\sigma\sigma'} = [\Psi^\dagger]_{\sigma,\nu}[\gamma_0]_{\nu\nu'}[\Psi]_{\nu',\sigma'}, \tag{4.54}$$

with the sum over ν, ν' implied. The time reversal operation transforms $[\Psi]_{\nu,\sigma}$ as:

$$\mathcal{T}([\Psi]_{\nu,\sigma}) = \tilde{\sigma}[\Psi^*]_{\nu,-\sigma}, \tag{4.55}$$

or in matrix form:

$$\mathcal{T} = \mathcal{I}_2 \otimes (i\tau_2), \tag{4.56}$$

where $\mathcal{I}_n$ is the $n \times n$ identity matrix and τ_2 the second Pauli matrix.

Charge conjugation transformation acts as:

$$C([\Psi]_{\nu,\sigma}) = \tilde{\nu}[\Psi]_{-\nu,\sigma}, \tag{4.57}$$

where $\tilde{\nu} = \pm 1$ for ν even and odd, respectively. Here $-\nu$ corresponds to $\{2, 1, 4, 3\}$ for

$\nu = \{1, 2, 3, 4\}$. In matrix form:

$$C = \mathcal{I}_2 \otimes (-i\sigma_2), \tag{4.58}$$

where σ_2 is again the second Pauli matrix.

The composition of these transformations leads to:

$$C\mathcal{T}([\Psi]_{\nu,\sigma}) = \tilde{\nu}\tilde{\sigma}[\Psi^*]_{-\nu,-\sigma} = [\Psi]_{\nu,\sigma}, \tag{4.59}$$

or

$$C\mathcal{T} = [\mathcal{I}_2 \otimes (-i\sigma_2)][\mathcal{I}_2 \otimes (i\tau_2)] = \mathcal{I}_4. \tag{4.60}$$

This shows that $[\Psi]_{\nu,\sigma}$ has an extra internal symmetry, and as a consequence the unitary transformation of the spinors introduced above should be in accordance with this symmetry as well. This requirement introduces the condition:

$$[U, C\mathcal{T}] = 0. \tag{4.61}$$

In order to proceed with the analysis we redefine the time-reversal operation as complex conjugation, represented by the operator K, times an antisymmetric matrix:

$$\mathcal{T}([\Psi]_{\nu\sigma}) = TK([\Psi]_{\nu\sigma}) = T([\Psi^*]_{\nu\sigma}), \tag{4.62}$$

where:

$$T = (-i\tau_2) \otimes D_{N/2}, \tag{4.63}$$

where $D_{N/2}$ is the $N/2 \times N/2$ anti-diagonal matrix with entries equal to one. Note that in this form T acts only on the spin indexes, in this case by a multiplication through the left.

Noticing now that the unitary transformation U is spin independent, it commutes with

the matrix $\mathcal{T}$ and the condition given by Eq. 4.61 becomes:

$$U^T C U = C, \tag{4.64}$$

what introduces an extra symplectic condition to the unitary transformations.

4.4.3 The Casimir

To uniquely characterize an irreducible representation of SP(N), in principle one needs to define $r = N/2-1$ invariants, or Casimirs, where r is the rank of the group (the dimension of the Cartan sub-algebra). In terms of Young diagrams, one can understand these parameters as the number of boxes in each row of the diagram (the maximum number of rows in the Young diagram for SP(N) is N/2). In this work we are only considering L-shaped diagrams, so we have the extra information that all the rows below the first one have only a single

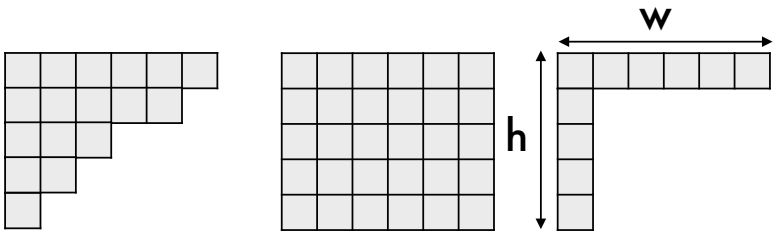

Figure 4.3: L-shape Young diagram and the parameters that characterize it: the width w and the height h.

From [131] we can deduce that for an L-shaped representation in SP(N) the second Casimir can be written in terms of the width w of the first row and the height h of the column in the diagram as:

$$C_2 = 2(w+h)(N+w-h) + 4h - 2 - 4N, \tag{4.65}$$

and identifying $Q = w + h - 1$ and $Y = h - w$, we have

$$C_2 = 2Q(N + 1 - Y), \tag{4.66}$$

see details in Appendix B. Now the two characteristic quantities are Q and Y, relative to the total number of boxes and the asymmetry of the representation, respectively.

Now we relate the magnitude of the spin $\mathbf{S}^2$ in terms of operators with the Casimir computed above. We start computing:

$$\mathbf{S}^2 = \sum_{\alpha\beta} S_{\alpha\beta} S_{\beta\alpha}, \tag{4.67}$$

whith $S_{\alpha\beta}$ is defined in Eq. 4.40. Taking the operator products and relabeling the summed indexes we find:

$$\begin{aligned} \mathbf{S}^2 &= \sum_{\alpha\beta} 2 \Big(f^\dagger_\alpha f_\beta f^\dagger_\beta f_\alpha + b^\dagger_\alpha b_\beta b^\dagger_\beta b_\alpha - \tilde{\alpha}\tilde{\beta} f^\dagger_\alpha f_\beta f^\dagger_{-\alpha} f_{-\beta} - \tilde{\alpha}\tilde{\beta} b^\dagger_\alpha b_\beta b^\dagger_{-\alpha} b_{-\beta} \\ &+ 2 f^\dagger_\alpha f_\beta b^\dagger_\beta b_\alpha - 2\tilde{\alpha}\tilde{\beta} f^\dagger_\alpha f_\beta b^\dagger_{-\alpha} b_{-\beta} \Big). \end{aligned} \tag{4.68}$$

Using the bosonic commutation and fermionic anticommutation relations we can identify the sum of operators with the definitions in Eq. 4.44:

$$\mathbf{S}^2 = 2 \left[N\hat{n}_F - \hat{n}_F^2 + N\hat{n}_B + \hat{n}_B^2 - \hat{\psi}^\dagger\hat{\psi} + 2\hat{\theta}^\dagger\hat{\theta} - 2\hat{\eta}^\dagger\hat{\eta} \right], \tag{4.69}$$

which can be rearranged as

$$\mathbf{S}^2 = 2 \left[(\hat{n}_B + \hat{n}_F)(N + 1 + \hat{n}_B - \hat{n}_F) - \hat{\psi}^\dagger\hat{\psi} - [\hat{\theta}, \hat{\theta}^\dagger] - 2\hat{\eta}^\dagger\hat{\eta} \right], \tag{4.70}$$

so we can identify:

$$\mathbf{S}^2 = 2\hat{Q}(N + 1 - \hat{Y}), \tag{4.71}$$

where

$$\hat{Q} = \hat{n}_F + \hat{n}_B, \tag{4.72}$$

$$\hat{Y} = \hat{n}_F - \hat{n}_B + \frac{\hat{\psi}^\dagger\hat{\psi} + [\hat{\theta}, \hat{\theta}^\dagger] + 2\hat{\eta}^\dagger\hat{\eta}}{\hat{Q}}, \tag{4.73}$$

so we can identify the operators $\hat{Q}$ and $\hat{Y}$ as operators that measure the parameters of the Young diagram, and that therefore fully characterize the representation.

We can also write $\mathbf{S}\cdot\mathbf{S}$ in terms of the redefined generators of the group:

$$\mathbf{S}\cdot\mathbf{S} = \Psi_0^2 - \mathbf{\Psi}\cdot\mathbf{\Psi} + \frac{i}{2}\mathbf{X}.\cdot\mathbf{M}\cdot\mathbf{X}, \tag{4.74}$$

where we introduced the vectors $\mathbf{\Psi} = (\Psi_1, \Psi_2, \Psi_3)$ and $\mathbf{X} = (A_1, A_2, B_1, B_2)$ and the matrix

$$\mathbf{M} = \begin{pmatrix} 0 & -1 & 0 & 0 \\ 1 & 0 & 0 & 0 \\ 0 & 0 & 0 & 1 \\ 0 & 0 & -1 & 0 \end{pmatrix}. \tag{4.75}$$

From this form, the constraint can be understood as the condition defining a super-surface in an 8-dimensional space with directions referent to each generator, subject to a complex measure $\mathbf{\Lambda}$ which can be inferred from the form above:

$$\mathbf{S}\cdot\mathbf{S} = \mathbf{V}_S\cdot\mathbf{\Lambda}\cdot\mathbf{V}_S, \tag{4.76}$$

where $\mathbf{V}_S = (\Psi_0, \Psi_1, \Psi_2, \Psi_3, A_1, A_2, B_1, B_2)$ and

$$\mathbf{\Lambda} = \begin{pmatrix} \gamma_1 & 0 \\ 0 & \mathbf{M} \end{pmatrix}, \tag{4.77}$$

with $\gamma_1 = diag[1, -1, -1, -1]$.

Further discussion on the Casimir and how it will be implemented in the large-N approach are points addressed in the next chapter and Appendix C.

Chapter 5

Applications of the Supersymmetric Symplectic Spins

In this chapter we apply the supersymmetric symplectic spins to two minimal models which allow us to make a parallel with the physics of heavy fermions. Our new approach allows us to explore different L-shaped representations and to determine which representation is more favorable in different regions in parameter space. We start exploring a two-impurity model that includes a Kondo coupling between the impurities and their respective bath of electrons and a Heisenberg coupling between them. We also study a three-impurity model that introduces the concept of geometrical frustration. We find promising results towards an unified description of the heavy fermion global phase diagram and a microscopic understanding of the two-fluid picture.

5.1 The need for a new approach to study heavy fermions

Heavy fermion systems are composed of a lattice of magnetic moments from electrons in f-orbitals, and a conduction sea originated from lighter bands of electrons [20, 32]. These systems have a very rich phase diagram due to the interplay of two energy scales originated from the Kondo coupling J_K:

$$T_K \sim De^{-1/N(0)J_K}, \qquad T_{RKKY} \sim N(0)J_K^2, \tag{5.1}$$

where $N(0) \sim 1/D$ is the density of states of the conduction electrons at the Fermi energy and D the bandwidth. While the Kondo temperature, T_K, sets the energy scale for the onset of the Kondo effect and consequently the formation of a coherent heavy Fermi liquid, the RKKY temperature defines the energy scale for the onset of magnetic order.

This family of materials is a great playground for the study of quantum criticality [26, 46];

they are characterized by relatively small energy scales, which allow experimentalists to explore their phase diagram as a function of pressure, magnetic field or doping. Tuning the system by one of these external parameters usually supresses or induces magnetic order and superconductivity is usually found around the magnetic quantum critical point, above which, at finite temperatures, non Fermi liquid behavior is observed, usually characterized by:

$$\rho \propto T^{\alpha}, \qquad \gamma \propto \log T, \tag{5.2}$$

a power law temperature dependence of the resistivity with $\alpha < 2$ and a logarithmic temperature dependence of the specific heat coefficient (for a review on experimental results see [27]).

One of the central challenges of heavy fermion materials is to understand the mechanism by which magnetism develops within the heavy electron fluid. Traditionally, magnetism and heavy fermion behavior have been regarded as two mutually exclusive states, separated by a single quantum critical point. However, a variety of recent experiments suggest a richer state of affairs, in particular:

- $YbRh_2Si_2$ can be driven to a quantum critical point by the application of magnetic field, where both the Néel temperature and the Kondo energy scale appear to simultaneously vanish. However, when doped, these two energy scales appear to separate from one-another, indicating that the break-down of Fermi liquid behavior and the development of magnetism are not rigidly pinned together [132, 133, 134];

- In the 115 superconductor $CeRhIn_5$ there is evidence for a microscopic and homogenious coexistence of local moment magnetism and superconductivity under pressure [6];

- The spontaneous development of inhomogenious Kondo states with partial magnetic order in the geometrically frustrated CePdAl [135, 136], in which one third of the Ce moments undergo a Kondo effect, while the other two thirds magnetically order [67].

Several phenomenological frameworks were proposed for the understanding of heavy fermion systems. The classical framework proposed in the 70's by Doniach [44], consists in the competition between T_K and T_{RKKY} determining the ground state to be a heavy Fermi liquid or magnetically ordered. More recently a new axis was added to this picture, by the inclusion of geometric frustration or reduction of dimensionality [53, 54]. These two factors contribute towards the suppression of magnetism in a different way, if compared to the competition with the Kondo effect. Also, based on experiments in several families of heavy fermions, a phenomenological two-fluid picture was proposed by Nakatsuji and Pines, with predictive power on the ground state [60, 74].

Unfortunately these proposals do not give us information on the character of the transition between the heavy Fermi liquid and magnetic phases, and its theoretical description has been a challenge for several decades. Theoretical proposals based on a spin density wave description of the quantum critical point [49], Kondo breakdown [137], deconfined quantum criticality [50] and local quantum criticality [48] were suggested, but their results are not able to fully account for experimental observations.

5.1.1 Spin Representations in the Kondo Model

The minimal model for heavy fermion systems is given by a Kondo lattice Hamiltonian:

$$H_{KL} = \sum_{\mathbf{k}\sigma} \epsilon_{\mathbf{k}} c^{\dagger}_{\mathbf{k}\sigma} c_{\mathbf{k}\sigma} + J_K \sum_i \mathbf{S}_j \cdot \mathbf{s}_j, \tag{5.3}$$

where the first term describes a conduction band of electrons with dispersion $\epsilon_{\mathbf{k}}$, J_K is the antiferromagnetic Kondo coupling between the local moment $\mathbf{S}_j$ and the spin of the conduction electron $\mathbf{s}_j$ at site j. The local moments present in these systems are neutral entities that have completely lost their charge degree of freedom and are hence uniquely characterized by their spin quantum numbers.

The removal of the charge degrees of freedom from the Hilbert space of the localized f-electrons implies that spin operators do not follow canonical commutation relations; consequently, their treatment within a path integral or diagrammatic approach is complicated by the absence of a Wick's theorem for spin operators. To circumvent this difficulty, the

spin operator is traditionally factorized in terms of creation and annihilation operators:

$$S_{\sigma\sigma'} = a^{\dagger}_{\sigma} a_{\sigma'}, \tag{5.4}$$

where the a_σ can be either a boson or a fermion operator, and the index $\sigma = \{1, 2\}$ for an $SU(2)$ spin. There are actually several spin representations one can choose from: the Holstein-Primakoff [88], the Schwinger boson [111], the Abrikosov pseudo-fermion [84] and drone or Majorana fermion [118] representations, among others.

The physics that each of these representations properly accounts for varies widely. For example, the antiferromagnetic (AFM) phase is well described by a Schwinger boson representation of the local moments, with the condensation of the bosons corresponding to the onset of magnetic order [138, 139]. By contrast, the heavy Fermi liquid phase is successfully understood in terms of a fermionic representation of the spin, forming a singlet state with the conduction electrons [140]. While these two examples successfully describe different extremes of the heavy fermion phase diagram, there is no theory that is able to account the most interesting region in the vicinity of the magnetic quantum critical point.

In this paper, we argue that to fully describe heavy fermion systems one needs to build an approach that allows the character of the spins to flow along the phase diagram. This need calls for the use of a supersymmetric representation of the spin:

$$S_{\sigma\sigma'} = f^{\dagger}_{\sigma} f_{\sigma'} + b^{\dagger}_{\sigma} b_{\sigma'}, \tag{5.5}$$

a combination of the previously proposed bosonic and fermionic representations, where $f^{\dagger}_{\sigma}$, f_σ are fermionic and $b^{\dagger}_{\sigma}$, b_σ bosonic creation and annihilation operators.

One of the difficulties which arise once spin operators are factorized in terms of creation and annihilation operators is that one must introduce projection operators or constraints to guarantee that the solution lies within the correct Hilbert space. In terms of wave functions we now have:

$$|\Psi\rangle = P_G |\Psi_F\rangle |\Psi_B\rangle, \tag{5.6}$$

where $|\Psi_F\rangle$ is the fermionic part of the wave function which describes the formation of singlets with the conduction electron spins, and $|\Psi_B\rangle$ is the bosonic part of the wave function which describes the formation of magnetic bonds. P_G is a Gutzwiller projection operator which keeps the system in the physical constrained Hilbert space and can be written as:

$$P_G = \int \Pi_j \frac{d\theta_j}{2\pi} e^{i\theta_j(n_B+n_F-1)}, \tag{5.7}$$

effectively imposing the condition $n_B + n_F = 1$ for an $SU(2)$ spin-1/2, and entangling the fermionic and bosonic character of the spin at each site.

These two components of the wave function behave as two complimentary fluids which can give rise to magnetism and heavy Fermi liquid behaviors and potentially provides a microscopic description of the phenomenological two-fluid picture.

5.1.2 Large-N Approch

The absence of a small energy scale in the Kondo model does not allow one to apply perturbative methods in the interaction. The alternative approach, followed here, is the use of a large N expansion in which the Kondo lattice model is generalized to a family of models in which the fundamental spin has N components, introducing the artificial small parameter $1/N$ in the large-N limit. The simplest generalization takes $SU(2)$ to $SU(N)$[141, 140, 142, 143, 144]:

$$S^{SU(N)}_{\sigma\sigma'} = f^\dagger_\sigma f_{\sigma'} + b^\dagger_\sigma b_{\sigma'}, \tag{5.8}$$

where now $\sigma = \{1, ..., N\}$. However, in this paper we choose the generalization to the symplectic subgroup $SP(N)$ [112, 123, 145]:

$$S^{SP(N)}_{\sigma\sigma'} = f^\dagger_\sigma f_{\sigma'} - \tilde{\sigma}\tilde{\sigma}' f^\dagger_{-\sigma'} f_{-\sigma} + b^\dagger_\sigma b_{\sigma'} - \tilde{\sigma}\tilde{\sigma}' b^\dagger_{-\sigma'} b_{-\sigma}, \tag{5.9}$$

where $\sigma = \{-N/2, ...N/2\}$, which we believe provides the most appropriate large-N treatment. In this second generalization all spin components explicitly invert under time reversal and it allows the development of mean field theories which incorporate magnetism and superconductivity, in contrast to the $SU(N)$ generalization.

The concept of a supersymmetric spin was introduced in previous studies of impurity Kondo models [126, 127, 128, 129]. In the work presented here, we follow the lines of [129], now with the generalization to $SP(N)$, and discuss the spin representations in terms of Young tableaus. Young tableaus provide a pictorial way to label different representations: horizontal Young tableaus label completely symmetric representations, which are naturally described by bosons, while vertical Young tableaus label completely antisymmetric representations, usually described by fermions. In case of supersymmetric representations we consider the set of representations characterized by L-shaped Young tableaux that arise once one combines the Schwinger boson and Abrikosov fermion spin representations. These representations are characterized by two constants:

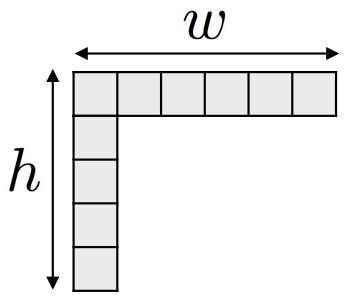

- the total number of elementary spins (or boxes) in the representation $Q = h + w - 1$, where h and w are height, and width of the Young tableau, respectively, and

- the asymmetry $Y = h - w$ of the L-shaped Young tableau, as in [129].

The asymmetry of the representation is absent in a physical $SU(2)$ spin-1/2, in which case the Young tableau is depicted by a single box, but once we enlarge the symmetry group of the spin in order to develop a large-N theory, we find a family of representations that range from a completely symmetric representation, fully described by bosons, to a completely antisymmetric representation, described only by fermions, including a whole plethora of

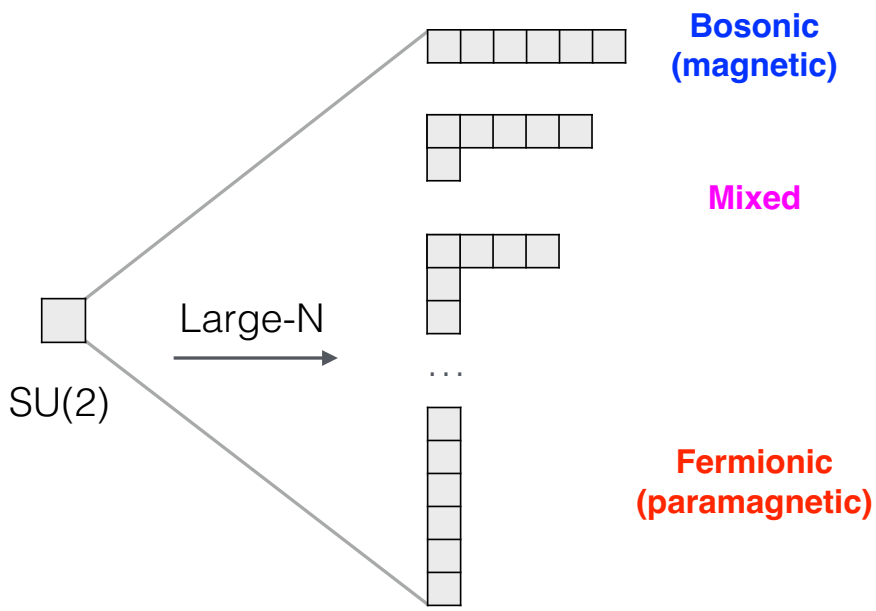

Figure 5.1: Series of Young tableaux in the large-N limit ranging from a fully symmetric (top) towards a fully antisymmetric (bottom), passing through a series of L-shape representations.

intermediate representations that we refer to as *mixed representations*, depicted by L-shaped Young tableaux (see Fig. 5.1). The possibility of mean-field solutions described by mixed representations is interesting as it may permit the description of new states of matter, including coexistence of magnetism, superconductivity and heavy Fermi liquid phases.

For a given value of N, one needs to decide which representation to choose in order to proceed with the calculations. Traditionally a purely bosonic representation or a purely fermionic representation is chosen, but the supersymmetric approach provides the possibility of considering an L-shaped representation. To constrain the problem to such a representation one must fix the values of $\hat{Q} = Q_0$ and $\hat{Y} = Y_0$ through the introduction of projection operators into the partition function:

$$Z = Tr[P_{Q_0,Y_0} e^{-\beta H}]. \tag{5.10}$$

Typically, the more negative Y, the more symmetric the spin representation and the

more magnetic the resulting ground-state whereas the more positive Y, the more antisymmetric the spin representation and the more Fermi-liquid like the ground-state. To avoid biasing the physics, we consider a grand-canonical ensemble of representations defined by the partition function with indefinite asymmetry Y,

$$Z = Tr[P_{Q_0} e^{-\beta H}] = \sum_{Y_0} Tr[P_{Q_0,Y_0} e^{-\beta H}], \tag{5.11}$$

where now we can identify P_{Q_0} with the large-N generalization of the Gutzwiller projection operator introduced in Eq. 5.7:

$$P_G \Rightarrow P_{Q_0} = \int \Pi_j \frac{d\theta_j}{2\pi} e^{i\theta_j (n_B + n_F - Q_0)}. \tag{5.12}$$

This procedure will enable the ensemble to explore the lowest energy configurations. Another motivation to work with the constraint that fixes only the total number of boxes of the representation is the fact that the asymmetry of the representation appears only in the large-N limit, so by letting Y run free provides an unbiased way to take the limit $N \to 2$ (see Fig. 5.1).

5.1.3 New features of this work

The large-N limit we now develop places all L-shaped representations with a given number of boxes on the same footing, and the asymmetry of the representation can be thought of as a variational parameter. The character the representation (bosonic, fermionic or mixed) will now be decided by the energetics of the problem. This will permit us to completely explore the phase diagram of systems as heavy fermions, in which the character of the spin changes from fermionic in the HFL phase towards bosonic in the AFM region.

Fig. 5.2 illustrates schematically the evolution of the energy landscape as a function of q_F, the number of fermions in the representation, for three different values of T_K/T_{RKKY}. For small T_K/T_{RKKY} the energy landscape has a minima for $q_F = 0$, what means that the system prefers to have a bosonic spin representation and possibly develops magnetic order. Analogously, for large T_K/T_{RKKY}, the energy landscape has a minimum for the maximum

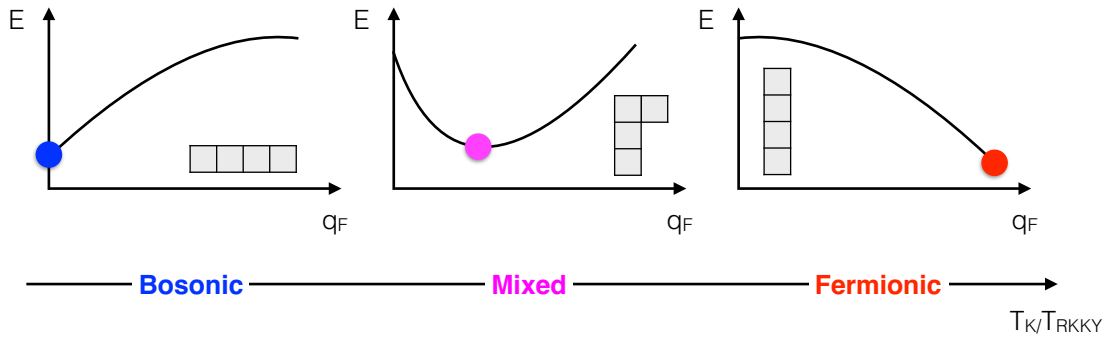

Figure 5.2: Schematic representation of the evolution of the energy landscape as a function of q_F for different values of the ratio T_K/T_{RKKY}.

possible value of q_F, indicating a purely fermionic representation, what would possibly lead to the development of a heavy Fermi liquid. For intermediate values of T_K/T_{RKKY} we find that the representation is actually mixed since the energy minima happens for an intermediate value of q_F, and that the minima is a saddle point as a function of q_F. Here we highlight the different nature of the minima by labeling:

- Type I minima: For this kind of minima there is no saddle point for the free energy as a function of the representation and the minima occurs for purely bosonic or purely fermionic representations, indicating that the original supersymmetry of the spin is severely broken. In this case the results of a purely bosonic or fermionic representations are recovered;

- Type II minima: This kind of minima is in fact a saddle point of the free energy as a function of the representation and happens when mixed representations are energetically favorable. This minima potentially represents a new phase of matter, in which bosons and fermions coexist, naturally bringing the idea of a two fluid-picture. Apparently, associated with this saddle point there will be a *goldstino*, a fermionic zero mode, related to a partial restoration of supersymmetry coming from the fact that the corner box in the Young tableaux can be either represented by a boson or a fermion, and in this case we say that supersymmetry is only weakly broken.

Other new features of this work are:

- Symplectic Spins: we generalize the rotation group of the spin from $SU(2)$ to $SP(N)$ for a large-N treatment [123, 145]. This generalization guarantees that all the components of the generalized spin properly invert under time reversal and also brings in some advantages. First, it allows the description of geometrically frustrated magnetism; one can use the same spin representation in every site of a lattice and be able to form singlets between those [112], which is not possible within an $SU(N)$ generalization, in which case one is restricted to treat only bipartite lattices with conjugate representations in different sub-lattices [144]. Second, it naturally introduces superconductivity into the problem since now one can also decouple the four-body terms in the particle-particle channel;

- Inhomogeneous representation: We explore the possibility of solutions with different spin representations in different sites. This is motivated by the partially ordered phase verified experimentally in CePdAl. Fig. 5.3 represents this kind of solution schematically in a frustrated triangular geometry: one of the local moments in the

from the

sentation,

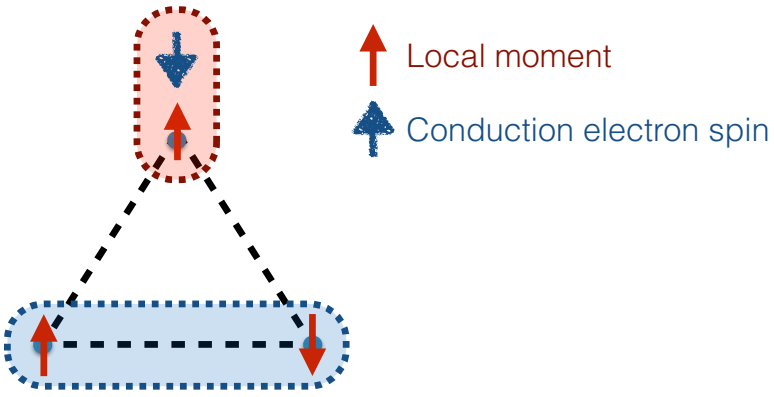

Figure 5.3: Schematic representation of the inhomogeneous solution for the frustrated triangular geometry.

5.2 The formalism

Starting with the Kondo Lattice Model, including now a Heisenberg exchange between nearest neighbors:

$$H = H_c + J_K \sum_j S_{\sigma\sigma'}(j) s_{\sigma'\sigma}(j) + J_H \sum_{\langle jj' \rangle} S_{\sigma\sigma'}(j) S_{\sigma'\sigma}(j'), \tag{5.13}$$

with an implied sum over σ and σ'. The first term is the conduction electron Hamiltonian $H_c = \sum_{\mathbf{k}\sigma} \epsilon_{\mathbf{k}} c^\dagger_{\mathbf{k}\sigma} c_{\mathbf{k}\sigma}$ for electrons with dispersion $\epsilon_{\mathbf{k}}$, where $c^\dagger_{\mathbf{k}\sigma}$, $c_{\mathbf{k}\sigma}$ are creation and annihilation operators of electrons with momentum $\mathbf{k}$ and spin σ. $s(j)$ is the spin density of conduction electrons at site j and $S(j)$ is the local moment spin at the same site. Introducing the supersymmetric-symplectic spin, the Hamiltonian can be written in the large-N limit in terms of fermionic and bosonic operators as:

$$H = H_c - \frac{J_K}{N} \sum_j c_{j\sigma} \bar{\Psi}_{j\sigma} \Psi_{j\sigma'} c^\dagger_{j\sigma'} + \frac{J_H}{2N} \sum_{\langle jj' \rangle} \bar{\Psi}_{j\sigma} \Psi_{j\sigma'} \bar{\Psi}_{j'\sigma'} \Psi_{j'\sigma}, \tag{5.14}$$

with $\bar{\Psi}_\sigma = \Psi^\dagger_\sigma \gamma_0$, as defined in Eq. 4.42. Note that the Hamiltonian is invariant under any transformation $\Psi_{a\sigma} \to g\Psi_{a\sigma}$ that satisfies $g^\dagger \gamma_0 g = \gamma_0$. For explicit form of the transformations g we refer the reader to the previous chapter.

The constraint fixing the total number of bosons plus fermions at each site $n_{Fj} + n_{Bj} = Q_0$ can also be written in terms of the spinors $\Psi_{j\sigma}$:

$$n_{Fj} + n_{Bj} = \frac{1}{2} \sum_\sigma \bar{\Psi}_{j\sigma} \Lambda \Psi_{j\sigma}, \tag{5.15}$$

where

$$\Lambda = \begin{pmatrix} 1 & 0 & 0 & 0 \\ 0 & -1 & 0 & 0 \\ 0 & 0 & 1 & 0 \\ 0 & 0 & 0 & -1 \end{pmatrix}. \tag{5.16}$$

We can now write the partition function as a functional integral, already introducing

the constraint in the form above by the means of the Lagrange multiplayer λ_j for each site:

$$Z = \int \mathcal{D}\mu e^{-S}, \qquad \mathcal{D}\mu = \mathcal{D}[c, f, b, \lambda], \tag{5.17}$$

where

$$S = S_c + S_S + S_K + S_H. \tag{5.18}$$

The components of the action are:

$$S_c = \int_0^\beta d\tau \sum_{\mathbf{k}\sigma} c^\dagger_{\mathbf{k}\sigma}(\partial_\tau + \epsilon_{\mathbf{k}}) c_{\mathbf{k}\sigma}, \tag{5.19}$$

the conduction electron part of the action,

$$S_S = \int_0^\beta d\tau \sum_j \left(\sum_\sigma \bar{\Psi}_{j\sigma} \frac{(\partial_\tau + \Lambda_j)}{2} \Psi_{j\sigma} - \lambda_j Q_0 \right), \tag{5.20}$$

describes the Berry phase and constraint associated with the localized spins, by the introduction of the Lagrange multiplier λ_j, where $\Lambda_j = \lambda_j \Lambda$,

$$S_K = -\frac{J_K}{N} \sum_j c_{j\sigma} \bar{\Psi}_{j\sigma} \Psi_{j\sigma'} c^\dagger_{j\sigma'}, \tag{5.21}$$

is the Kondo term and

$$S_H = \frac{J_H}{2N} \sum_{\langle jj' \rangle} \bar{\Psi}_{j\sigma} \Psi_{j\sigma'} \bar{\Psi}_{j'\sigma'} \Psi_{j'\sigma}, \tag{5.22}$$

the Heisenberg term in the action.

The components S_K and S_H include interacting terms that we decouple by Hubbard-Stratonovich transformations. The Kondo term decouples as:

$$S_K \to \tilde{S}_K = \int_0^\beta d\tau \sum_j \left[\sum_\sigma \left(\bar{\Psi}_{j\sigma} V_j c_{j\sigma} + h.c. \right) + \frac{N}{J_K} V_j^\dagger \gamma_0 V_j \right], \tag{5.23}$$

where the Hubbard-Stratonovich fields are organized in the matrixes:

$$V_j = \begin{pmatrix} v_j \\ \bar{d}_j \\ -\phi_j \\ \bar{\xi}_j \end{pmatrix}. \tag{5.24}$$

Here v_j and d_j are complex fields related to the hybridization between f-fermions and c-electrons and the development of superconductivity by the formation of pairs between f-fermions and c-electrons, respectuvely. The parameters ϕ_j and ξ_j are complex Grassmann numbers, the first related to the hybridization between b-bosons and c-electrons and the second related to the development os pairs formed between b-bosons and c-fermions.

The Heisenberg term decouples as:

$$S_H \to \tilde{S}_H = \int_0^\beta d\tau \left[\frac{1}{2} \sum_{\langle jj' \rangle} \bar{\Psi}_{j\sigma} \Delta_{jj'} \gamma_0 \Psi_{j'\sigma} + \frac{N}{4J_H} \sum_{\langle jj' \rangle} STr(\Delta^\dagger_{jj'} \gamma_0 \Delta_{jj'} \gamma_0) \right], \tag{5.25}$$

where STr is the super-trace defined as $STr(A) = A_{11} + A_{22} - A_{33} - A_{44}$. The Hubbard-Stratonovich fields are now:

$$\Delta_{jj'} = \begin{pmatrix} \Delta_{Fjj'} & \Delta_{Sjj'} \\ \Delta_{Sj'j} & \Delta_{Bjj'} \end{pmatrix}, \tag{5.26}$$

where

$$\Delta_{Fjj'} = \begin{pmatrix} p_{jj'} & t_{jj'} \\ \bar{t}_{jj'} & -\bar{p}_{jj'} \end{pmatrix}, \tag{5.27}$$

$$\Delta_{Bjj'} = \begin{pmatrix} q_{jj'} & -g_{jj'} \\ \bar{g}_{jj'} & \bar{q}_{jj'} \end{pmatrix}, \tag{5.28}$$

$$\Delta_{Sjj'} = \begin{pmatrix} -\gamma_{jj'} & -\mu_{jj'} \\ \bar{\mu}_{jj'} & -\bar{\gamma}_{jj'} \end{pmatrix}. \tag{5.29}$$

Here the complex fields $p_{jj'}$ and $t_{jj'}$ promote hopping and pairing amongst the f-fermions in different sites and the complex fields $q_{jj'}$ and $g_{jj'}$ promote hopping and magnetic bond formation between the b-bosons. The Grassmannian parameters $\gamma_{jj'}$ and $\mu_{jj'}$ are related to a kind of hopping which transmutes bosons into fermions and vice-versa and pairing between bosons and fermions in different sites, respectively.

The partition function now reads:

$$Z = \int \mathcal{D}\mu^* e^{-\tilde{S}}, \qquad \mathcal{D}\mu^* = \mathcal{D}\mu\mathcal{D}[V,\Delta], \tag{5.30}$$

where

$$\tilde{S} = S_c + S_S + \tilde{S}_K + \tilde{S}_H, \tag{5.31}$$

and the integral over $\mathcal{D}[V,\Delta]$ indicates the integral over all the fluctuating fields introduced by the Hubbard-Stratonovich transformations. Here c-number fields are represented by the latin letters (v,d,p,t,q,g), while the Grassmannian fields are represented by the greek letters (ϕ,ξ,γ,μ). Grassmannian fields are introduced in order to decouple terms with fermionic bilinears. Note that the Kondo and Heisenberg parts of the action are invariant under the transformation $\Psi_{a\sigma} \to g\Psi_{a\sigma}$ if the fluctuating field matrices transform accordingly as $V_a \to gV_a$ and $\Delta = g\Delta g^\dagger$.

Now we move to the discussion of the implementation of constraint by fixing $\hat{Q} = Q_0$ (see also discussion in Appendix C). The constraint can be imposed as a projection operator in each site j, written as a delta function:

$$P_{Q_0} = \Pi_j P^j_{Q_0} = \Pi_j \delta(\hat{Q}_j - Q_0). \tag{5.32}$$

In order to treat the bosonic and fermionic components of the spin in the grand canonical

ensemble, we split the constraint into three terms as follows:

$$P^{j}_{Q_0} = \sum_{Q_{Fj},Q_{Bj}} \delta(\hat{n}_{Fj} - Q_{Fj})\delta(\hat{n}_{Bj} - Q_{Bj})\delta(Q_{Fj} + Q_{Bj} - Q_0). \tag{5.33}$$

The constraint fix the total number of bosons plus fermions equal to Q_0, leaving the exact representation (or asymmetry) undetermined. As discussed in the introductory section here the representation is in fact determined by the energetics of the problem.

This constraint can be implemented in the path integral as a Dirac delta function in its integral form:

$$P_{Q_0} = \int \mathcal{D}\lambda e^{-S_P}, \quad \mathcal{D}\lambda = \Pi_j d\lambda_j d\lambda_{Fj} d\lambda_{Bj}, \tag{5.34}$$

with

$$\begin{aligned} S_P &= \int_0^\beta d\tau \sum_j \left(\lambda_{Fj}(n_{Fj} - Q_{Fj}) + \lambda_{Bj}(n_{Bj} - Q_{Bj})\right. \\ &\qquad \left. +\lambda_j(Q_{Fj} + Q_{Bj} - Q_0)\right), \end{aligned} \tag{5.35}$$

where λ_j, λ_{Fj} and λ_{Bj} are integrated along the imaginary axis. Within these considerations S_S can be rewritten as:

$$\begin{aligned} S_S \to \tilde{S}_S &= \int_0^\beta d\tau \sum_j \left(\sum_\sigma \bar{\Psi}_{j\sigma} \frac{(\partial_\tau + \tilde{\Lambda}_j)}{2} \Psi_{j\sigma} \right. \\ &\qquad \left. -\lambda_{Fj}Q_{Fj} - \lambda_{Bj}Q_{Bj} - \lambda_j(Q_{Fj} + Q_{Bj} - Q_0) \right), \end{aligned} \tag{5.36}$$

where now

$$\tilde{\Lambda}_j = \begin{pmatrix} \lambda_{Fj} & 0 & 0 & 0 \\ 0 & -\lambda_{Fj} & 0 & 0 \\ 0 & 0 & \lambda_{Bj} & 0 \\ 0 & 0 & 0 & -\lambda_{Bj} \end{pmatrix}, \tag{5.37}$$

and the partition function is now written as: The partition function now reads:

$$Z = \int \mathcal{D}\mu^* D\lambda e^{-S'}, \tag{5.38}$$

where

$$S' = S_c + \tilde{S}_S + \tilde{S}_K + \tilde{S}_H, \tag{5.39}$$

Anticipating that we are interested in a static mean field solution, we can already drop the terms with fermionic bilinears (formed by a boson times a fermion). Fermionic operators are anti-periodic and bosonic operators are periodic in imaginary time with period β. As a consequence, the terms with fermionic bilinears do not contribute to the static mean field solution since the action should be periodic in imaginary time. For this kind of term to contribute the fluctuating fields introduced by the Hubbard-Stratonovich transformation should be anti-periodic in time, what would require them to be dynamic. As a conclusion the Grassmannian fields contribute just to the fluctuations, not to the static mean field solution, so we have:

$$V_j \to V_j^0 = \begin{pmatrix} v_j \\ \bar{d}_j \\ 0 \\ 0 \end{pmatrix}, \tag{5.40}$$

and

$$\Delta_{jj'} \to \Delta_{jj'}^0 = \begin{pmatrix} \Delta_{Fjj'} & 0 \\ 0 & \Delta_{Bjj'} \end{pmatrix}. \tag{5.41}$$

Note that the fermionic and bosonic parts of the action decouple since all the matrices in the action now have the off-diagonal blocks equal to zero. Now it is possible to solve the fermionic and bosonic problems separately, imposing the constraint $Q_{Fj} + Q_{Bj} = Q_0$ to the solution in the end of the calculation. Note that this provides a picture of two

asymptotically independent fluids, bosonic and fermionic, in the large-N limit and that the introduction of fluctuations will provide interactions between them.

Now, as a first exploration of this idea we illustrate the formalism with two simple examples: a two-impurity and a frustrated three-impurity model and show that there are stable mean field solutions with mixed representations, as well as with purely bosonic and purely fermi

5.3 A fir

As a first a
that allows
consists of t
and interact

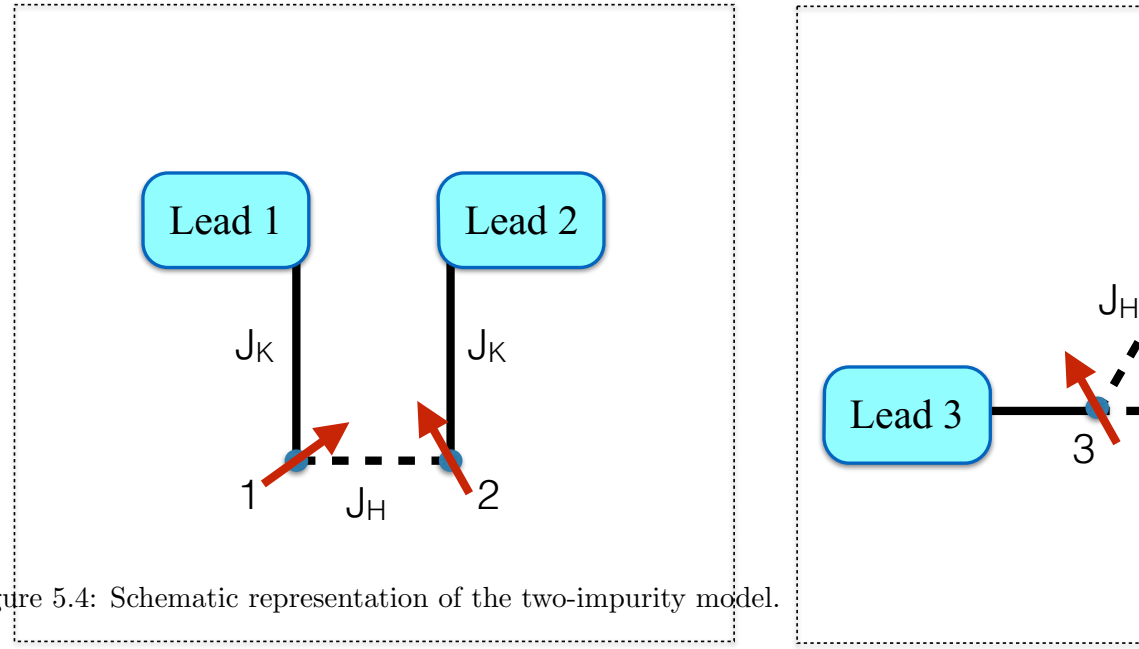

Figure 5.4: Schematic representation of the two-impurity model.

The Hamiltonian is written as:

$$H = H_c + J_K \sum_a s_{a\sigma\sigma'}(0) S_{a\sigma'\sigma} + J_H S_{1\sigma\sigma'} S_{2\sigma'\sigma}, \tag{5.42}$$

where $H_c = \sum_{a\mathbf{k}\sigma} \epsilon_{\mathbf{k}} c^\dagger_{a\mathbf{k}\sigma} c_{a\mathbf{k}\sigma}$ is the conduction electron Hamiltonian, $a = \{1, 2\}$ is the lead and local moment index, $\mathbf{k}$ the momentum and σ the spin index. Here $s_a(0)$ is the spin density of conduction electrons at the site that is connected to the local moment spin S_a. Introducing the supersymmetric-symplectic spin, the Hamiltonian can be written in the

large-N limit in terms of fermionic and bosonic operators as:

$$H = H_c - \frac{J_K}{N}\sum_{a\mathbf{k}\sigma\sigma'} c_{a\mathbf{k}\sigma}\bar{\Psi}_{a\sigma}\Psi_{a\sigma'}c^{\dagger}_{a\mathbf{k}\sigma'} + \frac{J_H}{2N}\sum_{\sigma\sigma'}\bar{\Psi}_{1\sigma}\Psi_{1\sigma'}\bar{\Psi}_{2\sigma'}\Psi_{2\sigma}, \tag{5.43}$$

where $\bar{\Psi}_\sigma = \Psi^\dagger_\sigma\gamma_0$, as defined in Eq. 4.42.

We can now apply the formalism introduced in the previous section. We perform a Hubbard-Stratonovich transformation in order to decouple the interacting terms in the Hamiltonian by introducing fluctuating fields. Within a static mean field solution the fermionic and bosonic problem decoupled and are effectively linked only by the constraint; we can now factor the partition function as:

$$Z = Z_0 Z_F Z_B, \tag{5.44}$$

where

$$Z_0 = \int d\lambda e^{-\beta N\lambda(q_F+q_B-q_0)} \tag{5.45}$$

guarantees that the constraint is satisfied when the free energy is minimized with respect to λ. Here we defined $q_{F,B,0} = Q_{F,B,0}/N$ and assumed the representation to be the same in both sites, so we drop the index a in λ and $q_{F,B,0}$.

5.3.1 The fermionic part of the solution

The fermionic part of the partition function reads:

$$Z_F = \int \mathcal{D}\mu_F e^{-S_F}, \quad \mathcal{D}\mu_F = \mathcal{D}[c, f, v, \lambda_F] \tag{5.46}$$

$$\begin{aligned} S_F &= S_c + \int_0^\infty \sum_{a\sigma}\left[f^\dagger_{a\sigma}(\partial_\tau + \lambda_F)f_{a\sigma} + \sum_{\mathbf{k}}\left(f^\dagger_{a\sigma}v_a c_{a\mathbf{k}\sigma} + h.c.\right)\right] \\ &\quad +\beta N\sum_a \frac{|v_a|^2}{J_K} - 2\beta N\lambda_F q_F, \end{aligned} \tag{5.47}$$

where we already dropped the terms in p_a and t_a, since it can be shown that these do not contribute to the saddle point solution. Also, the f-operators can be redefined to eliminate the pairing term between c- and f-operators from the Hamiltonian:

$$f_{a\sigma} \to \tilde{f}_{a\sigma} = \frac{\bar{v}_a f_{a\sigma} + d_a \tilde{\sigma} f^{\dagger}_{a-\sigma}}{\sqrt{|v_a|^2 + |d_a|^2}}. \tag{5.48}$$

Under these considerations, the fermionic part of the solution reduces to two decoupled impurity problems. Taking $v_a = v$ to be site independent and integrating out the conduction electrons in each lead and transforming from imaginary time to Matsubara frequencies (see details in Appendix D):

$$S_F = \sum_{na\sigma} f^{\dagger}_{a\sigma}(i\omega_n)(-i\omega_n + \lambda_F + i\Gamma_n) f_{a\sigma}(i\omega_n) + 2\beta \frac{N|v|^2}{J_K} - 2\beta N \lambda_F q_F, \tag{5.49}$$

with

$$\Gamma_n = \Gamma \Theta(D - |i\omega_n|) sgn(i\omega_n), \quad \Gamma = \pi \rho_0 |v|^2, \tag{5.50}$$

where ρ_0 is a constant DOS, D is the bandwidth and $\Theta(x)$ is a Heaviside step function. Summing over Matsubara frequencies, in the limit $T \to 0$, the free energy has the form:

$$\frac{F_F}{N} = \frac{2}{\pi} Im \left[\xi_F \ln \left(\frac{\xi_F}{e T_K e^{i\pi q_F}} \right) \right], \tag{5.51}$$

where we define

$$\xi_F = \lambda_F + i\Gamma, \tag{5.52}$$

and the Kondo temperature

$$T_K = D e^{-1/\rho_0 J_K}. \tag{5.53}$$

In the large-N limit the partition function is dominated by the saddle point. Minimizing

the free energy with respect to ξ_F one finds

$$\xi_F = T_K e^{i\pi q_F}, \tag{5.54}$$

and substituting back into the fermionic free energy:

$$\frac{F_F}{N} = -\frac{2}{\pi} T_K \sin(\pi q_F). \tag{5.55}$$

5.3.2 The bosonic part of the solution

The bosonic part of the partition function can be concisely written as:

$$Z_B = \int \mathcal{D}\mu_B e^{-S_B}, \quad \mathcal{D}\mu_B = \mathcal{D}[b, g, \lambda_B]$$

$$S_B = \int_0^\beta d\tau \sum_\sigma \Psi^\dagger_{B\sigma} L_B \Psi_{B\sigma} + \beta N \frac{|g|^2}{J_H} - 2\beta N \lambda_B (q_B + 1/2), \tag{5.56}$$

where

$$L_B = \begin{pmatrix} \partial_\tau + \lambda_B & g \\ \bar{g} & -\partial_\tau + \lambda_B \end{pmatrix}, \tag{5.57}$$

$$\Psi_{B\sigma} = \begin{pmatrix} b_{1\sigma} \\ \tilde{\sigma} b^\dagger_{2-\sigma} \end{pmatrix}. \tag{5.58}$$

Here we already dropped the fluctuating field q since the saddle point solution results in $q = 0$. Integrating out the bosons and summing over Matsubara frequencies (see Appendix E), in the zero temperature limit, the free energy is given by:

$$\frac{F_B}{N} = \sqrt{\lambda_B^2 - |g|^2} + \frac{|g|^2}{J_H} - 2\lambda_B (q_B + 1/2). \tag{5.59}$$

Minimizing the free energy with respect to g and λ_B one finds:

$$\lambda_B = J_H(q_B + 1/2), \qquad |g|^2 = J_H^2 q_B(q_B + 1), \tag{5.60}$$

so the the bosonic free energy can be written as:

$$\frac{F_B}{N} = -J_H(q_B + 1/2)^2, \tag{5.61}$$

up to a constant term.

5.3.3 Analysis of the free energy

The total free energy can be written, already making explicit use of the constraint condition $q_F + q_B = q_0$, as:

$$\frac{F}{J_H N} = -\frac{2}{\pi} A \sin(\pi q_F) - (q_0 - q_F + 1/2)^2, \tag{5.62}$$

where $A = \frac{T_K}{J_H}$ and the free energy is given in units of J_H. For each value of A and q_0 the representation was determined by the minimization of the free energy with respect to q_F and the result is plotted in Fig. 5.5. In case $q_F = q_0$ the phase is purely fermionic, meaning that a completely antisymmetric representation is favored. Analogously, for $q_F = 0$ (or $q_B = q_0$) the phase is purely bosonic, and a symmetric representation is more appropriate. Solutions with $0 < q_F < q_0$ are solutions in which both bosons and fermions coexist, what we call *mixed phase* and label as $F + B$ in Fig. 5.5. Note that for a fixed value of q_0, as the ratio T_K/J_H is increased the spins tend to develop fermionic character. Also, for a fixed value of T_K/J_H, increasing $1/q_0$ (or reducing q_0, what is equivalent to decreasing the magnitude of the spin) the spin representation also tends towards a fermionic representation (at least for $T_K/J_H > 1$).

The dashed line between F and $F+B$ regions indicates a second order "phase transition"

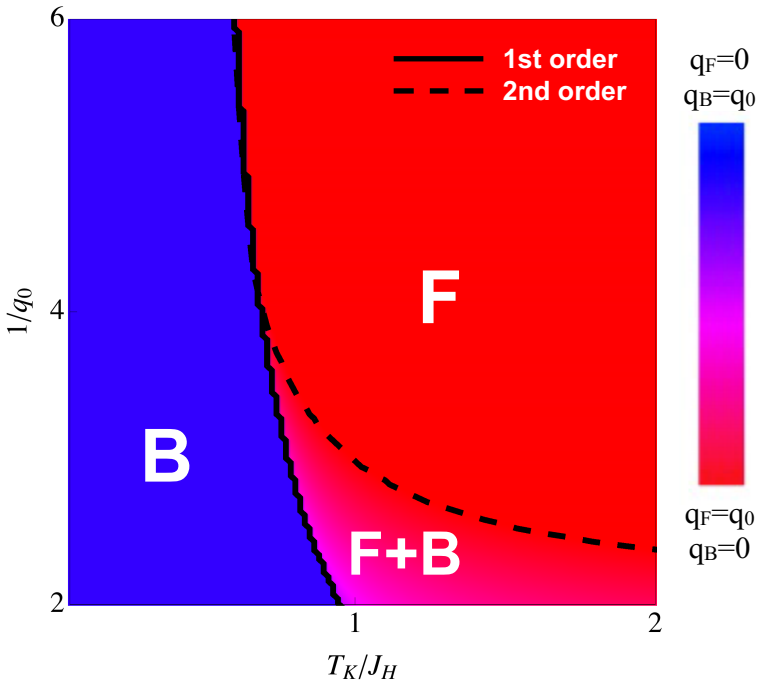

Figure 5.5: "Phase diagram" of the most favorable representations as a function of $A = \frac{T_K}{J_H}$ and $1/q_0$ for the two-impurity model. A purely fermionic representation phase (red) is labeled by F, a pure bosonic representation phase (blue) is labeled as B and the mixed representation phase (intermediate colors) is labeled by $F + B$.

and can be determined from the condition:

$$\frac{F[q_F = q_0]}{N} = \frac{F[q_F = q_0 - \delta]}{N}\bigg|_{\delta \to 0}, \tag{5.63}$$

which leads to:

$$A = \frac{1}{2Cos(\pi q_0)}. \tag{5.64}$$

The continuous line represents a first order "phase transition". The line between the purely fermionic and purely bosonic representations is determined by:

$$\frac{F[q_F = q_0]}{N} = \frac{F[q_F = 0]}{N}, \tag{5.65}$$

which gives the condition:

$$A = \frac{\pi q_0(q_0+1)}{2Sin(\pi q_0)}. \tag{5.66}$$

The first order line between the phases B and $F+B$ cannot be computed analytically and was determined numerically.

Throughout the mixed phase we have $\lambda_F = \lambda_B$, as if both fluids have the same chemical potential. This is related to the presence of the Type II minima of the free energy (see discussion in the introduction), with a saddle point that allows the coexistence of bosons and fermions and the interchange of one into another at no energy cost. In particular, at the second order "phase transition" line discussed above, when $q_F = q_0 - \delta$ and $q_B = \delta$ with $\delta \to 0$, one can check explicitly from Eq. 5.60 and 5.54 that the condition $\lambda_F = \lambda_B$ gives the same condition that defines the second order line in Eq. 5.64.

5.3.4 Fluctuations of the local fermionic fields

We now analyze the effects of fluctuations of the local fermionic fields. Further investigation on the effect of fluctuations are left for future work.

In Section 5.2 above we introduced the time dependent local fields ϕ_a and ξ_a, which allow us to decouple the terms $(b^\dagger_{a\sigma} c_{a\mathbf{k}\sigma})(c^\dagger_{a\mathbf{k}\sigma'} b_{a\sigma'})$ and $(\tilde{\sigma} b^\dagger_{a\sigma} c^\dagger_{a\mathbf{k}-\sigma})(\tilde{\sigma}' c_{a\mathbf{k}-\sigma'} b_{a\sigma'})$ in the action, respectively. These fields do not acquire an expectation value, but fluctuate around zero. The partition function can now be written in terms of the saddle point solution determined in the former subsection times $Z_{\phi,\xi}$, the new contributions to the partition function due to the presence of the fluctuating fields $\delta\phi$ and $\delta\xi$, that we take to be site independent. Focusing first in the $\delta\phi$ field:

$$Z_\phi = \int D\phi e^{-\int_0^\beta d\tau \left[\sum_{a\mathbf{k}\sigma}(b^\dagger_{a\sigma} c_{a\mathbf{k}\sigma}\delta\phi + h.c.) + \frac{2N|\delta\phi|^2}{J_K}\right]}. \tag{5.67}$$

Expanding up to second order in $\delta\phi$ we can identify the propagator for the fluctuating

field $\delta\phi$:

$$[D_\phi(i\omega_r)]^{-1} = 2N\left[\chi_{cb}(i\omega_r) - \frac{1}{J_K}\right], \tag{5.68}$$

where $\chi_{cb}(i\omega_r)$ can be identified with the following bubble diagram:

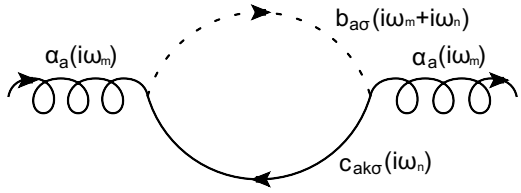

and written as:

$$\chi_{cb}(i\omega_r) = -\frac{1}{\beta}\sum_{\mathbf{k}\mathbf{k}'m} G_b(i\omega_r + i\omega_m)G_{\mathbf{k}\mathbf{k}'}(i\omega_m), \tag{5.69}$$

where $G_b(i\nu_n)$ is the bosonic propagator and $G_{\mathbf{k}\mathbf{k}'}(i\omega_n)$ is the full c-electron propagator. Details of the calculation of $\chi_{cb}(\omega)$ can be found in Appendix F.

One interesting region for the analysis of $D_\phi(i\omega_r)$ is the second order transition line, where the energy levels of the bosons and fermions are equal. In the infinite bandwidth limit we find:

$$\chi_{cb}(\omega - i\epsilon) - \frac{1}{J_K} = N(0)\omega Re\left[\frac{\log(\lambda + i\Delta)}{\omega + i\Delta}\right] - \frac{N(0)\omega^2}{\Delta^2 + \omega^2}\log(\lambda - \omega + i\epsilon). \tag{5.70}$$

Note that at zero frequency, $\chi_{cb}(0) - \frac{1}{J_K} = 0$, so $[D_\phi(0)]^{-1} = 0$, and the propagator for the fermionic hybridization field ϕ diverges at the second order phase transition, indicating the presence of a fermionic zero mode. Also, there is a gap of magnitude equal to $\lambda = \lambda_F = \lambda_B$ with a continuum which goes up to the bandwidth. This gap is always present in the 2-impurity model since $\lambda = \xi_B = J_H/2$ is aways finite at the transition. For a Kondo-Heisenberg model in the lattice, the bosonic level will acquire a dispersion and when magnetic order sets in it will be gapless at some points in the Brillouin zone. In that case the spectrum for the fermionic hybridization field is expected to have a continuum of excitations, which can potentially lead to non Fermi liquid behavior.

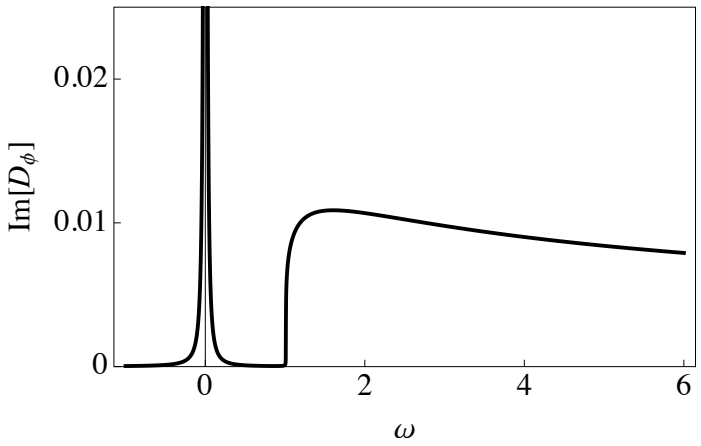

Figure 5.6: Plot of the imaginary part of the $\delta\phi$ propagator. The parameters used in this plot were a solution of the mean field theory at a specific point of the second order phase transition: $A = 1.57$ and $1/q_0 = 2.5$, what gives $\lambda_F = \lambda_B = \lambda = 1.01$ and $\Delta = 2.97$ (in units of J_H).

For the second fermionic mode $\delta\xi$ a similar calculation follows, where now:

$$[D_\xi(i\omega_r)]^{-1} = 2N\left[\bar{\chi}_{cb}(i\omega_r) - \frac{1}{J_K}\right], \tag{5.71}$$

where $\bar{\chi}_{cb}(i\omega_r)$ can be identified with the following bubble diagram:

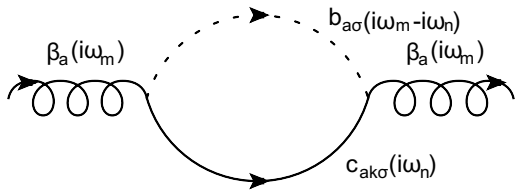

and written as:

$$\bar{\chi}_{cb}(i\omega_r) = \frac{1}{\beta}\sum_{\mathbf{k}\mathbf{k}'m} G_b(i\omega_r - i\omega_m)G_{\mathbf{k}\mathbf{k}'}(i\omega_m). \tag{5.72}$$

In an analogous fashion we find:

$$\begin{aligned}\bar{\chi}_{cb}(\omega - i\epsilon) - \frac{1}{J_K} &= N(0)(\omega - 2\lambda)Re\left[\frac{\log(-\lambda + i\Delta)}{\omega - 2\lambda + i\Delta}\right] \\ &- \frac{N(0)(\omega - 2\lambda)^2}{\Delta^2 + (\omega - 2\lambda)^2}\log(\lambda - \omega + i\epsilon).\end{aligned} \tag{5.73}$$

Here we note that there is no zero mode for this fermionic field at the transition, and a continuum starts at a finite $\lambda = \xi_B = J_H/2$. In the limit of $\lambda \to 0$, when we recover particle-hole symmetry the propagators for the ϕ and ξ fields actually coincide and there are two zero modes. That can be checked by assuming particle-hole symmetry: $G_{\mathbf{k}\mathbf{k}'}(-i\omega) = -G_{\mathbf{k}\mathbf{k}'}(i\omega)$, in which case:

$$\begin{aligned}
\bar{\chi}_{cb}(i\omega_m) &= \frac{1}{\beta}\sum_{n\mathbf{k}\mathbf{k}'} G_{\mathbf{k}\mathbf{k}'}(i\omega_n)G_b(i\omega_m - i\omega_n), \\
&= \frac{1}{\beta}\sum_{n\mathbf{k}\mathbf{k}'} G_{\mathbf{k}\mathbf{k}'}(-i\omega_n)G_b(i\omega_m + i\omega_n), \\
&= -\frac{1}{\beta}\sum_{n\mathbf{k}\mathbf{k}'} G_{\mathbf{k}\mathbf{k}'}(i\omega_n)G_b(i\omega_m + i\omega_n), \\
&= \chi_{cb}(i\omega_m).
\end{aligned} \tag{5.74}$$

Further work is needed for the complete understanding of the effect of fluctuations of the fermionic fields in the mean field result.

5.4 Three Impurity Model: Exploring geometric frustration

As a second application of the supersymmetric-symplectic spin, we study a minimal model which brings in the issue of geometric frustration into play. The model consists of three local moments interacting among themselves by an antiferromagnetic Heisenberg coupling J_H and interacting with its respective bath of conduction electrons by a Kondo coupling J_K, as depicted in Fig. 5.7. We are motivated to look at this problem by experiments in CePdAl in which a partially ordered state is verified [67] and to explore the ability of the symplectic representation of the spin to describe frustrated systems.

The Hamiltonian is written as:

$$H = H_c + J_K\sum_a \mathbf{s}_a(0)\cdot\mathbf{S}_a + J_H\sum_a \mathbf{S}_a\cdot\mathbf{S}_{a+1}, \tag{5.75}$$

where now $a = \{1, 2, 3\}$ is the lead and local moment index with periodic boundary conditions. As in the previous section, H_c is the conduction electron Hamiltonian, $\mathbf{s}_a(0)$ is the spin density of conduction electrons at the site that is connected to the local moment $\mathbf{S}_a$.

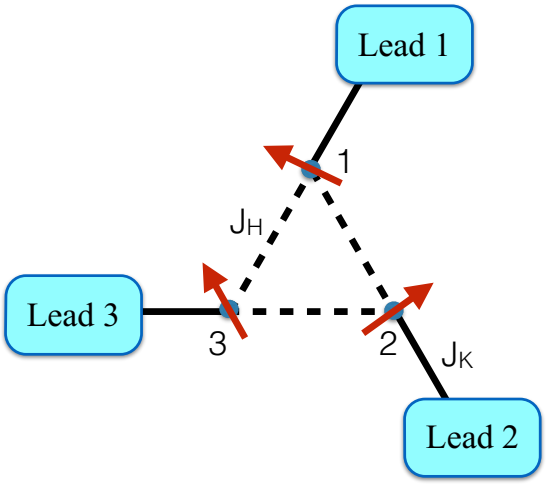

Figure 5.7: Schematic representation of the frustrated three-impurity model.

Introducing the supersymmetric-symplectic spin from Eq. 4.38 into the Hamiltonian, this can be written in the large-N limit as:

$$H = H_c - \frac{J_K}{N}\sum_{a\mathbf{k}\sigma\sigma'} c_{a\mathbf{k}\sigma}\bar{\Psi}_{a\sigma}\Psi_{a\sigma'}c^{\dagger}_{a\mathbf{k}\sigma'} + \frac{J_H}{2N}\sum_{a\sigma\sigma'}\bar{\Psi}_{a\sigma}\Psi_{a\sigma'}\bar{\Psi}_{a+1\sigma'}\Psi_{a+1\sigma}, \quad (5.76)$$

with $\Psi_{a\sigma}$ as defined in Eq. 4.42.

Proceeding as in the previous section, within a path integral formalism we introduce fluctuating fields in oder to decouple the quartic terms in the action and impose the constraint by the introduction of a delta function in the integral form. Within a static saddle point solution the problem decouples in to a bosonic and a fermionic part, effectively linked by the constraint. In this section we are going to leave the representation of the spin and the mean field parameters to be determined independently in each site. Omitting the details (similarly to the steps worked out in the previous section), the partition function in this case can be written as:

$$Z = Z_0 Z_F Z_B, \quad (5.77)$$

where

$$Z_0 = \int \Pi_a d\lambda_a e^{-\beta N \sum_a \lambda_a (q_{Fa}+q_{Ba}-q_0)}, \tag{5.78}$$

now fix the constraint in each site independently, allowing different sites to have different representations.

The fermionic part of the partition function can be written as:

$$Z_F = \int \mathcal{D}\mu_F e^{-S_F}, \quad \mathcal{D}\mu_F = \mathcal{D}[c, f, v_a, \lambda_{Fa}], \tag{5.79}$$

$$\begin{aligned} S_F &= S_c + \int_0^\beta d\tau \sum_{a\sigma} \left[\bar{f}_{a\sigma}(\partial_\tau + \lambda_{Fa}) f_{a\sigma} + \sum_{\mathbf{k}} \left(f^\dagger_{a\sigma} v_a c_{a\mathbf{k}\sigma} + h.c. \right) \right] \\ &+ \beta N \sum_a \frac{|v_a|^2}{J_K} - \beta N \sum_a \lambda_{Fa} q_{Fa}, \end{aligned} \tag{5.80}$$

where as in the previous section, we assume that the only fluctuating field that acquires a finite value at the saddle point solution is v_a. In this case the fermionic part of the solution reduces to three decoupled impurity problems, with the same solution as the previous section, now for 3 the leads:

$$\frac{F_F}{N} = -\frac{T_K}{\pi} \sum_a \sin(\pi q_{Fa}). \tag{5.81}$$

The bosonic part of the partition function reads:

$$Z_B = \int \mathcal{D}\mu_B e^{-S_B}, \quad \mathcal{D}\mu_B = \mathcal{D}[b, q_a, g_a, \lambda_{Ba}], \tag{5.82}$$

$$\begin{aligned} S_B &= \int_0^\beta d\tau \sum_\sigma \Psi^\dagger_{B\sigma} \frac{L_B}{2} \Psi_{B\sigma} - \frac{\beta N}{2J_H} \sum_a Tr[\Delta^\dagger_{Ba} \gamma_0^B \Delta_{Ba} \gamma_0^B] \\ &- \beta N \sum_a \lambda_{Ba}(q_{Ba} + 1/2), \end{aligned} \tag{5.83}$$

where now:

$$L_B = \begin{pmatrix} m_{B1} & \Delta_{B1} & \Delta_{B3}^{\dagger} \\ \Delta_{B1}^{\dagger} & m_{B2} & \Delta_{B2} \\ \Delta_{B3} & \Delta_{B2}^{\dagger} & m_{B3} \end{pmatrix}, \tag{5.84}$$

with

$$m_{Ba} = \begin{pmatrix} \partial_\tau + \lambda_{Ba} & 0 \\ 0 & -\partial_\tau + \lambda_{Ba} \end{pmatrix}, \tag{5.85}$$

$$\Delta_{Ba} = \begin{pmatrix} q_a & -g_a \\ \bar{g}_a & \bar{q}_a \end{pmatrix}, \tag{5.86}$$

and

$$\Psi_{B\sigma} = \begin{pmatrix} b_{1\sigma} \\ \tilde{\sigma} b_{1-\sigma}^{\dagger} \\ b_{2\sigma} \\ \tilde{\sigma} b_{2-\sigma}^{\dagger} \\ b_{3\sigma} \\ \tilde{\sigma} b_{3-\sigma}^{\dagger} \end{pmatrix}. \tag{5.87}$$

Note that the trace term in the action now appears with a minus sign since it is related to the bosonic part of the super-trace defined below Eq. 5.25. Here we define $\gamma_0^B = \sigma_3$ as the bosonic part of the original matrix γ_0. The solution of the bosonic part of the partition function is more involved if we allow the representations of the spin to be different in each lead.

5.4.1 Homogeneous solution

As a first solution we consider the same representation on every site, and look for an *homogeneous solution*, taking $\lambda_{Ba} \to \lambda_B$, $q_a \to q$ and $g_a \to g$. Integrating out the bosons and summing over Matsubara frequencies, in the zero temperature limit, the free energy can be written as:

$$\frac{F_B}{N} = (\lambda_B + 2q) + 2\sqrt{(\lambda_B - q)^2 - 3g^2} + \frac{3(g^2 - q^2)}{J_H} - 3\lambda_B(q_B + 1/2). \quad (5.88)$$

Minimizing the free energy with respect to q, g and λ_B one finds:

$$\frac{F_B}{N} = -\frac{3J_H}{2}(q_B + 1/2)^2, \quad (5.89)$$

up to a constant term.

The total free energy for the homogeneous solution can be written, already making explicit use of the constraint condition $q_F + q_B = q_0$, as:

$$\frac{F_{Hom}}{N} = -\frac{3}{\pi}A\sin(\pi q_F) - \frac{3}{2}(q_0 - q_F + 1/2)^2, \quad (5.90)$$

where again $A = \frac{T_K}{J_H}$ and the free energy is given in units of J_H. Note that this is functionally the same as the 2-impurity model up to an overall factor of $3/2$, and as a consequence the representation diagram determining the most favorable representation for the spin within an homogeneous solution will be identical to the 2-impurity case.

5.4.2 Inhomogeneous solution

Now we move on to investigate solutions with different representations in each site, what we call *inhomogeneous solution*. Due to frustration, we expect that it is energetically favorable for one of the spins to be in a fermionic representation, essentially disconnected from the other two spins with a bosonic or mixed representation, forming an antiferromagnetic bond. We assume one of the spins to always have a fermionic representation and let the representation of the two other spins to be selected as the one which minimizes the total

energy.

Now the problem reduces to a single impurity problem with a purely fermionic representation plus the two-impurity problem solved in the previous section. The free energy for the inhomogeneous solution reads:

$$\frac{F_{Inh}}{N} = -\frac{1}{\pi}A\sin(\pi q_0) - \frac{2}{\pi}A\sin(\pi q_F) - (q_0 - q_F + 1/2)^2,$$

in units of J_H. Again, the "phase diagram" of the representations will be the same as before, but now we compare the free energies of the homogeneous and inhomogeneous solutions for the 3-impurity problem. The hashed area in Fig. 5.8 is the region of the "phase diagram" in which the inhomogeneous solution is more favorable. This result provides an interesting interpretation for what is possibly happening in CePdAl [67]: one third of the local moments in the frustrated Kagome lattice (formed by an assemble of corner shared triangles) can be relieving the frustration by assuming an antisymmetric character and forming a Kondo singlet with a conduction electron, while the other two thirds of the local moments are assuming a bosonic character and developing magnetic order, allowing a partially disordered phase to be formed, as depicted in Fig. 5.3.

5.5 Conclusions and Perspectives

In this work we introduced a new supersymmetric-symplectic spin representation for large-N treatments. We have analyzed the properties of the supersymmetric-symplectic spin and its symmetries. We identified the supergroup $SU(2|1)$ as the group of transformations under which the spin is invariant.

We have proposed a new framework in the large-N limit, which allows the problem to sample different representations and to select the one which lowers the energy in a given point in parameter space. This gives the possibility of describing the phase diagram of heavy fermions within a single approach that is now able to capture the evolving character of the spin, and naturally provides microscopic framework for the phenomenological two-fluid picture for heavy fermions.

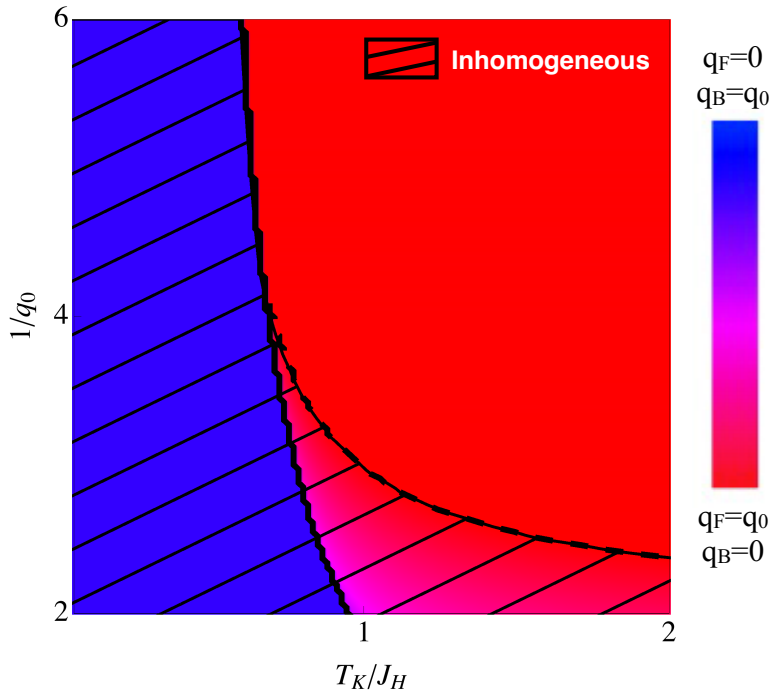

Figure 5.8: "Phase diagram" of the most favorable representation as a function of $A = \pi \frac{J_H}{T_K}$ and $1/q_0$ for the three-impurity model. The color code is the same as in Fig. 5.5. The hashed area represents the region of the phase diagram in which an inhomogeneous solution is energetically favorable.

Applying this approach to two toy models, the two-impurity model and the frustrated three-impurity model, we find positive results towards an unified description of heavy fermion systems. We find a *mixed phase* solution in which bosons and fermion coexist what allows the description of unusual phases of matter with coexistence of magnetism and Kondo effect, for example. Also, we find stable *inhomogenous solutions*, which can account for states as the partially ordered state in CePdAl, starting from a microscopic model.

This work motivates further investigations and leaves several open questions.

First, within the mixed phase, we find a new kind of zero mode due to the partial breaking of supersymmetry. This can be understood looking at an L-shape Young tableaux and verifying that the corner box in such kind of tableau can be associated either with a boson or a fermion. Given a state $|\Psi\rangle$ with a fermion assigned to the corner box, for

example, one can rotate:

$$|\Psi\rangle \rightarrow b^{\dagger} f|\Psi\rangle, \tag{5.91}$$

and find a new state which has same energy. This is an interesting property of the mixed phase and raises the questions: is there any new physics to this degeneracy or is it a trivial gauge degeneracy? Does it provide new kinds of zero modes or excitations which can lead to non-trivial physical consequences? These are very important questions and should be answered by the calculation of physical properties in this new phase in order to verify the effects of the new modes on scattering properties. One interesting possibility to find that these modes can provide novel critical behavior. These questions are left as subject for future work.

Second, we would like to discuss the application of this approach to lattice models. Extrapolating the results found in this work to the lattice we expect to find that for small ratios of T_K/J_H a bosonic representation is more favorable and consequently magnetic order can emerge once the bosons are able to condense given he dispersive character the bosonic energy acquires in the lattice solution. Heavy Fermi liquid behavior is expected to develop when there are fermions in the representation, which are able to hybridize with the conduction electrons. In case a mixed phase is stable in the lattice model, a heavy Fermi liquid phase is able coexist with magnetic order. In principle, this approach allows us to explore the different kinds of phase transitions as seen in $YbRh_2Si_2$ within a single approach: given that the fermions now can form a Fermi surface, the magnetic phase can emerge both from local moments within the bosonic representation or as an instability of the large Fermi surface. More interesting is the possibility of the description of superconductivity; this phase is likely to develop in the mixed phase and its vicinity, as a consequence of a valence-bond kind of magnetism emerging from the fermionic antiferromagnetic bonds. This is an interesting direction for future work.

Further investigations are needed for better understanding of the consequences of the new framework for the implementation of the constraint in the symplectic generalization. By fixing the total number of boxes in the representation we explicitly break the original

$SU(2|1)$ symmetry of the spin down to $SU(1|1)$, and only one zero mode is observed, related to the transformations of bosons into fermions, which is still a symmetry since the total number of bosons and fermions is preserved under this kind of transformation. Further analysis of a lattice model solution with the full constraint is needed in order to understand the effects of such zero mode.

Appendix A

Hubbard Operators

Hubbard operators were introduced in order to study strongly correlated systems in case the Coulomb interaction, ultimately related to the Hubbard U, is much larger than the hopping parameter t. The Hubbard operators are defined in such a way that they carry information about the specific initial and final state of a hopping process and exclude the possibility of double occupancy.

When treating f-electrons, the large Coulomb repulsion usually allows us to project out double occupied states, in which case the Hubbard operators come in hand. Here we introduce a notation for the Hubbard operators which highlights the f-character of the operators in order to make a better connection to the main text:

$$X_{\gamma\gamma'} = |4f^{13},\gamma\rangle\langle 4f^{13},\gamma'|, \tag{A.1}$$

$$X_{0\gamma} = |4f^{14}\rangle\langle 4f^{13},\gamma|, \tag{A.2}$$

$$X_{\gamma 0} = |4f^{13},\gamma\rangle\langle 4f^{14}|, \tag{A.3}$$

$$X_{00} = |4f^{14}\rangle\langle 4f^{14}|. \tag{A.4}$$

The Hubbard operators are written in terms of the $|4f^{13},\gamma\rangle$ "hole" states of the Yb^{3+} ion with total angular momentum component equal to γ and the filled shell Yb^{2+} state $|4f^{14}\rangle$. Here we note that these operators do not follow canonical commutation relations but:

$$[X_{\alpha\beta}(i), X_{\gamma\delta}(j)]_{\pm} = \delta_{ij}(\delta_{\beta\gamma}X_{\alpha\delta} \pm \delta_{\alpha\delta}X_{\gamma\beta}), \tag{A.5}$$

where we have anti-commutation relations (+) between the "fermionic" Hubbard operators

($X_{0\gamma}$ and $X_{\gamma 0}$) and commutation relations ($-$) between the "bosonic" Hubbard operators (X_{00} and $X_{\gamma\gamma'}$) and between fermionic and bosonic operators as well.

A.1 Slave Boson representation

In order to proceed with calculations using the standard many-body techniques we would like to write the Hubbard operators in terms of creation and annihilation operators. The most widely used representation of the Hubbard operators is the slave boson representation [89, 39], which can be written as:

$$X_{\gamma\gamma'}(j) = f^{\dagger}_{j\gamma} f_{j\gamma'}, \tag{A.6}$$

$$X_{0\gamma}(j) = b^{\dagger}_{j} f_{j\gamma}, \tag{A.7}$$

$$X_{\gamma 0}(j) = f^{\dagger}_{j\gamma} b_{j}, \tag{A.8}$$

$$X_{00}(j) = b^{\dagger}_{j} b_{j}, \tag{A.9}$$

where b_j and $f_{j\gamma}$ are a slave boson and Abrikosov pseudo-fermion, following the canonical bosonic and fermionic commutation relations, respectively. Here the charge degree of freedom is assigned to the bosons, while the spin degree of freedom is assigned to the fermions. This assignment can be understood in the following way: the filled shell (or empty state), is represented by a bosonic state, while the states with one or two holes (or electrons) are represented by fermionic states. Now the constraint is written as:

$$\sum_{\gamma} X_{\gamma\gamma} + X_{00} = \sum_{\gamma} f^{\dagger}_{j\gamma} f_{j\gamma} + b^{\dagger}_{j} b_{j} = 1, \tag{A.10}$$

which guarantees that the sites are never doubly occupied. The sites can be "empty" (with the full filled shell) when $n_B = 1$, or singly occupied (by a hole) when $n_F = 1$. This condition is implemented within a path integral formalism as a constraint in the theory. Here we note the convenience of the slave-particle approach in which case we have a holonomic constraint in stead of the non-holonomic constraint $n_F < 2$ in case we do not introduce the slave particle.

A.2 Slave Fermion representation

In an analogous fashion we can write the Hubbard operators with the inverse assignment of charge and spin [146]:

$$X_{\gamma\gamma'}(j) = b^{\dagger}_{j\gamma} b_{j\gamma'}, \tag{A.11}$$

$$X_{0\gamma}(j) = f^{\dagger}_{j} b_{j\gamma}, \tag{A.12}$$

$$X_{\gamma 0}(j) = b^{\dagger}_{j\gamma} f_{j}, \tag{A.13}$$

$$X_{00}(j) = f^{\dagger}_{j} f_{j}, \tag{A.14}$$

in which case the bosons carry the spin and the fermions the charge degrees of freedom. The constraint is now:

$$\sum_{\gamma} X_{\gamma\gamma} + X_{00} = \sum_{\gamma} b^{\dagger}_{j\gamma} b_{j\gamma} + f^{\dagger}_{j} f_{j} = 1. \tag{A.15}$$

Appendix B

Some facts about SP(N)

The SP(N) group is the group of $N \times N$ matrices over the reals which preserve a nondegenerate antisymmetric bilinear form [1]. The group is only defined for N even. In terms of matrices it can be defined as the matrices U which satisfy [147]:

$$U^T \boldsymbol{\epsilon} U = \boldsymbol{\epsilon}, \tag{B.1}$$

where $\boldsymbol{\epsilon}$ is an antisymmetric matrix $\epsilon^T = -\epsilon$.

Symplectic transformations are unimodular with $\det U = 1$.

B.1 Irreducible representations and Young diagrams

Young diagrams provide a simple way to label and characterize irreducible representations. It was introduced within the symmetric group and its use was also generalized to general linear groups. A Young diagram consists of a set of boxes arranged in left-justified rows of decreasing length:

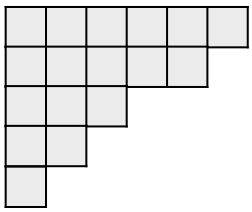

For tensor representations of a given rank r, the total number of boxes in the tableau is equal to r. To each box one can assign one index which is symmetrized with other indexes

[1] Note that different references use different notations. Here we use SP(N) as the group formed by $N \times N$ matrices.

in the same row and anti-symmetrized with other indexes in the same column. The shape of the diagram is labelled by a set of numbers $(f_{N/2}, f_{N/2-1}, ..., f_1)$, called partition, referent to the number of boxes in each row (here we already introduce the notation that will be convenient for the discussion of SP(N) in particular), where $f_{N/2} + f_{N/2-1} + ... + f_1 = r$. From these diagrams one can infer the dimension of the given representation and also use them for the determination of characters [147].

B.2 Casimirs

Following [131], the second Casimir for SU(N) representation given by the partition $(f_{N/2}, f_{N/2-1}, ..., f_1)$ can be written as:

$$C_2 = \sum_{i=-N/2}^{N/2} (\lambda_i^2 - \rho_i^2), \tag{B.2}$$

where the sum does not include $i = 0$ and

$$\left.\begin{aligned} \lambda_i &= f_i + N/2 + i \\ \rho_i &= N/2 + i \end{aligned}\right\} \text{for } i > 0 \tag{B.3}$$

$$\left.\begin{aligned} \lambda_i &= -f_{-i} + N/2 + i \\ \rho_i &= N/2 + i \end{aligned}\right\} \text{for } i < 0 \tag{B.4}$$

Since we are interested in L-shaped Young diagrams with width w and height w we can find a simplified form for the second Casimir if terms of these parameters. We know that:

$$f_i = \begin{cases} w, & \text{for } i = N/2 \\ 1, & \text{for } N/2 - 1 \leq i \leq N/2 - h + 1 \\ 0, & \text{for } i > N/2 - h + 1 \end{cases} \tag{B.5}$$

so that

$$\lambda_i^2 - \rho_i^2 = \begin{cases} w^2 + 4Nw, & \text{for } i = N/2 \\ w^2, & \text{for } i = -N/2 \\ 1 + 2(N+1), & \text{for } i > 0 \\ 1 - 2(N+1), & \text{for } i < 0 \\ 0, & \text{for } |i| > N/2 - h + 1 \end{cases} \tag{B.6}$$

Summing over i:

$$C_2 = 2(w+h)(w-h+2N) + 4h - 2 - 4N. \tag{B.7}$$

In case we identify $Q = w + h - 1$ and $Y = h - w$, we can write:

$$C_2 = 2Q(N + 1 - Y). \tag{B.8}$$

B.3 Decomposition of Products of Representations

Following [148], the Young diagrammatic method to decompose the product of representations in SU(N) can be generalized for SP(N). If we are interested in the product of two representations $[f_1]_{\xi_1}$ e $[f_2]_{\xi_2}$, where ξ_n is the number of boxes used to describe the representation and $[f] = (f_{N/2}, f_{N/2-1}, ...)$, the procedure goes as follows:

- Start with the product of the representations in the usual way using the Young diagrams.
- Also take the product of the representations after removing simultaneously k-boxes from the original representations. Here $k = 1, 2, 3, ...min\{\xi_1, \xi_2\}$. This removal can be done in all possible ways under two restrictions:

  A) The resulting diagram should be standard Young diagram.

  B) No more than two boxes in the same column (row) in $[f_1]$ with those in the same row (column) in $[f_2]$ can be removed simultaneously. This is required given the

symmetrization (antisymmetrization) of the indexes if the boxes are in a row (column) in the diagram. Removing two indices means to trace over them and the trace over antisymmetrized indices is zero.

- For SP($N = 2l$), if the representation obtained $[\lambda] = (\lambda_{N/2}, \lambda_{N/2-1}, ..., \lambda_{N/2-p+1}, 0, 0, ...)$ has $p > l$ then we have a non-standard diagram (p is in fact the number of rows with nonzero boxes). In this case we need to remove boxes from the diagram along a continuous hook of length $2p - n - 2$ and depth x, with x being counted from the first column to the right most column the hook reaches. The resultant Young diagram will be admissible or set to zero if, at any stage, the removal of the required hook leaves an irregular Young diagram. The diagram gets a factor of $(-1)^{x+1}$.

One important result is the fact that the decomposition of the product of a representation with itself always gives rise to a singlet state (this follows from the removal of all boxes from both representations in the product, leading to singlets).

Appendix C

Discussion on the linearization of the constraint

In Chapter 4 we introduced the second Casimir in its operator form as the condition defining a super-surface in an 8-dimensional space with directions referent to each generator, subject to a complex measure $\mathbf{\Lambda}$:

$$4\mathbf{S}\cdot\mathbf{S} = \mathbf{V}_S\cdot\mathbf{\Lambda}\cdot\mathbf{V}_S, \tag{C.1}$$

where $\mathbf{V}_S = (\Psi_0, \Psi_1, \Psi_2, \Psi_3, A_1, A_2, B_1, B_2)$ and

$$\mathbf{\Lambda} = \begin{pmatrix} \gamma_1 & 0 \\ 0 & \mathbf{M} \end{pmatrix}, \tag{C.2}$$

with $\gamma_1 = diag[1,-1,-1,-1]$ and

$$\mathbf{M} = \begin{pmatrix} 0 & -1 & 0 & 0 \\ 1 & 0 & 0 & 0 \\ 0 & 0 & 0 & 1 \\ 0 & 0 & -1 & 0 \end{pmatrix}, \tag{C.3}$$

as introduced in the main text.

When implementing the above constraint in our theory, it introduces interacting terms that can be decoupled by a Hubbard-Stratonovich transformation. Within a static mean field solution we already know that the fermionic part of the constraint will not contribute to the mean field solution (fermionic operators are anti-periodic in imaginary time), so we can take $A_1 = A_2 = B_1 = B_2 = 0$. Also, if we are not interested in superconducting

solutions the constraint reduces to fixing:

$$4\mathbf{S}\cdot\mathbf{S} = \Psi_0^2 - \Psi_3^2, \tag{C.4}$$

what defines a hyperbola in a 2-dimensional space. Redefining the operators as:

$$\Psi_B = \frac{\Psi_0}{N} = n_B/N + 1/2, \tag{C.5}$$

$$\Psi_F = \frac{\Psi_3}{N} = n_F/N - 1/2, \tag{C.6}$$

we can write the constraint as:

$$s^2 = \Psi_B^2 - \Psi_F^2, \tag{C.7}$$

where the parameter s now controls the magnitude of the spin according to:

$$\mathbf{S}\cdot\mathbf{S} = \frac{s^2N^2}{4}. \tag{C.8}$$

From the form above we can note the following points:

1. The values of Ψ_B are bounded from below to $\Psi_B = 1/2$ (for $n_B = 0$) and unbounded from above.

2. The values of Ψ_F are bounded from below to $\Psi_F = -1/2$ (for $n_F = 0$) and from above to $\Psi_F = 0$ (maximum number of fermions is $n_F = N/2$).

3. A completely bosonic representation is characterized by $\Psi_F = -1/2$ (or $n_F = 0$).

4. A completely fermionic representation is characterized by $\Psi_B = 1/2$ (or $n_B = 0$).

Note now that the maximum value of $\mathbf{S}\cdot\mathbf{S}$ which can be described purely by fermions is for the case $n_B = 0$ and $n_F = N/2$:

$$s^2 = \left(0 + \frac{1}{2}\right)^2 - \left(\frac{1}{2} - \frac{1}{2}\right)^2 = 1/4, \tag{C.9}$$

restricting the maximum value of the spin to $s = 1/2$. For $s > 1/2$ the spin cannot

be described purely by fermions, and there is always a bosonic component to it. Given this fact we restrict the discussion to values of $s < 1/2$ so that our solution can sample representations ranging from purely bosonic to purely fermionic for a given N.

Within the restrictions on the values of Ψ_B and Ψ_F enumerated above, we can plot the hyperbolic constra

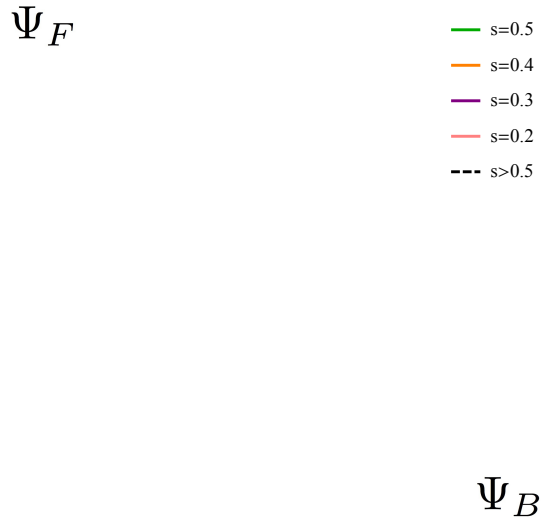

Figure C.1: Plot of the hyperbolae constraints for different magnitudes of the spin, or values of s. The full colored lines indicate the physical $s < 1/2$, and the black dotted hyperbolae the unphysical $s > 1/2$ lines. The straight dashed lines indicate the linear constraint approximation. The lower horizontal axis (in blue) refers to a fully bosonic representation, while the left vertical axis (in red) refers to a purely fermionic representation.

From the figure above we can see that only the colored curves (for $s < 1/2$) actually span from the completely bosonic representation (located an the bottom horizontal axis, in blue) to the fully fermionic representation (located in the left vertical axis, in red) for a given value of $\mathbf{S} \cdot \mathbf{S}$. The figure also shows hyperbolae for $s > 1/2$, which does not have a fully fermionic representation. Also, we note that as $s \to 0$ the constraint behaves essentially as a straight line satisfying $\Psi_B + \Psi_F = cte$, what motivates the use of a simplified form of the constraint in our approach.

Approximating the hyperbolae of constant $\mathbf{S} \cdot \mathbf{S}$ by straight lines, we can write:

$$\Psi_B + \Psi_F = n_B + n_F = q. \tag{C.10}$$

We can now relate the size of the spin, or the parameter s, with the value of the parameter $q = Q/N$. By matching the left most point of the hyperbola with the linear constraint, we are matching the point with coordinates $\Psi_B = 1/2$ and:

$$\Psi_F = -\sqrt{\Psi_B^2 - s^2} = -\sqrt{1/4 - s^2}, \tag{C.11}$$

so

$$\Psi_B + \Psi_F = q = 1/2 - \sqrt{1/4 - s^2}, \tag{C.12}$$

what defines the relation between s and q. Note that the minimum value of $q = 0$ (for $s = 0$ and the maximum value $q = 2$ (for $s = 1/2$). Fig. C.1 shows the hyperbolae constraints and the respective linear constraints.

We can also estimate by how much the magnitude of the spin is deviating from its starting value by taking the linear constraint in stead of the hyperbolic constraint. Note that the linear and hyperbolic constraints are not exactly the same in the other extreme, what means that the linear constraint is now matching some other hyperbolic curve referent to a different spin size s. We can estimate this new spin size by finding the hyperbola which passes through the point $\Psi_F = -1/2$ and

$$\Psi_B = q - \Psi_F = q + 1/2 = 1 - \sqrt{1/4 - s^2}. \tag{C.13}$$

The new hyperbola can be written as:

$$(s')^2 = \Psi_B^2 - \Psi_F^2 = 1 - s^2 - 2\sqrt{1/4 - s^2}. \tag{C.14}$$

Note that the ratio s'/s tends to one as $s \to 0$, as expected, and has its maximum deviation for $s \sim 1/2$.

Appendix D

Fermionic part of the free energy

The fermionic part of the solution reduces to two decoupled impurity problems. Here we show explicitly the single impurity solution. The partition function for a single impurity can be written as:

$$Z_F = \int \mathcal{D}\mu_F e^{-S_F}, \quad D\mu_F = D[c, f, v, \lambda_F], \tag{D.1}$$

already transforming from imaginary time to Matsubara frequencies:

$$\begin{aligned} S_F &= \sum_n \left[\sum_{\mathbf{k}\sigma} c^\dagger_{\mathbf{k}\sigma}(-i\omega_n + \epsilon_{\mathbf{k}}) c_{\mathbf{k}\sigma} + \sum_\sigma f^\dagger_\sigma(-i\omega_n + \lambda_F) f_\sigma \right. \\ &\quad \left. + \sum_\sigma \left(\sum_{\mathbf{k}} f^\dagger_\sigma v c_{\mathbf{k}\sigma} + h.c. \right) \right] + \beta N \sum_{\mathbf{k}} \frac{|v|^2}{J_K} - \beta N \lambda_F q_F. \end{aligned} \tag{D.2}$$

We start by integrating out the conduction electrons, taking into account their effect in the self energy of the fermions that compose the spin. The effective fermion propagator can be written as:

$$\begin{aligned} G_f &= G^0_f + G^0_f v^* \sum_{\mathbf{k}} G^0_{c\mathbf{k}} v G^0_f + G^0_f v^* \sum_{\mathbf{k}} G^0_{c\mathbf{k}} v G^0_f v^* \sum_{\mathbf{k}'} G^0_{c\mathbf{k}'} v G^0_f + ... \\ &= G^0_f + G^0_f v^* \sum_{\mathbf{k}} G^0_{c\mathbf{k}} v G_f, \\ &= [(G^0_f)^{-1} - \Sigma_f]^{-1}, \end{aligned} \tag{D.3}$$

where $(G^0_f)^{-1} = i\omega_n - \lambda_F$ is the bare f-fermion propagator, and

$$\Sigma_f = \sum_{\mathbf{k}} |v|^2 G^0_{c\mathbf{k}}, \tag{D.4}$$

is the f-fermion free energy, where $(G^0_{c\mathbf{k}})^{-1} = i\omega_n - \epsilon_{\mathbf{k}}$ is the bare conduction electron propagator.

We evaluate the sum over $\mathbf{k}$ in Σ_f as an integral over energy with a constant density of states. Analytically continuing the Matsubara frequencies to the real axis ($\omega_n \to \omega \pm i\delta$):

$$\begin{aligned} \Sigma_f &= |v|^2 \sum_{\mathbf{k}} \frac{1}{\omega \pm i\delta - \epsilon_{\mathbf{k}}} \\ &= |v|^2 \int_{-D}^{D} \rho(\epsilon) d\epsilon \left(\frac{1}{w - \epsilon} \mp i\pi\delta(\omega - \epsilon) \right), \\ &= -i\Gamma\Theta(D - |\omega|) sgn(\tilde{\omega}), \end{aligned} \tag{D.5}$$

where $\Gamma = \pi N(0)|v|^2$, D the bandwidth, $N(0)$ the constant density of states, $\Theta(x)$ the Heaviside step function. Here $\tilde{\omega}$ indicates the imaginary part of the frequency.

Now the fermionic part of the free energy reads:

$$S_F = \sum_{n\sigma} f^\dagger_\sigma(i\omega_n)(-i\omega_n + \lambda_F + i\Gamma_n) f_\sigma(i\omega_n) + \beta \frac{N|v|^2}{J_K} - \beta N \lambda_F q_F, \tag{D.6}$$

where $\Gamma_n = \Gamma\Theta(D - |\omega_n|) sgn(\tilde{\omega}_n)$. We can integrate out the f-fermions and write an effective action at the saddle point values of v and λ_F (to be determined by extremization of the free energy, see main text):

$$S_F^{Eff} = -\sum_{n\sigma} \log[-i\omega_n + \lambda_F + i\Delta_n] + \beta \frac{N|v|^2}{J_K} - \beta N \lambda_F q_F. \tag{D.7}$$

The sum over Matsubara frequencies can be performed as an integral in the complex plane weighted by the Fermi distribution function $f(z) = (e^{\beta z} - 1)^{-1}$. Note that the

integrand has a branch-cut:

$$\begin{aligned} & \sum_{n\sigma} \log[-i\omega_n + \lambda_F + i\Delta\Theta(D - |\omega_n|)sgn(\tilde{\omega}_n)] \qquad \text{(D.8)} \\ = \; & \frac{\beta N}{2\pi i} \int_C dx \log[-z + \lambda_F + i\Delta\Theta(D - |z|)sgn(\tilde{z})] f(z) \\ = \; & \frac{\beta N}{2\pi i} \left[\int_{-D}^{D} dz f(z) \log[-z + \lambda_F - i\Delta] \right. \\ & \left. + \int_{D}^{-D} dz f(z) \log[-z + \lambda_F + i\Delta] \right], \end{aligned}$$

which simplifies to:

$$\begin{aligned} & \sum_{n\sigma} \log[-i\omega_n + \lambda_F + i\Delta\Theta(D - |\omega_n|)sgn(\tilde{\omega}_n)] \qquad \text{(D.9)} \\ = \; & -\frac{\beta N}{\pi} \int_{-D}^{D} dz f(z) Im[\log[-z + \lambda_F + i\Delta]]. \qquad \text{(D.10)} \end{aligned}$$

In the zero temperature limit the Fermi function sets the upper limit of the integral to zero. Evaluating the integral we determine the free energy:

$$\frac{F_F}{N} = \frac{1}{\pi} Im \left[(\lambda_F + i\Delta) \ln \left(\frac{\lambda_F + i\Delta}{De} \right) \right] + \frac{|v|^2}{J_K} - \lambda_F q_F, \qquad \text{(D.11)}$$

which can be rewritten as:

$$\frac{F_F}{N} = \frac{1}{\pi} Im \left[\xi_F \ln \left(\frac{\xi_F}{eT_K e^{i\pi q_F}} \right) \right], \qquad \text{(D.12)}$$

once we define

$$\xi_F = \lambda_F + i\Delta, \qquad \text{(D.13)}$$

and the Kondo temperature

$$T_K = De^{-1/N(0)J_K}. \qquad \text{(D.14)}$$

Appendix E

Bosonic part of the free energy

From the main text we have that the bosonic part of the partition function is:

$$Z_B = \int \mathcal{D}\mu_B e^{-S_B}, \quad \mathcal{D}\mu_B = D[b, g, \lambda_B], \tag{E.1}$$

already transforming from imaginary time to Matsubara frequencies:

$$S_B = \sum_{n\sigma} \Psi^{\dagger}_{B\sigma}(i\nu_n) L_B(i\nu_n) \Psi_{B\sigma}(i\nu_n) + \beta N \frac{|g|^2}{J_H} - 2\beta N \lambda_B (q_B + 1/2), \tag{E.2}$$

where

$$L_B(i\nu_n) = \begin{pmatrix} -i\nu_n + \lambda_B & g \\ \bar{g} & i\nu_n + \lambda_B \end{pmatrix}, \tag{E.3}$$

$$\Phi_{B\sigma}(i\nu_n) = \begin{pmatrix} b_{1\alpha}(i\nu_n) \\ \tilde{\sigma} b^{\dagger}_{2-\sigma}(-i\nu_n) \end{pmatrix}. \tag{E.4}$$

Integrating out the bosons and taking the saddle point value of λ_B and g, which will be determined by the extremization of the free energy with respect to these parameters, we can write:

$$Z_B = e^{-S_B^{Eff}}, \tag{E.5}$$

where

$$\begin{aligned} S_B^{Eff} &= \sum_{n\sigma} \log[Det[L_B(i\nu_n)]] + \beta N \frac{|g|^2}{J_H} - 2\beta N \lambda_B (q_B + 1/2), \\ &= N \sum_{n,x=\pm} \log[E_B^x - i\nu_n] + \beta N \frac{|g|^2}{J_H} - 2\beta N \lambda_B (q_B + 1/2), \end{aligned} \tag{E.6}$$

where

$$E_B^x = x\sqrt{\lambda_B^2 - g^2}. \tag{E.7}$$

The sum over Matsubara frequencies can be written in terms of an integral over the imaginary plane weighted by the bosonic distribution function $n(z) = (e^{\beta z} - 1)^{-1}$:

$$\sum_{n,x=\pm} \log[E_B^x - i\nu_n] = -\beta N \sum_{x=\pm} \int_C \frac{dz}{2\pi i} \log[E_B^x - z] n(z). \tag{E.8}$$

In the zero temperature limit:

$$\sum_{n\sigma} \log[Det[L_B(i\nu_n)]] \xrightarrow{T\to 0} N \sum_{x=\pm} (-E_B^x)\Theta(-E_B^x), \tag{E.9}$$

where $\Theta(x)$ is the Heaviside step function, so that the bosonic part of the free energy reads:

$$\frac{F_B}{N} = \sqrt{\lambda_B^2 - g^2} + \frac{g^2}{J_H} - 2\lambda_B (q_B + 1/2). \tag{E.10}$$

Appendix F

Fluctuations of the local fermionic fields

In this appendix we define and compute $\chi_{cb}(i\omega_n)$. From the main text we have:

$$\chi_{cb}(i\omega_r) = -\frac{1}{\beta}\sum_{\mathbf{k}\mathbf{k}'m} G_b(i\omega_r + i\omega_m)G_{\mathbf{k}\mathbf{k}'}(i\omega_m) \tag{F.1}$$

where,

$$G_b(i\nu_n) \;\; = \;\; (i\nu_n - \xi_B)^{-1} \tag{F.2}$$

is the bosonic propagator, with $\xi_B = \sqrt{\lambda_B^2 - |g|^2}$, and

$$G_{\mathbf{k}\mathbf{k}'}(i\omega_n) \;\; = \;\; G^0_{\mathbf{k}}(i\omega_n)\delta_{\mathbf{k}\mathbf{k}'} + |v|^2 G^0_{\mathbf{k}}(i\omega_n)G_f(i\omega_n)G^0_{\mathbf{k}'}(i\omega_n), \tag{F.3}$$

with same definitions as in Appendix D.

Evaluating the sum over momenta:

$$\sum_{\mathbf{k}\mathbf{k}'} G_{\mathbf{k}\mathbf{k}'}(i\omega_n) \;\; = \;\; \sum_{\mathbf{k}} G^0_{\mathbf{k}}(i\omega_n) + |v|^2 G_f(i\omega_n)\left(\sum_{\mathbf{k}} G^0_{\mathbf{k}}(i\omega_n)\right)^2, \tag{F.4}$$

we know

$$\sum_{\mathbf{k}} G^0_{\mathbf{k}}(i\omega_n) = -i\pi N(0) sgn(\omega_n), \tag{F.5}$$

as computed in the evaluation of the fermionic part of the free energy. In the infinite

bandwidth limit the sum over $\mathbf{k}$ can be written as:

$$\sum_{\mathbf{k}\mathbf{k}'} G_{\mathbf{k}\mathbf{k}'}(i\omega_n) = -i\pi N(0) sgn(\omega_n) - \frac{\pi N(0)\Gamma}{i\omega_n - \lambda_F + i\Gamma sgn(\omega_n)} \tag{F.6}$$

where $N(0)$ is a constant density of states and $\Gamma = \pi N(0)|v|^2$ as before.

Back to the computation of χ_{cb}:

$$\chi_{cb}(i\omega_r) = \chi^1_{cb}(i\omega_r) + \chi^2_{cb}(i\omega_r), \tag{F.7}$$

the first term is equal to:

$$\begin{aligned}
\chi^1_{cb}(i\omega_r) &= \frac{1}{\beta}\sum_m \frac{i\pi N(0) sgn(\omega_m)}{i\omega_m + i\omega_r - \xi_B} \\
&= \frac{i\pi N(0)}{2\pi i}\oint dz f(z)\frac{sgn(\tilde{z})}{z + i\omega_r - \xi_B} \\
&= -i\pi N(0) f(\lambda_B - i\omega_r) \\
&+ \frac{i\pi N(0)}{2\pi i}\left[\int_{-D}^{D} dz f(z)\frac{(-1)}{z + i\omega_r - \xi_B} + \int_{D}^{-D} dz f(z)\frac{(+1)}{z + i\omega_r - \xi_B}\right],
\end{aligned} \tag{F.8}$$

where $\tilde{z} = Im(z)$ and $f(\lambda_B - i\omega_r) = -n(\lambda_B)$. In the zero temperature limit $f(z) \to \theta(-z)$ and $n(\lambda_B > 0) \to 0$, so:

$$\chi^1_{cb}(i\omega_r) = -N(0)\log\left(\frac{-\xi_B + i\omega_r}{-\xi_B + i\omega_r - D}\right). \tag{F.9}$$

The second part of $\chi_{cb}(i\omega_r)$:

$$\chi^2_{cb}(i\omega_r) = \frac{1}{\beta}\sum_m \frac{\pi N(0)\Delta}{i\omega_m - \lambda_F + i\Delta sgn(\omega_m)}\frac{1}{i\omega_m + i\omega_r - \xi_B} \tag{F.10}$$

can be computed in analogous fashion:

$$\begin{aligned}
\chi^2_{cb}(i\omega_r) &= \frac{N(0)\Delta}{2i}\frac{1}{i\omega_r - \xi_B + \lambda_F + i\Delta} \\
&\times \left[Log\left(\frac{-\lambda_F - i\Delta}{-\lambda_F - i\Delta - D}\right) - Log\left(\frac{-\xi_B + i\omega_r}{-\xi_B + i\omega_r - D}\right)\right] + (i\Delta \to -i\Delta).
\end{aligned} \tag{F.11}$$

Continuing to real frequencies $\omega_r \to \omega \pm i\epsilon$, writing $1/J_K = -N(0)Log|(\lambda + i\Delta)/D|$, in the infinite bandwidth limit:

$$\begin{aligned}\chi_{cb}(\omega - i\epsilon) - \frac{1}{J_K} &= +N(0)Log\left|\frac{\lambda_F + i\Delta}{\xi_B - \omega \mp i\epsilon}\right| - i\pi N(0)\Theta(\omega - \lambda) \\ &+ \frac{N(0)\Delta}{2i}\frac{1}{\omega \pm i\epsilon - \xi_B + \lambda_F + i\Delta}Log\left(\frac{\lambda_F + i\Delta}{\xi_B - \omega \mp i\epsilon}\right) \\ &- \frac{N(0)\Delta}{2i}\frac{1}{\omega \pm i\epsilon - \xi_B + \lambda_F - i\Delta}Log\left(\frac{\lambda_F - i\Delta}{\xi_B - \omega \mp i\epsilon}\right).\end{aligned} \tag{F.12}$$

In the transition line, where $\xi_B = \xi_F \Rightarrow \sqrt{\lambda_B^2 - g^2} = \lambda_B = \lambda_F = \lambda$, we have the simplified form:

$$\begin{aligned}\chi_{cb}(\omega - i\epsilon) - \frac{1}{J_K} &= +N(0)Log\left|\frac{\lambda + i\Delta}{\lambda - \omega + i\epsilon}\right| - i\pi N(0)\Theta(\omega - \lambda) \\ &+ \frac{N(0)\Delta}{2i}\frac{(\omega - i\Delta)}{\omega^2 + \Delta^2}Log\left(\frac{\lambda + i\Delta}{\lambda - \omega + i\epsilon}\right) + (i\Delta \to -i\Delta),\end{aligned} \tag{F.13}$$

rewriting,

$$\chi_{cb}(\omega - i\epsilon) - \frac{1}{J_K} = N(0)\omega Re\left[\frac{Log(\lambda + i\Delta)}{\omega + i\Delta}\right] - \frac{N(0)\omega^2}{\Delta^2 + \omega^2}\log(\lambda - \omega + i\epsilon), \tag{F.14}$$

which is the form of χ_{cb} discussed in the main text.

References

[1] P. W. Anderson, Science 177, 4047, 393 (1972).

[2] P. Coleman, Ann. Henri Poincaré 4, 1 (2003).

[3] J. Bardeen, L. N. Cooper, and J. R. Schrieffer, Phys. Rev. 108, 1175 (1957).

[4] C. Kittel, Introduction to Solid State Physics, John Wiley & Sons (1986).

[5] J. Nagamatsu, N. Nakagawa, T. Muranaka, Y. Zenitani and J. Akimitsu, Nature 410, 63 (2001).

[6] G. Knebel, D. Aoki, D. Braithwaite, B. Salce and J. Flouquet, Phys. Rev. B 74 020501 (2006).

[7] G. Knebel, J. Buhot, D. Aoki, G. Lapertot, S. Raymond, E. Ressouche and J. Flouquet, J. Phys. Soc. Jpn. 80, SA001 (2011).

[8] M. Azuma, K. Takata, T. Saito, S. Ishiwata, Y. Shimakawa and M. Takano, J. Am. Chem. Soc. 127, 8889 (2005).

[9] A. Schilling, M. Cantoni, J. D. Guo and H. R. Ott, Nature 363, 56 (1993).

[10] K. Momma and F. Izumi, J. Appl. Crystallogr., 44, 1272-1276 (2011).

[11] N. W. Ashcroft and N. D. Mermin, Solid State Physics, Thomson Learning (1976).

[12] L. Landau, Sov. Phys. JETP 3, 920 (1957).

[13] P. Coleman, Introduction to Many-Body Physics, Cambridge University Press (2015).

[14] K. G. Wilson, Rev. Mod. Phys. 47, 4 (1975).

[15] L. Landau. Sov. Phys. JETP 7, 19 (1937).

[16] H. L. Stormer, D. C. Tsui and A. C. Gossard, Rev. Mod. Phys. 71, S298 (1999).

[17] P.W. Anderson, Mater. Res. Bull. 8, 153 (1973).

[18] X.-G. Wen, ISRN Cond. Mat. Phys. 2013, 198710 (2013).

[19] J. L. Smith and E. A. Kmetko, J. of the Less-Common Metals 90, 83 (1983).

[20] P. Coleman in Handbook of Magnetism and Advanced Magnetic Materials, Vol. 1, Eds H. Kronmuller and S. Parkin, (John Wiley and Sons), 95-148 (2007).

[21] B. Keimer, S. A. Kivelson, M. R. Norman, S. Uchida and J. Zaanen, Nature 518, 179 (2015).

[22] G. R. Stewart, Rev. Mod. Phys. 83, 1589 (2011).

[23] K. Andres, J. E. Graebner, and H. R. Ott, Phys. Rev. Lett. 35, 1779 (1975).

[24] *"Heavy Fermion Systems"*, Ed. Prasanta Mitra, Handbook of Metal Physics Vol 2, 1-338 (Elsevier, 2008).

[25] Q. Si and F. Steglich, Science 329, 1161 (2010).

[26] P. Gegenwart, Q. Si, and F. Steglich, Nature Physics 4, 186 (2008).

[27] G. R. Stewart, Rev. Mod. Phys. 73, 797 (2001).

[28] P. W. Anderson, Phys. Rev. 124, 41 (1961).

[29] J. Hubbard, Proc. Roy. Soc. A 285, 542 (1965).

[30] C. Zener, Phys. Rev. 81, 440 (1951).

[31] J. Kondo, Prog. Theo. Phys. 32, 1 (1964).

[32] A. C. Hewson, The Kondo Problem to Heavy Fermions, Cambridge University Press, Cambridge, England (1993).

[33] P. Nozières, Jour. of Low Temp Phys. 17, 112 (1974).

[34] Y. Onuki and T. Komatsubara, J. Mag. Mat. 63, 281 (1987).

[35] G. D. Mahan, Many-particle Physics, Plenum Press (1990).

[36] G. t Hooft, Nucl. Phys. B 72, 461 (1974); G. t Hooft, Nucl. Phys. B 75, 461 (1974).

[37] P. W. Anderson, Valence Fluctuations in Solids, Amsterdam: North-Holland (1981).

[38] N. Read and D. Newns, J. Phys. C 16, 3273 (1983).

[39] P. Coleman, Phys. Rev. B. 29, 3035 (1984).

[40] P. Coleman, Phys. Rev. B. 35, 5072 (1987).

[41] A. Auerbach, Interacting Electrons and Quantum Magnetism, Springer-Verlag (1994).

[42] R. L. Stratonovich, Soviet Physics Doklady, Vol. 2, 416 (1957); J. Hubbard, Phys. Rev. Lett. 3, 77 (1959).

[43] M.A. Ruderman and C. Kittel, Phys. Rev. 96, 99 (1954); T. Kasuya, Prog. Theor. Phys. 16, 45 (1956); K. Yosida, Phys. Rev. 106, 893 (1957).

[44] S. Doniach, Physica B 91, 231 (1977).

[45] J. Custers, P. Gegenwart, H. Wilhelm, K. Neumaier, Y. Tokiwa, O. Trovarelli, C. Geibel, F. Steglich, C. Pépin and P. Coleman, Nature 424, 524 (2003).

[46] Q. Si and F. Steglich, Science 329, 1161 (2010).

[47] Q. Si, J.-X. Zhu and D. R. Grempel, J. Phys.: Condens. Matt. 17, R1025 (2005).

[48] Q. Si, S. Rabello, K. Ingersent and J. L. Smith, Nature 413, 804 (2001).

[49] J. A. Hertz, Phys. rev. B 14, 1165 (1976); A. J. Millis, Phys. Rev. B 48, 7183 (1993); T. Moriya and T. Takimoto, J. Phys. Soc. Japn. 64, 960 (1995).

[50] T. Senthil, M. Vojta and S. Sachdev, Phys. Rev. B 69, 035111 (2004).

[51] T. Senthil, A. Vishwanath, L. Balents, S. Sachdev and M. P. A. Fisher, Sicence 303, 1490 (2004).

[52] Q. Si, Physica B 378, 23 (2006).

[53] Q. Si and S. Paschen, Phys. Status Solidi B 250, 425 (2013).

[54] P. Coleman and A. Nevidomskyy, J. Low Temp. Phys. 161, 182 (2010).

[55] P. Fazekas, Lecture Noted on Electron Correlation and Magnetism, Series in Modern Condensed Matter Physics, Vol. 5, World Scientific (1999).

[56] E. Schuberth, YbRh2Si2 at ultralow temperatures: Superconductivity and antiferromagnetism, talk at KITP Conference: Strong Correlations and Unconventional Superconductivity: Towards a Conceptual Framework (2014).

[57] H. v. Lohneysen, T. Pietrus, G. Portisch, H. G. Schlager, A. Schroeder, M. Sieck and T. Trappmann, Phys. Rev. Lett. 72, 3262 (1994).

[58] A. Schroeder, G. Aeppli, R. Coldea, M. Adams, O. Stockert, H. v. Lohneysen, E. Bucher, R. Ramazashvill and P. Coleman, Nature, 407, 351 (2000).

[59] M. Yashima, H. Mukuda, Y. Kitaoka, H. Shishido, R. Settai, and Y. Onuki, Phys. Rev. B 79, 214528 (2009).

[60] S. Nakatsuji, K. Kuga, Y. Machida, T. Tayama, T. Sakakibara, Y. Karaki, H. Ishimoto, S. Yonezawa, Y. Maeno, E. Pearson, G. G. Lonzarich, L. Balicas, H. Lee and Z. Fisk, Nature 4, 603 (2008).

[61] Y. Matsumoto, S. Nakatsuji, K. Kuga, Y. Karaki, N. Horie, Y. Shimura, T. Sakakibara, A. H. Nevidomskyy and P. Coleman, Science 21, 316 (2011).

[62] T. Tomita, K. Kuga, Y. Uwatoko and S. Nakatsuji, arXiv:1501.03852 (2015).

[63] K. Deguchi, S. Matsukawa, N. K. Sato, T. Hattori, K. Ishida, H.Takakura andT. Ishimasa, Nature Materials 11, 1013 (2012).

[64] Y. Tokiwa, C. Stingl, M.-S. Kim, T. Takabatake and P. Gegenwart, Sci. Adv. 1, e1500001 (2015).

[65] M. S. Kim, Y. Echizen, K. Umeo, S. Kobayashi, M. Sera, P. S. Salamakha, O. L. Sologub, T. Takabatake, X. Chen, T. Tayama, T. Sakakibara, M. H. Jung, and M. B. Maple, Phys. Rev. B 68, 054416 (2003).

[66] Y. Tokiwa, J. J. Ishikawa, S. Nakatsuji and P. Gegenwart, Nature Materials 13, 356 (2014).

[67] V. Fritsch, N. Bagrets, G. Goll, W. Kittler, M. J. Wolf, K. Grube, C.-L. Huang, and H. v. Lhneysen, Phys. Rev. B 89, 054416 (2014).

[68] E. D. Mun, S. L. Bud'ko, C. Martin, H. Kim, M. A. Tanatar, J.-H. Park, T. Murphy, G. M. Schmiedeshoff, N. Dilley, R. Prozorov, and P. C. Canfield, Phys. Rev. B 87, 075120 (2013).

[69] C. Krellner, S. Lausberg, A. Steppke, M. Brando, L. Pedrero, H. Pfau, S. Tence, H. Rosner, F. Steglich and C. Geibel, New Journal of Physics 13, 103014 (2011).

[70] A. Rosch, A. Schroder, O. Stockert and H. v. Lohneysen, Phys. Rev. Lett. 79, 159 (1997).

[71] O. Stockert, H. v. Lhneysen, A. Rosch, N. Pyka, and M. Loewenhaupt, Phys. Rev. Lett. 80, 5627 (1998).

[72] S. Nakatsuji, D. Pines and Z. Fisk, Phys. Rev. Lett. 92, 016401 (2004).

[73] N. J. Curro, B.-L. Young, J. Schmalian and D. Pines, Phys. Rev. B 70, 235117 (2004).

[74] Y. Yang and D. Pines, Proc. Natl. Acad. Sci. USA 109, E3060 (2012).

[75] P. Coleman, Physica B 259, 353 (1999).

[76] G. E. Volovik, The Universe in an Helium Droplet, Oxford Science Publications, Oxford (2010).

[77] N. D. Mermin, Rev. Mod. Phys. 51, 591 (1979).

[78] H. Ikeda and K. Miyake, J. Phys. Soc. Jpn. 65, 6, 1769 (1996).

[79] J. Moreno and P. Coleman, Phys. Rev. Lett. 84, 342 (2000).

[80] P. S. Riseborough, Adv. Phys. 49, 257 (2000).

[81] M. Dzero, K. Sun, V. Galitski, and P. Coleman, Phys. Rev. Lett. 104, 106408 (2010).

[82] M. Z. Hasan and C. L. Kane, Rev. Mod. Phys. 82, 3045 (2010).

[83] K. Hanzawa, K. Yosida, K. Yamada, Prog. Theor. Phys. 81, 960 (1989).

[84] E. Abrahams and P. Wölfle, Phys. Rev. B 78, 104423 (2008).

[85] A. Ramires, P. Coleman, A. H. Nevidomskyy and A. M. Tsvelik, Phys. Rev. Lett. 109, 176404 (2012).

[86] M. Okawa, M. Matsunami, K. Ishizaka, R. Eguchi, M. Taguchi, A. Chainani, Y. Takata, M. Yabashi, K. Tamasaku, Y. Nishino, T. Ishikawa, K. Kuga, N. Horie, S. Nakatsuji, and S. Shin, Phys. Rev. Lett. 104, 247201 (2010).

[87] A. H. Nevidomskyy and P. Coleman, Phys. Rev. Lett. 102, 077202 (2009).

[88] L. M. Holanda, J. M. Vargas, W. Iwamoto, C. Rettori, S. Nakatsuji, K. Kuga, Z. Fisk, S. B. Oseroff and P. G. Pagliuso, Phys. Rev. Lett. 107, 026402 (2011).

[89] S. E. Barnes, J. Phys. F 6, 1375 (1976).

[90] A. Hackl and M. Vojta, Phys. Rev. Lett. 106, 137002 (2011).

[91] Y. Matsumoto, K. Kuga, T. Tomita, Y. Karaki, and S. Nakatsuji, Phys. Rev. B 84, 125126 (2011).

[92] E. C. T. O'Farrell, D. A. Tompsett, N. Horie, S. Nakatsuji and M. L. Sutherland, J. Phys.: Conf. Ser. 391 012053 (2012).

[93] S. E. Barnes, Adv. in Phys. 30, 801 (1980).

[94] J. Korringa, Physica 16, 601 (1950).

[95] C. Tien, J.-T. Yu and H.-M. Duh, Jap. J. Appl. Phys. 32, 2658 (1993).

[96] J. Sichelschmidt, V. A. Ivanshin, J. Ferstl, C. Geibel and F Steglich, Phys. Rev. Lett. 91, 156401 (2003).

[97] J. G. S. Duque, E. M. Bittar, C. Adriano, C. Giles, L. M. Holanda, R. Lora-Serrano, P. G. Pagliuso, C. Rettori, C. A. Pérez, Rongwei Hu, C. Petrovic, S. Maquilon, Z. Fisk, D. L. Huber and S. B. Oseroff, Phys. Rev. B 79, 035122 (2009).

[98] U. Schaufuβ, V. Kataev, A. A. Zvyagin, B. Buchner, J. Sichelschmidt, J. Wykhoff, C. Krellner, C. Geibel, F. Steglich, Phys. Rev. Lett. 102, 076405 (2009).

[99] J. Sichelschmidt, J. Wykhoff, H.-A. Kryg von Nidda, I. I. Fazlishanov, Z. Hossain, C. Krellner, C. Geibel and F. Steglich, J. Phys. Condens. Matter 19 016211 (2007).

[100] C. Krellner, T. Förster, H. Jeevan, C. Geibel and J. Sichelschmidt , Phys. Rev. Lett. 100, 066401 (2008).

[101] V. A. Ivanshin, A. A. Sukhanov, D. A. Sokolov, M. C. Aronson, S. Jia, S. L. Bud'ko and P. C. Canfield, J. Alloys and Comp. 480, 126 (2009).

[102] B. I. Kochelaev, S. I. Belov, A. M. Skvortsova, A. S. Kutuzov, J. Sichelschmidt, J. Wykhoff, C. Geibel, F. Steglich, Eur. Phys. J. B 72, 485 (2009).

[103] P. Schlottmann, Phys. Rev. B 79, 045104 (2009).

[104] D. A. Tompsett, Z. P.Yin, G. G. Lonzarich, W. E. Pickett, Phys. Rev. B 82, 235101 (2010).

[105] L. J. Tao, D. Davidov, R. Orbach and E. P. Chock, Phys. Rev. B 4, 5 (1971).

[106] R. T. Macaluso, S. Nakatsuji, K. Kuga, E. L. Thomas, Y. Machida, Y. Maeno, Z. Fisk and J. Y. Chan, Chem. Mater. 19, 1918 (2007).

[107] Z. Schlesinger, Z. Fisk, Hai-Tao Zhang, M. B. Maple, J. F. DiTusa and G. Aeppli, Phys. Rev. Lett. 71, 1748 (1993).

[108] E. C. T. O'Farrell, Y. Matsumoto, and S. Nakatsuji, Phys. Rev. Lett. 109, 176405 (2012).

[109] J. Sichelschmidt, V. A. Ivanshin, J. Ferstl, C. Geibel and F. Steglich, Phys. Rev. Lett. 91, 156401 (2003).

[110] P. G. Pagliuso, C. Rettori and L. M. Holanda (private communication).

[111] J. Schwinger, "On angular momentum", Report to the US Atomic Energy Commission NYO-3071 (1952).

[112] N. Read and S. Sachdev, Phys. Rev. Lett. 62, 1694 (1989).

[113] N. Read and S. Sachdev, Nucl. Phys. B 316, 609 (1989).

[114] S. Sarker, C. Jayaprakash, H. R. Krishnamurthy and M. Ma, Phys. Rev. B 40, 5028 (1989).

[115] A. A. Abrikosov, Physics 2, 5 (1965).

[116] T. Holstein and H. Primakoff, Phys. Rev. 58, 1098 (1940).

[117] A. Tsvelik, Phys. Rev. Lett. 69, 2142 (1992).

[118] R. P. Kenan, Jour. of Apply. Phys., 37, 1453 (1966).

[119] D. C. Mattis, Theory of Magnetism, page 77, Harper & Row (1965).

[120] A. Shnirman and Y. Makhlin, Phys. Rev. Lett. 91, 207204 (2003).

[121] R. Flint, PhD thesis, Rutgers University (2010).

[122] N. Read and S. Sachdev, Phys. Rev. Lett. 66, 1773 (1991).

[123] R. Flint, M. Dzero and P. Coleman, Nature Physics 4, 643 (2008).

[124] I. Affleck, Z. Zou, T. Hsu and P. W. Anderson, Phys. Rev. B 38, 745 (1988).

[125] P. Coleman, A. M. Tsvelik, N. Andrei and H. Y. Kee, J. Phys Cond Matt, 10, L239 (1998).

[126] J. Gan and P. Coleman, Physica B 171, 3 (1991).

[127] J. Gan, P. Coleman and N. Andrei, Phys. Rev. Lett 68, 3476 (1992).

[128] C. Pépin and M. Lavagna, Phys. Rev. B 59, 12180 (1999).

[129] P. Coleman, C. Pépin and A. M. Tsvelik, Phys. Rev. B 62, 3852 (2000).

[130] I. Bars, Physica D 15, 42 (1985).

[131] C. O. Nwachuku and M. A. Rashid, J. of Math. Phys. 18, 1387 (1977).

[132] S. Paschen, T. Lhmann, S. Wirth, P. Gegenwart, O. Trovarelli, C. Geibel, F. Steglich, P. Coleman and Q. Si, Nature 432, 881 (2004).

[133] P. Gegenwart, Science 315, 969 (2007).

[134] S. Friedmann, et al., Nature Physics 5, 465 (2009).

[135] A. Donni, G. Ehlers, H. Maletta, P. Fischer, H. Kitazawa and M. Zolliker, J. Phys.: Condens. Matter 8, 11213 (1996).

[136] M. Dolores Nunez-Regueriro, C. LaCroix and B. Canals, Physica C 282-287, 1885-1886 (1997).

[137] P. Coleman, C. Pèpin, Q. Si and R. Ramazashvili, J. Phys.: Condens. Matter 13, R723 (2001).

[138] A. Auerbach and D. P. Arovas, Phys. Rev. Lett 61, 617 (1988).

[139] D. Yoshioka, J. of the Phys. Soc. of Jpn. 58, 32 (1989), ibid 58, 3733 (1989).

[140] P. Coleman, Phys. Rev. B 28, 5255 (1983).

[141] N. Read, and D. M. Newns, J. Phys. C 29, L1055, (1983).

[142] A. Auerbach, and K. Levin, Phys. Rev. Lett. 57, 877 (1986).

[143] A. J. Millis and P. A. Lee, Phys. Rev. 35, 3394–3414 (1987),

[144] D. P. Arovas and A. Auerbach, Phys. Rev. B 38, 316 (1988).

[145] R. Flint and P. Coleman, Physical Review B 79, 014424 (2009).

[146] C. Jayaprakash, H. R. Krishnamurthy and S. Sarker, Phys. Rev. B 40, 2610 (1989).

[147] M. Hamermesh, Group Theory and its application to Physical Problems, Dover Publications (1962).

[148] R. C. King, J. Math. Phys. 12, 1588 (1971).